DOCTORAL THESIS

Developing a Remote Sensing System Based on X-Band Radar Technology for Coastal Morphodynamics Study

Wendy P. Navarro A.
2020

Doctorate Programme in Electrical and Electronics Engineering
Department of Electrical and Electronics Engineering

UN Universidad DEL NORTE

UNIVERSIDAD DEL NORTE

DOCTORAL THESIS

Developing a Remote Sensing System based on X-band Radar Technology for Coastal Morphodynamics Study

---

Author:
Wendy P. Navarro Ariza

Supervisors:
Dr. Juan Carlos Vélez D.
Dr. Alejandro Orfila F.

A thesis submitted in fulfillment of the requirements
for the degree of Doctor in Electrical and Electronics Engineering
in the

Department of Electrical and Electronics Engineering

UNIVERSIDAD DEL NORTE

February, 2020

Declaration of Authorship

I, Wendy P. Navarro Ariza, declare that this thesis titled, "Developing a Remote Sensing System based on X-band Radar Technology for Coastal Morphodynamics Study" and the work presented in this manuscript are my own. I confirm that:

- This work was done wholly or mainly while in candidature for a research degree at this University.

- Where any part of this thesis has previously been submitted for a degree or any other qualification at this University or any other institution, this has been clearly stated.

- Where I have consulted the published work of others, this is always clearly attributed.

- Where I have quoted from the work of others, the source is always given. With the exception of such quotations, this thesis is entirely my own work.

- I have acknowledged all main sources of help.

- Where the thesis is based on work done by myself jointly with others, I have made clear exactly what was done by others and what I have contributed myself.

Signed:

Date: 6th February 2020

Thesis Specifications

Student ID	200030051
Author Name	Wendy Paola Navarro Ariza, Eng. MSc.
E-mail	wendnavarro@gmail.com; wendyn@uninorte.edu.co
Doctoral Thesis Title	Developing a Remote Sensing System based on X-band Radar Technology for Coastal Morphodynamics Study.
Thesis Advisor	**Dr. Juan Carlos Vélez Díaz** Titular Professor, Universidad del Norte Chief of the Postgraduate Program in Electrical and Electronics Engineering Chief of the Telecommunication and Signals Research Group (GT&S)
Thesis Co-Advisor	**Dr. Alejandro Orfila Förster** Tenured Scientist CSIC Dept. of Oceanography and Global Change Marine Technologies and Operational Oceanography: TMOOS Group Leader IMEDEA. Esporles - Spain
Research Group	Telecommunication and Signals Research Group
Research Area	Telecommunication Systems
Research Line	Digital Image and Signal Processing High Frequency Electronics Circuits
Research Sub-line	Remote Sensing
VoBo. Thesis Advisor	
VoBo. Thesis Co-Advisor	

"Whatever you do, you need courage. Whatever course you decide upon, there is always some one to tell you that you are wrong. There are always difficulties arising to tempt you to believe your critics are right. To map out a course of action and follow it to an end requires some of the same courage that a soldier needs. Peace has it's victories, but it takes brave men and women to win them."

Ralph Waldo Emerson (1803–1882)

"Success is not the key to happiness. Happiness is the key to success. If you love what you are doing, you will be successful."

Albert Schweitzer (1919-1965)

Abstract

This PhD thesis is a step further in the understanding of novel applications for X-Band radars to study morphodynamics and wave hydrodynamics in coastal areas. . New data processing techniques are proposed for the assessment of scopes and limitations from radar-derived sea state parameters, coastline evolution and water depth estimates. Most of the raised research is focused on Colombian Caribbean coast and the Western Mediterranean Sea.

First, a novel procedure to mitigate shadowing in radar images is proposed. The method compensates distortions introduced by the radar acquisition process and the power decay of the radar signal along range applying image enhancement techniques through a couple of pre-processing steps based on filtering and interpolation. Results reveal that the proposed methodology reproduces with high accuracy the sea state parameters in nearshore areas. The best performance is achieved when the significant wave height (H_s) is at least 0.5 m and preferably higher and the peak period is $T_p \geq 4$ s.

The improvement resulting from the proposed method is assessed in a coral reef barrier, introducing a completely novel use for X-Band radar in coastal environments. So far, wave energy dissipation on a coral reef barrier has been studied by a few in-situ sensors placed in a straight line, perpendicular to the coastline, but never been described using marine radars. In this context, this dissertation use marine radar images to describe prominent features of coral reefs, including the delineation of reef morphological structure, wave energy dissipation and wave transformation processes in the lagoon of San Andres Island barrier-reef system.

Results show that reef attenuates incident waves by approximately 75% due to both frictional and wave breaking dissipation, with an equivalent bottom roughness of 0.20 m and a wave friction factor of 0.18. These parameters are comparable with estimates reported in other shallow coral reef lagoons as well as at meadow canopies, obtained using in-situ measurements of wave parameters. Besides, the mean height of the reef elements is also estimated in the entire radar coverage area. Results are both in the same order of magnitude of measured data reported by previous studies and in good agreement with the geometric parameters proposed by in-canopy flow models for branched species, such as *Stylophora* and *Pocillopora*, which are also common in the coral carpets of San Andres Island.

Finally, the assessment of morphological mapping facilities of X-Band radars is performed by comparing radar-derived bathymetry and shoreline estimates with in-situ data and the previously reported video performance at the study sites. Results reveal a promising combined use of X-Band radars and stereo-video systems as complementing monitoring tools in coastal areas. Therefore, radars and optical video systems should be considered as complementing morphological mapping tools, instead of excluding, in order to provide higher-resolution and more accurate bathymetric estimates and shoreline measurements in a broad area.

Agradecimientos

Una bitácora me acompaña siempre a cada viaje. Un pequeño cuaderno donde intento inmortalizar a través de la escritura las experiencias más significativas, aquellas que nunca deseo olvidar. Este viaje llamado *tesis doctoral* no ha sido la excepción. Y hoy, cuando ha llegado a feliz término, me he tomado el trabajo de revisar las páginas escritas en estos últimos 54 meses de arduo trabajo. Noto que no hay mejor frase para resumir lo que ha supuesto para mí desarrollar esta investigación que aquel famoso proverbio chino: "*Si caminas solo, irás más rápido; si caminas acompañado, llegarás más lejos*". Por lo cual, el mérito del aporte alcanzado en esta tesis debe ser atribuído a la labor conjunta de diferentes personas e instituciones que contribuyeron de múltiples formas durante su desarrollo y de quienes hago mención en las siguientes líneas.

Quiero agradecer en primer lugar al autor de mis días, mi Padre Celestial, por abrir las puertas necesarias y rodearme de las personas indicadas en los tiempos correctos. Por ser mi principal fuente de paz y conocimiento. Este documento y todo lo aprendido ha sido obra de Su Gracia.

Agradezco profundamente a mis directores, Juan Carlos y Alejandro, porque han dado siempre lo mejor de sí mismos para alcanzar este anhelado sueño. Su contibución multidisciplinaria ha sido la clave para orientar esta tesis hacia los resultados obtenidos. Por ello, mi mayor agradecimiento está dirigido a ellos.

Gracias Juan Carlos, por ver en mí un gran potencial y acompañarme desde mi formación profesional como ingeniera hasta este punto de mi vida. Por haberme propuesto cinco años atrás iniciar el doctorado en esta temática y por orientar este trabajo con tu experiencia en radioelectrónica. Muchas gracias por tus comentarios, tu actitud reflexiva y tu marcado liderazgo. Por preocuparte por mi desarrollo integral y por permitirme recurrir a tu experiencia científica en un marco de confianza, afecto y amistad. Por las charlas en tu oficina que comenzaban con la tesis y terminaban con un café, consejos para la vida y divertidas anécdotas. Por tu espiritualidad, por ser más que un tutor, un verdadero amigo. Sé que siempre podré contar con tu valioso apoyo. A tí debo haber conocido a Alejandro y a muchas de las personas e instituciones que abrieron paso a este proyecto.

Jano, gracias por animarme a tomar este camino en la investigación, por tu valiosa amistad y tu enorme paciencia. Pasar de llamarte *Dr. Orfila* a *Jano* no fue duro trabajo para mí ya que siempre te has mostrado cercano, atento y dispuesto a colaborar en este camino. Las charlas en tu oficina, los libros y artículos que me sugeriste leer, tu siempre oportuna orientación, soporte y discusión crítica, fueron abriendo paso a esta investigación y me permitieron aprender mucho más de lo reportado en este documento. Tu ejemplo y tu actitud han sido la mejor escuela de formación en todo este tiempo y han inspirado en mí el carácter de un buen científico. Gracias por mantener siempre abiertas las puertas de tu oficina para acudir ante cualquier duda y por la confianza que has depositado en mí. Por estar dispuesto aún a cargar junto conmigo las antenas y dispositivos en cada salida de campo. Muchas gracias por brindarme la oportunidad de realizar mi pasantía

en IMEDEA, la más significativa de las experiencias vividas durante este tiempo. Gracias por convencer a tantas personas e instituciones para que apoyaran este proyecto. A tí debo mucho de lo aprendido y vivido. Muchas gracias, amigo.

Quiero extender un sincero agradecimiento al Dr. Gonzalo Simarro del Instituto de Ciencias del Mar ICM-CSIC en Barcelona, por haberme compartido más de lo que pensé aprender acerca de su trabajo durante mi estancia en dicha institución. Muchas gracias por su asesoría y colaboración al proporcionar acceso al algoritmo *uBathy* de su autoría, el cual permitió la estimación remota de la batimetría usando radares de microondas. Gracias también al Dr. Daniel Calvete y a la Dra. Francesca Ribas por su apoyo en este tema.

Me gustaría también agradecer de manera especial al Dr. Serguei Lonin y a la Escuela Naval de Cadetes Almirante Padilla (ENAP) en Cartagena de Indias por el soporte técnico y financiero para el traslado del radar a la isla de San Andrés y las mediciones in-situ realizadas. También agradezco al personal técnico del SOCIB, en especial a Benja, Pau, Nico e Irene, por su apoyo incondicional en la toma de datos con instrumentación in-situ y por colaborar con el montaje del radar en cada campaña de medición realizada en España. Son un excelente equipo de trabajo. Gracias Dr. Jorge Guillen y Dr. Lluis Gómez-Pujol por su interés en los resultados de esta investigación.

Especial mención merecen las personas cuya colaboración ha sido importante en el desarrollo de este trabajo. A Antonio Serrano, Iván Arias y Jonathan Posada por marcar un camino inicial en esta investigación y por el soporte técnico en el diseño electrónico de las tarjetas de adquisición. A Andrés Orejarena por su valiosa colaboración aportando modelos numéricos para la validación de las mediciones del radar en la isla de San Andrés. Gracias Amaya por enseñarme, desde tu experiencia, el tratamiento de datos in-situ de RTKs, ADVs y AWACs que me permitió obtener gran parte de los resultados de validación. Por darme la oportunidad de acompañarte durante la toma de datos y entender el procedimiento de medición.

Muchas gracias al Departamento de Ingeniería Eléctrica y Electrónica y a la Dirección de Investigación, Desarrollo e Innovación de la Universidad del Norte por su apoyo técnico y financiero. En especial, al Dr. Raimundo Abello y a Katherine Pardo por su incondicional apoyo para la exportación temporal del radar y la instalación de instrumentos in-situ en las diferentes salidas de campo realizadas en Colombia. Su gestión y arduo trabajo fueron determinantes para la consecución de este logro. A Reynaldo por su incondicional colaboración desde el laboratorio de Ingeniería Eléctrica y Electrónica. A Luisa Baldovino y Jessie Gamarra por su gestión administrativa para la solicitud de los diferentes desembolsos ante COLCIENCIAS. Mis más sinceros agradecimientos a los profesores del Programa de Doctorado en Ingeniería Eléctrica y Electrónica, en especial a la Dra. María Gabriela Calle, por su amistad, colaboración e interés en esta investigacón.

Gracias a mis compañeros de doctorado en Uninorte, Jorge, Jamer, Sandra y Liesle por su amistad y complicidad. Por haber hecho de esta etapa un trayecto de vivencias inolvidables.

I would like to express my sincere gratitude to all of my colleagues at IMEDEA, in particular to Merit, Carlos, Juanma, Isma, Ester, Vero, Bárbara, Ana Lucía, Laura, Andrea, Juan David, Dani, Tim, Chloe and Eva. I enjoyed working in this friendly and international atmosphere where

everybody is dedicated to research and science. I owe you my gratitude for sharing laughs, cups of coffee and giving me your sincere friendship that remains despite the distance. I hope you can replicate again my millenary recipe for cooking *egg arepas*.

Christopher and Francisca Ellwood, you gave me a lot of reason to thank you. Your kindness and generosity have touched my heart during my stay at your house in Esporles. It was a pleasure to be accompanied by your loving family. I am grateful for your hospitality, I felt at home the entire time. All my love and thanks to you.

Y, por supuesto, el agradecimiento más sentido y profundo es para mi familia. Por su apoyo incondicional y comprensión. A mis padres, Aida y José, por enseñarme con su ejemplo de vida el valor del trabajo, el amor y el sacrificio. A mi hermano José David por ser ejemplo de valentía y superación. A mis abuelas Aija y Aura por enseñarme a disfrutar cada detalle de la vida. Mi historia y mi legado estarían incompletos sin mencionarlos a ellos. De manera muy especial agradezco a mi esposo David Marum, quien ha permanecido incondicionalmente a mi lado, incluso durante las noches de trabajo, animándome a luchar incansablemente por este sueño. Él, siendo la mayor motivación en mi vida encaminada al éxito, fue el complemento perfecto para poder alcanzar esta victoria. Gracias cariño por ser el mejor compañero de viaje y la fuerza detrás de este logro. Por comprenderme y preocuparte por mí en cada momento. Por tu paciencia, entrega y sacrificio. Por demostrarme que estás dispuesto a deshacerte para que yo me haga. Por creer siempre en mí y por demostrarme que puedo llamar *casa* a cualquier lugar donde estemos los dos. Eres mi mayor inspiración y motivación. A tí dedico esta tesis.

Contents

List of Figures

List of Tables

List of Abbreviations

Abbreviation/Acronym	Expression
ADC	Analog-to-Digital Converter
ADCP	Acoustic Doppler Current Profiler
ADV	Acoustic Doppler Velocimeter
ANN	Artificial Neural Network
ANOVA	Analysis Of Variance
ARPM	Adaptive Recursive Positioning Method
AUV	Autonomous Underwater Vehicle
AWAC	Acoustic Wave and Current
BASIR	Bar and Swash Imaging Radar
BP	Band-Pass
CC	Correlation Coefficients
CCF	Cross-Correlation Function
CSM	Cross Spectral Matrices
CWT	Continuous Wavelet Transform
DFT	Discrete Fourier Transform
DIMAR	Colombian National Marine Authority
DiSC	Dispersive Surface Classificator
dof	Degrees Of Freedom
EM	Electromagnetic Signal
EOF	Empirical Orthogonal Function
FFT	Fast-Fourier Transform
3D-FFT	Three dimensional Fast-Fourier Transform
GPS	Global Positioning System
HF	High Frequency
HH	Horizontal-Transmit-Horizontal-Receive
HP	High-Pass
HT	Hilbert Transform
IFFT	Inverse Fast-Fourier Transform
JONSWAP	JOint North Sea WAve Project
JPDF	Joint Probability Density Function
LAT	Geographical Latitude Coordinates
LiDAR	Laser Imaging Detection and Ranging
LON	Geographical Longitude Coordinates
LP	Low-Pass
LSD	Fisher's Least Significant Difference between means Test
MS	Mean Square
MSL	Mean Sea surface Level
MTF	Modulation Transfer Function
NRCS	Normalized Radar Cross Section
PC	Principal Component
PCA	Principal Component Analysis
PDF	Probability Distribution Function
PIV	Particle Imaging Velocimetry

Abbreviation/Acronym	Expression
PSD	Power Spectral Density
RCS	Radar Cross-Section
RMSE	Root Mean Square Error
SAR	Synthetic Aperture Radar
SNR	Signal-to-Noise Ratio
SoV	Source of Variance
SS	Square Sum
SVR	Support Vector Regression
SWAN	Simulating WAves Nearshore model
UTC	Universal Time Coordinated
VV	Vertical-Transmit-Vertical-Receive
WaMoS II	Wave and Current Monitoring System

List of Symbols

Symbol	Definition
a	Wave amplitude (m)
β	Critical breaking parameter
c	Wave celerity (ms^{-1})
C_g	Group velocity (ms^{-1})
E	Wave energy (Jm^{-2})
ϵ_{total}	Total wave energy dissipation rate per unit area (Jm^{-2}s^{-1})
ϵ_b	Wave energy dissipation rate (per unit area) due to wave breaking (Jm^{-2}s^{-1})
ϵ_f	Wave energy dissipation rate (per unit area) due to bottom friction (Jm^{-2}s^{-1})
F	Wave energy flux
f	Wave frequency (Hz)
f_p	Peak wave frequency (Hz)
f_{ADC}	Sample frequency for the Analog-to-Digital Converter (Hz)
$f_{e,r}$	Representative dissipation factor
$f_{w,r}$	Representative friction factor
g	Acceleration of gravity (ms^{-2})
γ	Peak shape parameter from JONSWAP formulation
h	Water depth (m)
h_{ant}	Radar antenna height (m)
H_{bed}	Height of the bottom roughness elements (m)
H_{rms}	Root-mean squared (RMS) wave height (m)
H_s	Significant wave height (m)
H_{s_0}	Incident significant wave height at offshore distance (m)
κ	Kurtosis
$\vec{k}, \mathrm{k}$	Wavenumber vector (m^{-1})
K_p	Pressure response factor
k_p	Peak wave number (m^{-1})
k_w	Equivalent bottom roughness (m)
λ_p	Peak wavelength (m)
λ_0	Wavelength at deep waters (m)
ϕ_r	Representative phase lag (degrees)
$\Delta\varphi$	Horizontal beam resolution (degrees)
Φ	Grazing incidence angle (degrees)
p_D	Dynamic pressure (dbar)
ρ	Seawater density (kg/m^3)
Δr	Spatial resolution (m)
Δr_{RADAR}	Nominal radar range resolution (m)
r	Correlation coefficient
r_0	Specific distance from radar antenna (m)
σ	Standard deviation
$S(f)$	Wave energy spectral density (m^{2}s)

Symbol	Definition
τ_w	Bottom shear stress ($\mathrm{Nm^{-2}}$)
θ	Wave direction (degrees)
θ_p	Peak wave direction (degrees)
T	Wave period (s)
T_p	Peak wave period (s)
Δt	Temporal resolution (s)
u	Fluid velocity ($\mathrm{ms^{-1}}$)
u_b	Near-bottom horizontal orbital velocity ($\mathrm{ms^{-1}}$)
ω	Wave angular frequency ($\mathrm{s^{-1}}$)
ω_p	Peak wave angular frequency ($\mathrm{s^{-1}}$)
ω_r	Representative wave angular frequency ($\mathrm{s^{-1}}$)

This dissertation is dedicated to the almighty God, my Creator, my Master and my Friend.

This is for you, Mom and Dad. Thanks for always being there and for teaching me the value of hard work, love and sacrifice. My story and legacy is incomplete without mentioning you, Aida and José.

For my dearest husband, who encouraged me to pursue my dreams and be brave. He has been the driving force behind my success. Thanks for joining me up to here, even at sleepless nights. Thank you for being a shelter and my favourite place.

In memory of my beloved grandparents, Erdulfo and J. Santander, and my lovely aunt Nohora, who left traces of grace on my life. Although they were my inspiration to pursue my doctoral degree, they were unable to see my graduation. This is for them and for all people who have touched my soul.

Chapter 1

Introduction

"You cannot measure time by days, the way you measure money by dollars and cents, because dollars are all the same while every day is different and maybe every hour as well."

Jorge Luis Borges (1899 – 1986)

1.1 Background

Shallow water environments are dynamic areas that play an important role for commercial activities providing high value ecosystems and economic benefits, which make them one of the most attractive and populated land zones in the world [1]. In these areas, ocean waves interact with the bottom modifying their properties and conditioning its complex coastal morphology. In particular, beaches and non-consolidated coasts dissipate energy from incoming waves, being the first natural coastal defenses against flooding. Furthermore, extreme morphological changes in coastal areas can cause negative impacts on the quality-life of human settlements affecting also civil structures. Therefore, access to continuous and real-time wave measurements is crucial for coastal studies and the assessment of global change impacts on coasts [2].

Since sea state data provide significant information to design coastal management programmes, it might be expected that gathering data from accurate devices (i.e. in-situ sensors) would decrease reliability issues. Although traditional in-situ measurements provide accurate sea state data, their limited spatial resolution hinders to examine coastal processes in a broad area. Besides, acquisition of sea surface data and bathymetry surveying are complex, expensive and labor-intensive tasks [3]. For instance, in-situ sensors (e.g. buoys and bottom-mounted pressure gauges) could be affected by breaking waves and strong wave-driven currents in the surf zone during storm events. Although these are the most important periods of sediment transport, measurements conditions hamper data acquisition to describe them. The high cost of installation and maintenance of in-situ sensors is the main drawback to use them massively in shallow water areas [1].

In order to overcome the shortcomings of in-situ devices, several remote sensing approaches have been designed as cost-effective tools. Foremost among the available remote sensing technologies are satellite imagery, infrared cameras, *Laser imaging Detection and Ranging* systems (LiDAR), video-based monitoring techniques and radar technologies that operate in a broad

frequency band. Radar frequencies range from high frequency (HF), which allows the scanning of gravitational ocean waves, also known as long waves, to microwave and radio-wave of the electromagnetic (EM) spectrum, including S-Band and X-Band marine radar systems.

Fixed optical video cameras and X-Band marine radars (also named *passive* and *active* remote sensing technologies, respectively) are relatively young nearshore remote sensing approaches. However, they are able to scan sea surface with high spatial and temporal resolution spending less time and effort than in-situ measurements. They use intensity of the acquired signals (i.e. pixels for optical cameras and echo signals for X-Band radars) as a direct proxy of water level, neglecting non-linear behaviours in the nearshore area [4]. These systems are the main focus of the discussion in the present dissertation.

X-Band marine radars are typically used for nautical purposes, but they can also be employed as mapping devices of the surrounding wave dynamic through *sea clutter* signals processing. The indirect relationship between the radar remotely sensed data and the true value of the wave properties (i.e. significant wave height H_s, peak period T_p, or wavelength λ) can be explained by backscattering and Bragg scattering laws and the composite surface theory that establish microwave backscatter and sea surface elevation data relationship [5], [6]. For video-based coastal monitoring systems, the mathematical description of optical reflectivity from ocean waves is based on Maxwell's equations [7]. Besides, the acquired features resolution degrades in the spatial domain as pixels are further from the shoreline. This occurs because the illuminated facets corresponds to unique look directions but not unique distance span. This concern is less evident in radar sensors, which map sea clutter through echo signals that are geographically located at the field site. This is done using the time difference between the transmitted and the received electromagnetic signal, as well as the azimuth resolution derived from the geometry of the antenna look-direction.

Although X-Band radars are highly desirable sensors for coastal studies, their mapping issues are still widely held, mainly in shadowing conditions. X-Band radar data have shown poor performance in the surf and swash zones compared to their good estimations achieved at offshore. It could be explained by noisy echo signals reflected from sand and nearby buildings, as well as non-linear wave propagation in extremely dynamic nearshore areas. The latter has not been considered in detail by commercial radar-data acquisition devices, such as WaMoS II [8]. In the case of fixed video cameras, noisy signals can correspond to brightness signature acquired from foam arisen by wave breaking in the surf zone [4], [9] as well as the presence of hostile weather conditions (e.g. fog, low wind or rain) during measurements that also contributes to degrade their performance. It is worth to note that unlike radar systems, fixed optical video cameras are unable to scan sea state during night and it is nearly impossible to estimate H_s due to optical limitations.

The lack of accurate sea state data collection throughout the nearshore area is mainly due to inherent limitations of the remote sensing devices. It could be overcome developing novel techniques and improving data processing, which is one of the main purpose of this thesis.

1.2   Research objectives and scope

The aim of this research is to develop a novel method using X-Band radar remotely sensed data to estimate nearshore bathymetry and hydrodynamics, which are inspired by video imagery algorithms, as well as signal and image processing techniques. The study proposes to close the gaps in shaded radar data acquisition in shallow water areas for further investigation into merging video and radar retrieved data in coastal environments. Hence, this research exhibits the scopes and limitations from radar remote sensing systems at different coastal environments (e.g. sand-beaches, coral reefs and semi-stretched beaches) in order to examine the opportunity to merge the advantages of radars and video cameras, which could improve the reliability of retrieved coastal data.

This study also aims to include shadowing mitigation procedure in radar-data processing method. Thus, more accurate sea state data are obtained and the reliability of inferred bathymetry is improved by minimizing estimation errors from wave properties (e.g. significant wave height, wave celerity, wave period, wavelength and incident wave angle). The improvement resulting from the proposed method is assessed in a coral reef barrier, introducing a completely novel use for X-Band radar in coastal environments. So far, wave energy dissipation in a shallow coral reef lagoon has been studied by a few in-situ sensors placed in a straight line, perpendicular to the coastline. It had never been described by marine radar systems, which provide sea state data throughout nearshore areas with high spatial and temporal resolutions. Besides, shoreline detection and bathymetric inversion algorithms from X-Band radar image sequences are proposed. These applications of radar systems are focused on the evaluation of new opportunities to merge radar-derived estimates with video imagery methods. Thus, the following issues are investigated in this study:

- Development of a signal processing methodology that does not require empirical or semi-empirical calibration to minimize shadowing effects due to extreme grazing incidence angles throughout the intensities of the radar image.

- Estimation of wave properties such as significant wave height, peak period, peak wave-length and peak wave angle from retrieved radar data by using space-time and frequency information of the processed shaded intensities.

- Analysis of wave energy dissipation in a coral reef barrier using radar remotely sensing data, as a novel application of X-Band marine radars.

- Estimation of bottom roughness and friction factors in a lagoon area of the coral reef field site through spectral methodology considering physical formulations.

- Inversion of water depths in nearshore areas through estimated sea state parameters from radar-derived image sequences.

- Shoreline detection algorithm from processed sea clutter radar image sequences.

- Comparison of shoreline and bathymetric estimates derived from video imagery and radar through the investigation of the effects of error sources on both coastal remote sensing systems and considering different scenarios.

As a local motivation, coastal erosion is one of the most relevant environmental problems in Colombia, which is caused by extreme waves that change significantly seabed form and shoreline [10]. So far, thirty percent of 3000 kilometres of Colombian coast have been affected, causing negative social and ecological impacts specially in the Caribbean coast. Therefore, DIMAR (*National Maritime Authority*) has installed a network of eight directional wave buoys, four of them located in the Caribbean Sea [11]. Despite these strategies to monitor wave climate, the present buoys are not sufficient to monitor entire coastal dynamic.

In this context, the massive installation of low-cost coastal monitoring systems in Colombian coasts is crucial to provide real-time data that describe the particularly complex coastal processes. This can be achieved installing radar systems throughout the littoral at nearshore towers or high buildings where antennas could be placed. However, shadowing effects have to be mitigated since, in most cases, the height of buildings does not exceed 50 meters above mean sea level (MSL) and hence grazing incidence angles are extreme.

1.3   Thesis Overview

This doctoral dissertation offers new developments and data processing descriptions to improve the understanding of the coastal hydrodynamics and morphodynamics using X-Band radar systems. Most of the raised research is focused on Colombian Caribbean coast and the Western Mediterranean Sea. In this context, this dissertation combines signal and image processing techniques as well as spectral analysis methodologies with the use of observations- radar, video imagery and in-situ sensors (e.g. AWAC, ADV and ADCP devices)- and numerical modelling data from *Simulating WAves Nearshore* (SWAN) model.

In Chapter 2, previous studies on coastal remote sensing using X-Band radars and fixed optical video cameras are reviewed considering their methodologies, advantages and shortcomings. Besides, the necessary wave and radar theory is introduced, including a short description of some commercial wave-data acquisition systems from radar and video imagery. Chapter 3 summarizes methods and data sources used along this dissertation. It provides details of the X-Band marine radar system, the video camera monitoring system and all field sites, where sea clutter acquisition and data analysis process were performed.

The development of a novel procedure based on filtering and interpolation approaches is fully detailed in Chapter 4. Methods and techniques developed are of general applicability to estimate sea state parameters including significant wave height, peak wave direction, peak period, peak wavenumber and peak wavelength in shallow waters using X-Band marine radars.

Wave energy dissipation in a coral reef coastal environment is analysed in Chapter 5. This work is performed through two physical formulation [12]–[15] in the frequency domain by using a set of processed wave-radar composites, which were measured in San Andres Island. A spatial distribution of bottom roughness and friction factor is obtained in the study area considering only sea clutter images. A SWAN model provides sea state information of the surrounding zone to validate X-Band radar estimates. Simulation is forced by the water depth measurements, which were acquired during the field campaign.

Most of the time, wave properties estimates are used as inputs for obtaining others physical variables as bathymetry using three-dimensional Fast Fourier Transform (FFT), power spectral density (PSD) and time-frequency processing techniques. Chapter 6 gives an extended explanation of the proposed approach to estimate water depth (*uBathy* algorithm [16]) which is based on *empirical orthogonal functions* (EOF) and Hilbert Transform, as a novel bathymetric inversion algorithm from video imagery, which is adapted to radar data. Besides, a brief description of the shoreline detection algorithm derived from X-Band radar sea clutter data is stated, including a sensitivity analysis and a contrast against video imagery results.

Finally, Chapter 7 presents the overall conclusions of this doctoral dissertation and some future research considerations to expand the here addressed lines of research.

Chapter 2

Literature Review

"Life is a series of steps. Things are done gradually. Once in a while there is a giant step, but most of the time we are taking small, seemingly insignificant steps on the stairway of life."

Ralph Ransom (1903 – 1959)

2.1   Introduction

A large number of coastal dynamics studies within the last three decades reveals a growing interest in nearshore processes among the scientific community. However, poor availability of real-time sea state data restricts the reliability of coastal assessments [17]. The higher data efficiency, the more accurate predictions are obtained, regardless of inherent limitations of the monitoring devices [18]. Thereby, the forecasting and hindcasting of coastal hazards could be improved. The ideal scenario combines accurate real-time sea state data and morphological estimates from a distributed network of in-situ and remote sensors, yielding further data and useful foresights of coastal dynamics. This Chapter is focused on the study of video-based and X-Band marine radar systems as coastal mapping devices. It begins with the applicable linear wave theory and its non-linear limitations in shallow water. Then, a brief description of coastal observations is introduced, including in-situ and remote sensing platforms. Afterwards, nearshore applications of commercial microwave and optical monitoring systems are fully detailed. An overview of depth inversion and shoreline detection algorithms using video and radar remote sensing systems is also included. This Chapter concludes by examining previous studies that combines data from both remote sensors, highlighting a potential new line of research.

2.2   Nearshore Hydrodynamics and Morphodynamics

Coastal dynamics responds to ocean wave energy processes that drive nearshore currents circulation and sediment transport. The interaction between waves, currents and the seabed form describes the shape of the sea surface and beach morphology. In order to simplify the analysis of field data, ideal hydrodynamic conditions are usually considered. However, most remote sensing techniques does not take into account non-linear effects associated with shoaling, wave

breaking, refraction and diffraction. Therefore, estimation errors resulting from this simplification are relevant in the surf zone, where the effects of non-linear wave amplitude dispersion contributes significantly to nearshore processes [4]. Remote sensing techniques propose indirect measurements that require the application of physical concepts to infer the local bottom morphodynamics from the nearshore wave properties. This section describes the necessary linear wave dispersion relation and the non-linear limitations in the shallow water applicable to this doctoral dissertation.

2.2.1   Linear Wave Theory

The surface wave dispersion and its interaction with the complex bottom morphology is analyzed by means of the linear wave theory [9], [19], [20]. The linear wave theory is based on the continuity equation and the momentum balance whose solution requires the consideration of *dynamic* and *kinematic* free surface boundary conditions to establish the physical system behaviour. The dynamic boundary conditions use the Bernoulli equation to specify a constant pressure of the water surface. The kinematic air-water interface boundary conditions prescribe that any fluid particles must flow across the interface. In other words, the particles must not leave the surface [19].

The solution of the linear wave theory equations leads to the definition of the sea surface elevation as freely propagating harmonic waves in the form,

$$\eta = a \sin\left(\omega t - kx\right) \tag{2.1}$$

where η is the surface elevation that relies on time t and space x, a describes the amplitude of the waves, $\omega = 2\pi/T$ is the wave frequency and the wavenumber k is defined as $2\pi/\lambda$ for waves with a period of T and a wavelength λ [9], [19]. Besides, kinematic free surface boundary conditions describe the manner in which waves that propagate at different frequencies could separate or *disperse* due to the celerities of the different wave frequency components [19], [21]. Neglecting surface current, the relationship between ω and k can be explained by the *linear dispersion relation* defined as,

$$\omega^2 = gk \tanh(kh) \tag{2.2}$$

where g is the acceleration of gravity and h represents the local water depth. Since wave celerity c is given by λ/T, which in turn is equivalent to ω/k, the linear dispersion relation can be expressed as,

$$c = \sqrt{\frac{g}{k} \tanh\left(kh\right)} = \sqrt{\frac{gT}{2\pi} \tanh\left(kh\right)} \tag{2.3}$$

As water depth becomes large (i.e. deep water, $h/\lambda > 0.5$), the relation $\tanh\left(kh\right) \approx 1$ is satisfied. Hence, $c = \sqrt{g/k}$ depends on the wavenumber and implicitly on wave period. Besides, the wavelength can be defined as,

$$\lambda = cT = \lambda_0 \tanh(kh) \tag{2.4}$$

where λ_0 is the wavelength at deep waters $gT^2/2\pi$. In the case of shallow water, i.e. $h/\lambda \leq 0.05$, the relation $\tanh(kh) \approx kh$ is satisfied. Therefore, $c = \sqrt{gh}$ that is solely a function of local water depth. This leads to yield h estimates from gathered hydrodynamic wave parameters that are given by,

$$h_{linear} = \frac{1}{k} \tanh^{-1} \left(\frac{\omega^2}{gk} \right) = \frac{2\pi}{\lambda} \tanh^{-1} \left(\frac{\lambda}{\lambda_0} \right) \tag{2.5}$$

The linear wave dispersion relation and its non-linearity variants are the main physical concepts behind the depth inversion methodology explained in Chapter 6.

2.2.2 Non-linear Limitations

The linear wave theory assumes an incompressible fluid with a constant density without stratification and a continuous water body, which is subjected to a single external force. Besides, it assumes that wave height is small compared with the local water depth. Hence, this small-amplitude approximation is not applicable in non-dispersive shallow water waves which do not depend on wavelength or frequency.

Several studies have proposed non-linear approximations of the linear dispersion relation to inverse finite water depth with higher accuracy. They have demonstrated that the linear dispersion relation underestimates the wave speed and overestimates the water depth within the surf zone. The solitary wave theory approximates wave celerity in shallow water as a function of water depth and wave height (H) defined as,

$$c = \sqrt{g(h + H)} \tag{2.6}$$

which considers infinitely long wavelength [21], [22], but this is an idealization for waves bounded by the littoral in shallow waters. In the absence of currents, relative errors tend to be of order 10% in intermediate water depths. However, errors increases as waves shoal and water depths are often over-predicted with errors of more than 25% [23], [24]. In shallow water, errors and wave height have shown to be correlated [21], [24].

Thornton and Guza [25] found that the ratio H_{rms}/h is 0.42 considering their field measurements in the inner surf zone. H_{rms} corresponds to the root mean squared (RMS) wave height. It implies that water depth is overestimated up to 42% using the linear dispersion relation in the nearshore area. Grilli [26] found errors up to 50-70% for water depth estimates based on solitary linear wave theory.

Hedges [27] suggested a correction for finite amplitude dispersion as follows,

$$h_{Hedges} = \frac{2\pi}{\lambda} \tanh^{-1} \left(\frac{\lambda}{\lambda_0} \right) + Z \tag{2.7}$$

proposing $Z = H$ as an empirical parameter that includes non-linear behaviour of large waves in nearshore areas which propagate faster than the predictions of the linear wave theory. Booij [28] suggested $Z = 0.5H$ for monochromatic waves or $Z = H_s/2\sqrt{2} = 0.35H_s$ for spectral waves. Holland [24] suggested an empirical shallow water phase speed relationship given by

$$c = \sqrt{g(h + \alpha H_s)} \tag{2.8}$$

where $\alpha = 0.48$ is an empirical coefficient that considers the best fit between measured wave celerity and water depth in regions shallower than 4 m. However, the normalized depth error is over 50%. Hence, a more accurate estimator of c and h is needed in shallow water areas.

2.3 Coastal Observations

Ocean waves are complex random processes whose amplitude and energy rely on wind speed, duration, intensity and the average distance of wind along ocean surface, also known as *fetch*. Appendix B explains in more detail the stochastic concept as applied to random ocean waves description. A never-ending cycle of additive combination of waves that come from different offshore directions gradually increases wave energy, which is slowly dissipated in deep waters. Thus, beach morphology responds to strong energy dissipation processes as waves shoal towards nearshore areas [20].

The most energetic coastal processes, such as sediment transport and creation of sand bars, take place throughout shoaling, breaking, surf and swash zones. Since ocean waves shoal and continuously interact with the local seabed, beach morphology suffers extreme changes, such as shoreline erosion, which can occur on varied time scales as hours to days and over a large span of spatial scales ranging from tens to kilometres [21]. For instance, a large storm can cause significant coastal bathymetric changes in only an hour [4]. The aim of nearshore science is to describe, predict and monitor coastal waves, currents and water depth within a broad littoral domain by combining a large number of available experimental measurements and numerical modelling to improve the three-dimensional description of coastal dynamics.

Despite the importance in observing coastal dynamics, sampling devices are still scarce due to the difficulty of taking measurements. In-situ bathymetric surveys have traditionally been conducted through on-board sonar-based devices or using a survey rod for shallower points, which has to be held while the height of the submerged side of the target rod is recorded when it moves trying always to touch the seabed. Thus, water depth data are sparse and the uncertainty of measurements is large owing to low accuracy in the sampling system that hinders the bathymetry data collection during periods of large waves or strong nearshore currents [4], [21].

Sampling requirements for successful monitoring coastal processes are mainly determined by their rapid variability. Surface waves have periods of $O(10s)$, infragravity waves, and longer group waves in general, move with $O(30 - 300s)$ periods, whose instabilities in alongshore currents arise in very-low wave frequencies with periods ranging from $O(10^2 - 10^3 s)$, even though disregarding extreme wave events like storm and hurricanes. Therefore, acquisition

systems with a sampling rate between 1-10 Hz can meet the nearshore high-frequency needs in the time domain [1]. Regarding spatial cross-shore scales, wave currents, wave motions and water depth change significantly in nearshore areas [1]. Hence, proper sampling of coastal variability would need a large array of in-situ sensors to characterize a significant region. This ideal spatial sampling situation represents a slow, expensive and labour-intensive task. As a general rule, spatial resolution improvements involve restrictions in the time sampling domain and vice-versa. Remote sensors map hundreds of meters over wide areas during short time-scales at the expense of higher computational needs and lower accuracy data because they only acquire superficial ocean data unlike in-situ measurements. Moreover, ocean observations can be classified in three main groups depending on the inherit characteristics of the measurement devices.

- **In-situ and stationary sensors.** These instruments provide high temporal resolution data being limited to the single seabed location where they are deployed. Therefore, the description of coastal processes is usually expanded by using numerical modelling simulations. Wave currents and sea state properties, such us significant wave height (H_s or H_{m_0}), peak wave direction (θ_p), maximum wave height ($H_{\max}$), peak wave period (T_p) and peak wave frequency (f_p), can be directly measured using *Acoustic Doppler Current Profilers* (ADCP). The sensor measures wave current speed and direction using sound pulses ranging from 40 to 3000 kHz, which are reflected by small particles (e.g. fine silt or plankton) drifting with the current [29]. Doppler effect allows the acoustic three-dimensional measurements of wave current, considering that the frequency shift of the echo signal is proportional to the velocity component measured by the three oblique transducers of the sensor [29], [30]. Regarding sea state data, only the sea surface layer of the water column is considered applying the simple echo-sounder principle over the central vertically oriented transducer of the ADCP sensor. It transmits a very short pulse relative to the Doppler measurements. Bottom-mounted pressure gauges, such as *Acoustic Doppler Velocimeters* (ADV), use the same procedure described above for ADCP devices [9].

- **Observation with mobile systems.** These sensors move in an autonomous way or by following the ocean dynamics. They can also be deployed at mobile platforms such as ships or planes. Traditionally, expensive vessel campaigns have been performed to characterize small ocean areas during short periods. Recently, *Autonomous Underwater Vehicles* (AUV) and coastal gliders measure many physical, chemical and biochemical variables such as temperature, salinity, oxygen and chlorophyll along the water column by autonomous moving that is only restricted by the battery load [31]. Despite the spatial coverage increases, the sampling frequency is reduced.

- **Observation with remote sensors.** They measure the strength of the electromagnetic radiation to provide a large footprint of the observed nearshore dynamics, transforming the received intensities into a physical variable. These devices can be deployed either at fixed locations, e.g. towers, or at mobile platforms like satellites. Wave shadowing and spatial resolution degradation along distance are the strongest hurdles to deem fixed remote sensors as robust coastal monitoring devices. Instead, *Synthetic Aperture Radar* (SAR) satellites [32], [33] have been considered as the most mature overhead moving platforms with accurate analysis methods [1]. Although satellite imagery cover global areas, their capabilities as coastal mapping devices are usually daunting because of their limited dwell capability and spatial resolution [1].

Remote sensors can be active or passive, namely emitting-receiving or only receiving devices. Satellite-altimeter for Sea Surface Height (SSH) estimation [34], *Laser imaging Detection and Ranging* (LiDAR) systems, high-frequency (HF) and marine radars are active sensors that extract some wave properties through the modification of energy spectra and statistical attributes. Although marine radars can operate at both S-Band and X-Band wavelengths, X-Band radars are the most appropriate devices to sample the complex nearshore seabed variability at high frequencies. They cover large areas, out to 1-3 km, using wavelengths of 3 cm and 5-10 cm spatial resolution. According to Table 2.1, HF wavelengths are too coarse for nearshore applications.

In contrast, passive remote sensors use the energy received from natural emitter (e.g. the long-wave thermal radiation or the short-wave solar radiation reflected by a surface [35]) to estimate sea surface parameters. Optical and infrared (IR) cameras are passive sensors that rely on ambient sources of illumination from the local sea surface in the visible and the IR bands, respectively. Optical wavelengths spans from 400 (violet) to 700 (red) nm whereas thermal wavelengths are much longer ranging from 700 nm to 300 μm. Since optical video-cameras depend on the interaction of sun light with the dielectric surface of the ocean, reflection and refraction phenomena define the upwelling sea surface radiation. Unlike optical cameras, IR energy is directly radiated by the ocean even at night. However, turbulence often distort the sea surface signature with patchy patterns [1].

TABLE 2.1: IEEE standard letter designations for radar-frequency bands [36].

Frequency Band	Range of frequencies	Wavelengths
HF	3 - 30 MHz	100 - 10 m
VHF	30 - 300 MHz	10 - 1 m
UHF	300 - 1000 MHz	1 m - 30 cm
L	1 - 2 GHz	30 - 15 cm
S	2 - 4 GHz	15 - 7.5 cm
C	4 - 8 GHz	7.5 - 3.75 cm
X	8 - 12 GHz	3.75 - 2.5 cm
Ku	12 - 18 GHz	2.5 - 1.67 cm
K	18 - 27 GHz	1.67 - 1.11 cm
Ka	27 - 40 GHz	11.1 - 7.5 mm
V	40 - 75 GHz	7.5 - 4 mm
W	75 - 110 GHz	4 - 2.7 mm
mm	110 - 300 GHz	2.7 - 1 mm

2.4   X-Band Marine Radar

Since the 1980s, X-Band marine radar has devoted as remote sensing devices that describes wind and wave dynamics [37]–[39]. X-Band radars employ frequencies between 8 and 12 GHz, recognizing the sea surface signature, usually named *sea clutter*, through backscattering and Bragg resonance interactions. Although commercial X-Band radars filter the sea clutter for navigation and surveillance on-board ships, these electromagnetic signals have relevant information to describe sea state [40]–[42]. The electromagnetic signal transmitted by a radial displacement of the radar antenna (between 1°-3° wide in azimuth) is reflected off short capillary waves and other features, whose wavenumber is comparable to the wavelength of the transmitted
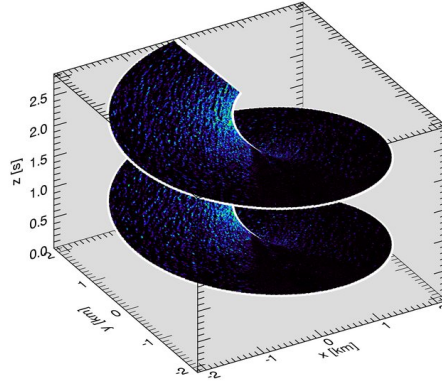
Figure 2.1: X-Band marine radar spiral data acquisition considering only two antenna rotation cycles [52].

signal (i.e. wavelength $\lambda \approx 3$ cm). Besides, the microwave pulses are electrically generated by either horizontal-transmit-horizontal-receive (HH) or vertical-transmit-vertical-receive (VV) polarization with different backscattering characteristics for each one [1]. Thus, the roughness of the sea surface can be geometrically defined considering echo intensities and time differences between radar-emitted waves and received signal [43], [44]. Appendix C describes in detail the basic concepts and operation of a pulse X-Band radar system to acquire sea clutter data.

The mathematical description of sea clutter, MTF (*Modulation Transfer Function*), describes the modulation of centimetric surface waves on water by longer waves through the incident radar signal affected by the statistical properties of the ocean dynamics [45], [46]. MTF considers aerodynamic, hydrodynamic, tilt and shadowing modulation. Aerodynamic modulation defines capillary waves through wind-sea interaction. Hydrodynamic modulation of short sea surface ripples determines the amplitude and phase of modulated longer waves, making them visible on sea clutter radar images. Besides, tilt modulation considers that wave slope variations lead to changes on effective incident angle of the radiated electromagnetic signal. Finally, shadowing occurs when higher waves obstruct microwave backscatter from smaller one, mainly during low grazing angle radar measurements [40], [47]–[51].

The raw sea clutter images are obtained by the continuous rotation of the radar antenna providing polar coordinates images in space-time domain. Then, radar images are interpolated to a Cartesian grid. Figure 2.1 reproduces the backscattered data from X-Band radars as a spiral staircase in a spatio-temporal cube instead of snapshot images from sea surface [52], [53]. However, for practical reasons, the radar backscatter recorded during each antenna rotation are assumed to be a spatio-temporal snapshot of the nearshore area.

X-Band marine radar has been used in several ocean applications including target tracking [54], oil spill detection [55], surface current determination [56]–[59], coastal upwelling observation [60], tide estimation [61], bathymetry mapping [62], [63], coastal erosion [64], surface elevation estimation [65], [66] and prediction [67], [68]. Relevant commercial products have been developed by exploiting the maturity and accuracy of X-Band radar measurements. For instance, WaMoS II (*Wave and Current Monitoring System*) digitalizes and saves sea clutter images through the *Dispersive Surface Classificator* (DiSC) algorithm, assuming stationary and inhomogeneity wavefields at offshore platforms, coastal stations and moving vessels [39], [69]–[71]. The acquisition system

scans sea surface with a spatial resolution of 5-10 m [72], [73] and measures directional wave spectra, H_s, f_p, θ_p, bathymetry and wave current speed [8], [9], [68], [69]. However, WaMoS II does not consider algorithms to mitigate shadowing effects in nearshore areas and cannot provide water depth data in strongly non-linear wavefields, i.e. $h > $ -4 m [71]. SeaDarQ [74] and Sigma 6 [75] systems allow the detection of oil spills and measure some wave parameters. However, the additional application of oil spill detection significantly increases the selling price (e.g. Sigma S6 + WaMoS II hybrid system costs about $ 115,000 USD [76], [77], similar to the directional wave buoy price). Radac system [78] is an offshore monitoring tool that uses a static marine radar deployed on an offshore structure similar to conventional wave buoys. Since this radar needs to be installed in the ocean, it has the same drawbacks of in-situ sensors.

Regarding wave properties estimation, non-coherent X-Band radars perform either spectral or texture analysis techniques to retrieve sea state information. For wave spectral analysis, wave parameters are usually estimated through wavenumber-frequency spectra of raw-radar time series using three-dimensional Discrete Fourier Transform (3D-DFT). In contrast, wave-retrieval algorithms based on texture analysis obtain wave parameters directly from the image texture without the estimation of wave spectra [37]. This section is devoted to examine previous radar-derived wave measurement algorithms in both spectral and texture approaches, comparing their performance and discussing their pros and cons for coastal applications.

Wave Spectral Analysis Techniques

Spectral inversion schemes have been broadly used for estimating wave properties analyzing time-sequence of sea clutter images in frequency domain. In this technique, consecutive rectangular sub-images are extracted and normalized subtracting the temporally-averaged radar intensity of each pixel. Then, directional wave spectrum is obtained starting from the three-dimensional Fast Fourier Transform (3D-FFT) of processed radar images in the test region. A large number of studies and commercial monitoring systems use this method to obtain wave properties from marine radar imagery [39], [44], [56], [57], [69], [79]–[84].

Izquierdo *et al.* [43] and Nieto-Borge *et al.* [42], [82] estimate H_s, peak wave direction θ_p, wavenumber vector $\vec{k} = (k_x, k_y)$ and peak frequency f_p from radar imagery in deep water waves. They use the linear wave theory to filter the 3D-FFT and obtain the directional wave spectrum. However, H_s estimation requires a previous empirical calibration using the square-root of measured signal-to-noise ratio (SNR) derived from in-situ sensors like buoys. Additionally, the calibration procedure depends on radar antenna location [82], [85]. SNR calibration originates from a SAR technique [82], [86] which considers that radar-derived wave spectra are not properly scaled whereby wave height cannot be directly determined. The performance of SNR-based methods relies on significant water depth changes and the local wind speed, showing correlation coefficients (CC) and root mean squared (RMS) differences of 0.71-0.89 and 0.18-0.42 m, respectively [37].

In contrast, Vicen-Bueno *et. al.* [87] proposed a non-linear model based on Artificial Neural Networks (ANN) with multilayer perceptrons (MLP) to improve H_s estimates, even under low wind speeds and swell-dominated sea state conditions. Although the CC between radar-derived

and buoy-measured H_s are higher than 0.96 and the RMS differences are lower than 0.27 m, SNR calibration is still used, in this case, as an input parameter for MLP method. Ma *et. al.* [88] proposed an array beamforming algorithm based on a spatial filtering methodology to estimate wave parameters and directional wave spectrum using X-Band marine radars. This algorithm considers each pixel as elements in a circular antenna array, obtaining CC in order of 0.95 and mean bias error of 0.28 m between H_s estimation and in-situ measurements. However, the array beamforming algorithm still uses SNR calibration and it does not consider heterogeneous wavefields [37].

Lund *et. al.* [52] examine the wave radar data dependency on range and azimuth. They remove the azimuth dependency in H_s estimates using least-squares fitting and Fourier series, but still considering deep water data. However, they suggested that the azimuth dependence could be neglected in coastal areas since waves approach towards shoreline, unlike offshore stations [52]. Lund's method provides robust wave parameter measurements when the radar field of view is partially obstructed in contrast to adaptive recursive positioning method (ARPM) proposed by Al-Habashneh *et al.* [89], which estimates wave properties under binomial (i.e. wind waves and swell) sea state conditions in deep water waves. ARPM requires a full radar field of view to average the wave spectra from several sub-images in different azimuthal directions [37].

Regarding coastal monitoring, Nieto-Borge *et al.* [80] proposed an empirical MTF correction as an extension of the traditional inverse modelling technique applied in shallow waters [42], [43], [82]. This mathematical approximation describes radar backscattering at HH polarization using a constant MTF of $|M(k)|^2 = k^\beta$, where $\beta = -1.2$ [80]. However, this function was determined using offshore radar data collected at deep waters, assuming a stationary and homogeneous wavefield [80]. In coastal regions, the variation of range and azimuth cannot be neglected and the linear MTF with a constant exponent does not work properly. In this context, Chen *et al.* [90] proposed a new quadratic polynomial MTF using a VV-polarized radar, but they only compared the buoys-measured peak and mean wave periods with the radar-retrieved data. Additionally, the sea clutter images in [80] were obtained by a permanent WaMoS II station at 100 m above the mean sea level, where shadowing has a minor impact on radar imaging and grazing incidence angles are not extreme [91]. WaMoS II system was also deployed at oil rigs, such as Ekofisk [91] and Glas Dowr [92], whose heights are beyond 50 m above the sea level and shadowing modulation is still insignificant [8], [91]. Vogelzang *et al.* [93] used WaMoS II device to measure H_s, θ_p and T_p at 10 m above the ground. Results show that H_s, T_p and θ_p were retrieved with 20% (about 30 cm), 0.6 seconds and 9° of error, respectively. However, WaMoS II data needed to be calibrated using a reference directional WaveRider buoy located at about 600 m offshore.

Considering shallow water heterogeneities, Chuang *et al.* [94] and Wu *et al.* [95] proposed a 2D continuous wavelet transform (CWT) to obtain wave spectra from X-Band radar imagery. An *et al.* [96] improved the previous 2D-CWT approach suggesting a self-adaptive algorithm to select the wavelet scaling parameters for wave properties estimation. Although the self-adaptive 2D-CWT-based method uses a single radar image, the computational cost is expensive, the RMS differences of H_s tend to be of $O(0.61m)$ and the wave directional ambiguity cannot be eliminated in the radar-retrieved wavenumber spectrum.

Recently, Greenwood *et al.* [65], [66] proposed a novel methodology to approximate sea surface

elevation η using a second order Stokes wave model in regions where radar shadows occur. Field data were captured by a SeaDarQ system with a VV polarized radar antenna. They generate artificial wavefields to minimize shadowing effects where required. CC of η approximation range from 0.56 to 0.69. For H_s and T_p, CC are 0.62 and 0.41, respectively, by comparing nearshore phase-resolved wave data, ADCP and wave buoy measurements. However, this method still needs calibration of X-Band radar data to scale H_s.

Serafino *et al.* [64], [97]–[101] proposed the Normalized Scalar Product (NSP) to estimate wave parameters, bathymetry, shoreline and surface currents in harbours. NSP method is based on spectral analysis and filtering of overlapping sea clutter regions considering the dispersion relation. The method proposes maximizing the normalized power scalar product between the magnitude of the image three-dimensional spectrum and the linear dispersion relation. Bathymetry estimation results show a mean bias error of 1.2 m. A novel commercial coastal monitoring device, REMOCEAN system [102]–[104], uses this approach to survey coastal dynamics. Although NSP has been tested in coastal areas, it follows the empirical MTF proposed by Nieto-Borge *et al.* in [80] that was obtained using offshore measurements [99]. Recently, Ludeno and Serafino [105] combined tidal and shadowing modulation approaches with the original NSP method to avoid external calibration. However, CC of H_s estimates are still of $O(0.7)$, even though they only use simulated radar wavefields.

Texture Analysis Techniques

Although traditional H_s estimation requires external calibrations, some texture-based techniques, such as tilt- [91] and shadowing-based [106] algorithms, have been proposed to remove calibration procedure and the estimation of wave spectra. Nevertheless, they are mainly developed for either infinite deep water or large incidence angles conditions. For instance, Dankert *et al.* considered tilt modulation to estimate H_s using marine radar imagery without calibration [91], [107]–[109]. However, the antenna was installed on oil rigs at deep waters, avoiding shadowing modulation and non-linear behaviour in shallow water areas [91]. Figure 2.2 illustrates the tilt- and shadowing modulation of the ocean waves through X-Band radar systems.
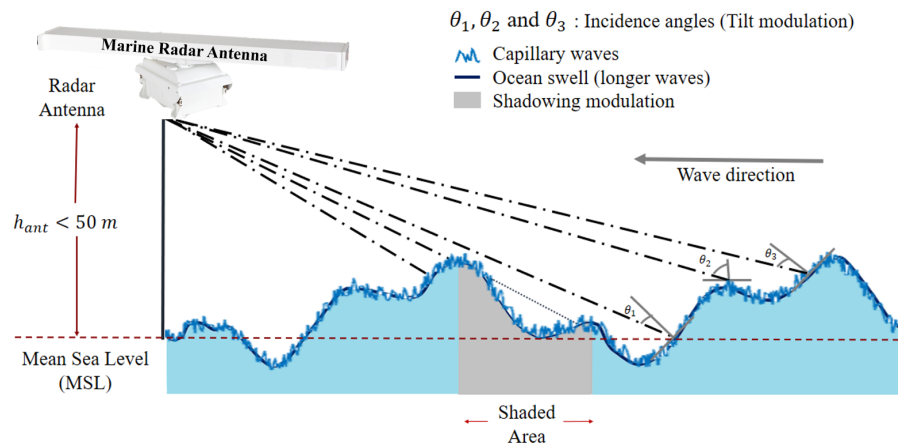
Figure 2.2: Tilt and shadowing modulation scheme for onshore microwave X-Band radar systems [2], [40].

In this regards, Plant and Farquharson [110] investigated two types of shadowing, namely geometric and partial shadowing in deep waters. They suggested that geometric shadowing is a poor description of backscatter from low grazing angles. However, it is difficult to distinguish between these two types of shadowing because SNR differences are very small [111]. Geometric optics theory has been used for estimating H_s through the probability of illumination P_0, as proposed Buckley and Aler [112]. This theory suggests that the peak-to-trough ratio (i.e. the illuminated areas reflected from visible wave portions) decreases as the wave height increases for a given P_0, emerging a large number of areas with no reflection due to shadowing. Shadowed areas are identified by a pixel-by-pixel threshold, in which intensity levels that are lower than the constant threshold are affected by shadowing whereas others are illuminated. However, a constant threshold value cannot be applied for different sea states. Thus, CC of H_s tend to be of order 0.54 [37].

Gangeskar [113], [114] proposed an image shadow statistical analysis to estimate H_s. This method is based on principles of geometric shadowing and band pass filtering obtaining CC of 0.67. However, it considers infinite deep water conditions [106]. Later, Gangeskar [106] also introduced a calibration-free shadowing-based algorithm that can be used even at grazing incidence conditions. This algorithm adds edge detection, threshold techniques and single noise filters to the previous procedure, incorporating sea surface slope and the average zero-crossing wave period. However, the test use the peak period derived from an external reference buoy instead of the radar estimation, still depending on in-situ measurements. An improved method is proposed by Liu *et. al.* in [115], [116]. They smoothed the edge pixel intensity histogram to select a more robust shadow threshold that yields high CC of H_s (i.e. 0.81). However, this method is only applied over a short sub-area (e.g. 5°) where radar backscatter meets wind direction. Wei *et. al.* [111] includes the water depth (*h*) to estimate H_s, but CC do not exceed 0.68 between radar-derived and buoy-measured H_s data.

Salcedo-Sanz *et al.* [117] carried out sea state measurements on a FINO 1 platform, where shadowing cannot be neglected. A SVR (*Support Vector Regression*) computer-aided algorithm was trained to remove calibration and to estimate H_s using simulation-based data [117]. However, SVR neglects diffraction effects and estimates of H_s are only accurate up to 1.5 m. According to this study, X-Band radar antennas installed in low grazing incidence conditions cannot detect sea state when local wind speed is lower than 3 m/s because it does not induce enough roughness on the sea surface [117].

Recently, Chen *et al.* [118] estimated H_s, T_p, θ_p and wavelength through the principal components (PC) of radar time-sequences derived from an empirical orthogonal function EOF-based algorithm (EOF-PC). Instead of linear wave theory and MTF formulation, H_s is estimated from an empirical relationship with the standard deviation of any one PC z_i from the 2D time-space image sequence Z given by, $H_s = A + B \cdot \text{std}(z_i)$. However, calibration procedure is necessary to obtain A and B empirical coefficients by using external sensor data, e.g. wave buoys. Besides, the method uses deep water dataset and it is affected by the selected area and pixel position. Yu *et al.* [119] and Zhang *et al.* [120] considered a rotated EOF (REOF) to estimate H_s. However, the calibration is still required, similar to the Ensemble Empirical Mode Decomposition algorithm proposed by Liu *et al.* in [121]. Chen *et al.* [122] also included a joint PDF of dimensionless

wave periods and wave heights to estimate the calibration coefficients of H_s without external reference data and using nearshore X-Band radar dataset. Joint PDF method is an extension of the EOF-PC algorithm. However, the performance needs to be improved relative to the SNR- and shadowing-based algorithms because CC of H_s are lower than 0.78 [37].

2.5   Optical Video-Based Monitoring Systems

Optical video cameras provide continuous sea state measurements from the ocean surface radiation in the visible band, usually neglecting upwelling and direct sun radiances. The modulation transfer function in optical imagery relates the differences in reflection and intensity with the true waveform and the sea surface slope. Therefore, MTF depends on the mechanism used for imaging ocean waves by the camera. For nonbreaking waves, the main mechanism is the *specular reflection* of the incident light on the sea surface, which relies on the direction of wave propagation and the camera looking angles. The specular radiation assumes the sky radiance is isotropic and homogeneous. Hence, the observed radiance depends on Fresnel reflection coefficient [123], [124]. However, strong brightness variations occur at non-linear surface slope that hinder the identification of clear wavefields. The breaking waves radiance in the surf zone relies on the diffuse reflectivity from the whitecap that is observed from the *isotropic scattering* mechanism [123], [124]. In this case, radiance is not closely related to the viewing geometry but the remnant foam must be removed for correct wavefield isolation.

With regard to nearshore remote sensing, video-based monitoring systems can estimate bathymetry, shoreline and in some ways wave parameters through conventional video imagery products including snapshot, time-exposure or *timex*, time-variance and timestack images [125]. Figure 2.3 shows a set of common video-based beach monitoring facility products at Tairua beach, New Zealand, which is considered as a case of study in [125]. Figures 2.3a to 2.3c (i.e. snapshot, *timex* and variance images, respectively) are oblique with resolution 2016×1528 pixels. The cross-shore black line in Figures 2.3a to 2.3c is used for building a timestack image with 10 minutes of time exposure at 2 Hz, as shown in Figure 2.3d [125].

Snapshot images yield beach features that are useful for coastal management (e.g. quantification of beach users [126], [127]) and geomorphological coastal studies (e.g. detecting beach cusps [128]). *Timex* images corresponds to the average in time domain of a large set of snapshot images, usually 10 minutes of video imagery, which allow the assessment of shoreline evolution [129]–[133], wave breaking and submerged bars migration in the surf zone [134]–[136], rip currents [137] and video-derived intertidal [138] and subtidal [139] bathymetry. Moreover, variance images reproduce the standard deviation in time domain from a set of snapshots [140] and they have been used for delineate wave breaking regions [141]–[143], runup and mean shoreline detection [125] obtaining accurate estimations. Time-sequences of video imagery used for *timex* and variance images are usually deleted once these products have been computed to reduce memory requirements. In contrast, timestack is a synthetic image that depicts the evolution of a given cross-shore beach transect in time (vertical axis) and space (horizontal axis) dimensions, as shown in Figure 2.3d [125]. Timestacks allow the study of swash zone including runup statistics
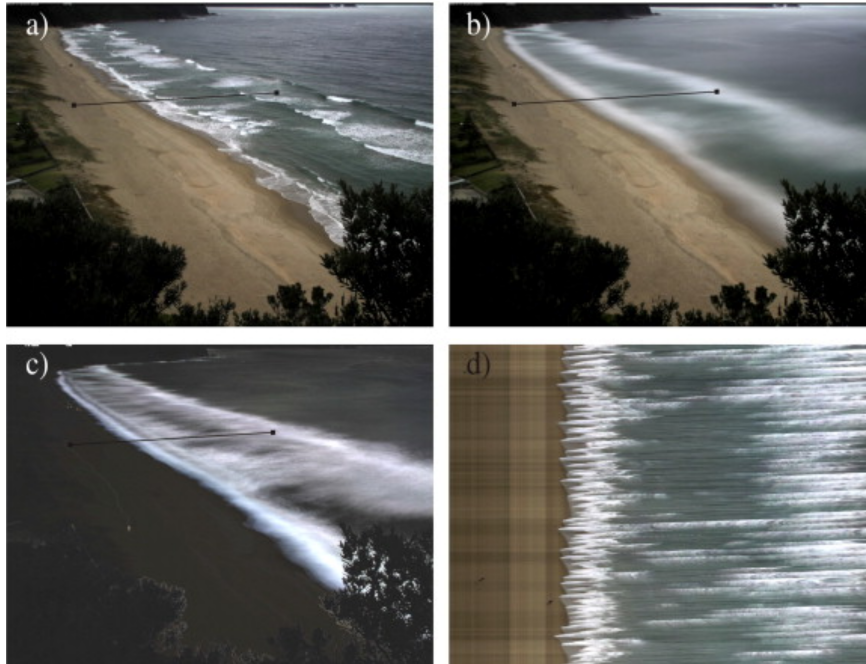
Figure 2.3: Traditional products from video monitoring stations, Tairua beach, New Zealand, as a case of study: **(a)** snapshot image, **(b)** time-exposure or *timex* image, **(c)** time variance image and **(d)** timestack image [125].

and shoreline evolution for a limited number of cross-shore locations instead of the whole field of view of the camera [4], [144].

Nieto *et al.* [145] presented a detailed comparison of some commercial and automated coastal video monitoring systems such as ARGUS, SIRENA and HORUS. ARGUS coastal stations, developed by Coastal Imaging Laboratory at Oregon State University in the 1990s, were the pioneering in video-based monitoring [140], [146]. It consists of a number of optical cameras installed together at a tower, looking downward at different directions in order to completely cover the beach [146]. However, users cannot personalize ARGUS facilities [140], [147]. The Mediterranean Institute of Advanced Studies (IMEDEA) developed SIRENA and ULISES [145], [148], [149], two open-source software conceived with the objective of video monitoring dynamical systems. HORUS, developed by University of Cantabria and National University of Colombia, is able to estimate waves, shoreline evolution and the number of beach users employing snapshots from high resolution video cameras [150], [151].

Although optical systems have a higher sampling rate (0.1-1 Hz) and a denser spatial resolution for shallower pixels (~1 m) than X-Band radars, video-based monitoring systems are unable to scan sea state during night. Hostile weather conditions during measurements (e.g. fog, low wind or rain) also contributes to degrade their performance. Besides, it is nearly impossible to estimate significant wave height (H_s) due to optical limitations and they cover smaller areas than X-Band radars, of about 1 km. Therefore, X-Band radars are becoming widely used in coastal monitoring because of their flexibility and their fine spatial and temporal resolution in comparison with in-situ sensors and others remote sensing techniques, such as satellites, synthetic aperture radar (SAR) imagery and high-frequency (HF) coastal radars [42], [64].

2.6   Bathymetry Estimation and Shoreline Detection

Water depth and shoreline are the most critical variables for modelling nearshore variability that can be surveyed through several direct or indirect remotely sensed products [4], including LiDAR techniques [152], [153], satellite images [154]–[158], video images [16], [21], [159], infrared [160], [161] and X-band radar imagery [80], [162]–[164]. Direct bathymetry survey techniques are highly dependent on optical clarity of sea waters and bottom reflection. They use remote sensing devices such as spectral satellite-airborne technology and LiDAR instruments, but water depth is usually overestimated by several meters using these expensive devices [4].

In contrast, indirect water depth measurement requires *a priori* wave properties estimation (e.g. wave celerity and wave frequency) considering the remotely sensed intensities as a proxy of the ocean surface signature. Then, bathymetry can be inferred by applying either frequency-domain (e.g. 3D-FFT method [165]) or spatio-temporal domain (e.g. phase gradient method [166], [167]) inversion algorithms based on the linear wave theory. The accuracy of depth inversion methods, including 3-D spectral analysis, time-exposure images and time-stacking techniques, depends on the capability of the remote sensor to estimate wave speed and wave amplitude with high accuracy and the applicability of a correct algorithm to relate wave data with water depth, even in non-linear regions [123]. Indeed, phase gradient method returns ten times finer high-resolution bathymetry than 3D-FFT-derived water depth estimates [166].

Stereo video-based imagery have been the most powerful and low-cost tool for coastal remote sensing [134], [168], which were initially used for morphological observation of shoreline and sandbar migration. However, video data also describe runup, wave energy dissipation, swash velocity and nearshore water depth. Bathymetry can be obtained from video images using timestack analysis [4], i.e. 1D space, or considering the whole 2D image by using cross-spectral method and Principal Component Analysis (PCA).

The *cBathy* [21], [159], [169] algorithm is the most widely used for video-derived 2D water depth estimation, which considers two main stages: first, a depth inversion procedure combining the linear dispersion relation and wave phase fitting for each hourly video; second, a Kalman filter to smooth the hourly estimated depths updating the previous depth points with the new estimates depending on the Kalman gain. Therefore, each pixel intensity is transformed to the frequency domain to obtain water depth from the EOFs of the Cross Spectral Matrices (CSMs) in a neighborhood of each given point. The analysis of the set of CSMs yields dominant frequencies and wavenumbers to estimate different water depths and a weighted average of them $\bar{h}$, which is then smoothed in the time domain through the Kalman filter. Although *cBathy* is a robust depth inversion method for micro/meso tidal environments, it needs to be modified considering the effect of the tide on the water depth estimation in a highly energetic macro-tidal domain, as shown in [169].

Bergsma *et al.* [169] revealed that water depth estimation using *cBathy* is significantly less accurate on the inter camera boundaries in a stereo-video system and the bias error tends to increase when tidal range also increases. Therefore, a parallel depth estimation using only pixels from single cameras is carried out. Then, depth estimates are combined by a weighted average considering the centre of mass of each location to overcome camera boundary issues. Besides,

floating pixels are considered instead of fixed geographical locations to include tidal elevation in *cBathy* code. However, the reduction of RMS error is found only for limited wave heights, i.e. lower than 1 m, because *cBathy* exhibits limitations dealing with high wave heights, wet/dry tiles and long waves [146], [170].

The inversion method presented in this doctoral dissertation is based on the idea of the *uBathy* approach [16] by determining the wavenumber and wave frequency through the time-series of pixel intensities, which is fully detailed in Chapter 6. It was originally designed to infer nearshore water depth through cross-spectral matrix and PCA of the Hilbert transform from video images. However, a new application using X-Band radar systems is discussed in Chapter 6. Appendix D provides more detailed description about Hilbert transform.

Catalán and Haller [23], [123] reviewed a large number of models for nonbreaking (e.g. linear theory and Boussinesq wave theory), breaking waves (e.g. Bore [171] and Shock [172] models) and waves in the transition between these two zones, i.e. intermediate depths where *kh* ranges from 0.15 to 0.81 (e.g. Kirby and Dalrymple *KD86* model [173], Hedges [27] and Booij [28] models), to obtain phase speeds and depth inversions using a hybrid dataset that combines video cameras, in-situ wave gages and model-generated wave amplitude profiles. Data were collected from a large-scale laboratory experiment using a fixed bathymetry and a single submerged bar. Results show that *KD86* and Booij composite models provided the best agreement in surf and intermediate zones, highlighting the simplicity of Booij model for practical applications. However, wave speed is computed by edge detection using timestack images in 1D space, which are not as robust as 2D depth inversion algorithms. Similarly, Flampouris *et al.* [174] found *KD86* as the best performance non-linear model relative to the modified cnoidal and Hedges models, but using X-Band radar data.

For X-Band radars, the pioneering study in shallow water bathymetry estimation is presented in [164], which recommended the inclusion of higher order wave models to improve the accuracy of the over-predicted shallower h, mainly when $h > $ -6 m [165]. Errors are up to $\pm$ 2 metres [57], [175], [176] in the intertidal zone, even using nested radar systems [177]. It was also suggested by Trizna in [178], [179]. DisC [71], [175] and NSP [64], [97], [99], [101] algorithms used in WaMoS II and REMOCEAN wave monitoring commercial products, respectively, are the most popular radar-derived depth inversion methods. They provide morphological information based on spectral analysis of time-sequence radar images (3D-FFT) and filtering techniques using the linear dispersion relation. Recently, Ludeno *et al.* [97] added a modification to NSP algorithm considering an adaptive spatial partitioning dimension of the radar overlapping sub-images, according to the local peak wavelengths estimates. This strategy provides more accurate bathymetric estimates than the original NSP space-invariant partitioning procedure with CC higher than 0.94, but only for $T_p > 7.5$ s and $h > $ -15 m. Method shows poor performance in deep and intermediate waters. Rips currents are also identified in [64].

Bell and Bird *et al.* [180], [181] introduced the *Temporary Waterline* depth inversion method for long-term intertidal bathymetry estimation that evaluates high/low changes in hourly averaged-radar pixel intensity, which are closely related to tidal variation and wet/dry transitions. Field data were obtained at about 30 m height above the sea level [57], [182] through WaMoS II system and POLPRED software. This latter uses a model based on harmonic constants and the type

of tide in offshore operations. Since *Temporary Waterline* algorithm depends on tidal changes, measurements must be performed during long periods of time (i.e. at least two-week to observe the full spring-neap cycle) with considerable spatial resolution to avoid significant bias errors.

Wu *et al.* [63] proposed a depth inversion algorithm based on image decomposition techniques and Hilbert transform to estimate the local wavenumber from radar images using single-period wavefields. Since the wave period is constant during wave propagation, a spectral filtering of the power density is carried out on individual pixels to obtain the monocomponent signals using 1-D inverse FFT (IFFT). Then, the Hilbert transform yields the imaginary part of the signals and the signal phase can be estimated from the phase derivative. The gradient of the local phase allows the estimation of the local wavenumber along *x-* and *y-directions*, i.e. $\overrightarrow{k} = (k_x, k_y)$. Hence, wave phase speed and water depth can be estimated considering the most frequency wavenumber from each location. Although the computational complexity is lower than DisC and wavelet transform methods, the isolated wave periods are limited to T_s greater than 7 s because wave patterns are sufficiently clear.

Besides, McNinch [163], [183] developed a *Bar and Swash Imaging Radar* (BASIR) to measure water depth, shoreline, runup and sandbars in swash and surf zones throughout large alongshore distances (5-10 km), especially during storm events. BASIR is a mobile X-Band radar mounted on a beach vehicle with a dual-channel global positioning system (GPS) to map the nearshore morphodynamics at very low grazing angles. It uses a fixed antenna height, i.e. 3 m elevation above surface level, a sampling frequency of 0.4 Hz and a modest power of ∼12 kW. However, large wave heights are required for breaking wave detection and wave parameters have not been estimated yet using BASIR system. Moreover, data collection is not carried out while the vehicle is moving along the beach. Instead, the X-Band radar only can move to new location once it has collected 8-10 minutes raw-radar images in the previous position.

Regarding coastline detection, there are a widespread number of applications based on digital coastal images including aerial photographs, LiDAR data and ARGUS video systems which have been documented in [184]. In particular, stereo-video systems use time-exposure [185], [186] and time-variance [17], [125] images to extract proxy shoreline features, being the high-water line (HWL) the most common discernible shoreline indicator to represent the *true* shoreline position [184]. Recent studies about video-based shoreline detection also include image processing techniques such as edge detection, automatic threshold detection, binarization based on the distribution of color intensity in the RGB histogram, erosion and dilatation techniques, image subtraction, supervised classification, adaptive filtering and smoothing approaches, similar to satellite imagery methods [156]–[158], [187].

Among the variety of data sources, X-Band radars have not been widely used as shoreline mapping devices. However, they can automatically surveyed morphological changes (e.g. seabed features, water depth estimates and shoreline variations) over large distances even during storms [163], [183] in order to support coastal management decisions using time-averaged images [188]. However, manual corrections is sometimes required, especially in irregular wave breaking areas [163].

2.7 Merging Marine Radar and Optical Video-Based Systems

Several studies use both optical and microwave data to measure nearshore dynamics, including swash and wave breaking zones. Haller and Lyzenga [189] introduced the pioneering shallow water wave breaking comparison between radar and video observations at intermediate grazing angles. Sensors are accurately synchronized and geolocated. Wave breaking regions are identified by an empirical threshold procedure. Results show that radar is less sensitive to persistent high-intensity foam on the sea surface. Therefore, breaking and nonbreaking waves are identified with less tuning using radar imagery. Similarly, Ruessink *et al.* [162] measured sandbar location from time-averaged X-Band radar images and *timex* video imagery also tracking the maximum intensity with good agreement.

Regarding low grazing angles, Catalán *et al.* [124], [190] analyzed intensities and different scattering features between radar and video sensors in the surf zone to classify breaking and nonbreaking regions through a *Joint Probability Density Function* (JPDF). In [163], shoreline and nearshore sandbar locations are measured by the mobile X-Band BASIR system and then estimations are compared with video-derived data and in-situ measurements. Results show high correlation between radar and ARGUS sandbar estimates whereas water depth is under-predicted relative to in-situ bathymetric profiles. Besides, radar antenna position and orientation is crucial to define the *Bar and Swash Imaging Radar* system accuracy.

Perkovic *et al.* [191] measured long-shore surface currents using Doppler radar and *Particle Imaging Velocimetry* (PIV) video data. Shoreline was only detected from video-derived timestack images. Both marine radar and video systems were deployed at 73 m above sea level, neglecting shadowing modulation effects. Although radar and stereo-video imagery rely on different measurement mechanisms, reasonable accuracy was found with CC of about 0.78. However, differences between radar- and video-derived velocity estimates increase as range also increases because the spatial resolution of both systems degrades at seaward direction. Thus, the cross-shore pixel geolocation of two data sources may not be aligned. Differences between radar and video estimates in the surf zone were mainly attributed to inappropriate image-to-ground coordinate transformation, lack of synchronization and lens distortion of video cameras. In contrast, Benetazzo *et al.* [192] suggested, as a future research, the use of directional properties of stereo imagery to find the best radar MTF and scale calibration factor, after comparing the directional wavenumber spectra from radar and video overlapping wavefield regions.

Rutten *et al.* [146] estimated nearshore bathymetry from VV polarized marine radar data and optical video imagery, neglecting the correction for finite wave amplitude dispersion in non-linear wavefields. Depth inversion was carried out using 3D-FFT and *cBathy* algorithm from radar and video time-sequence images, respectively. According to bias and RMS errors, they defined three depth ranges, namely shallower, intermediate and deeper water regions. Limits of depth ranges are different for both microwave and optical sensors. Intermediate depth range is the best agreement zone for both video and radar systems relative to in-situ data. Bias error from radar images is up to -2.3 m in shallower depths because of FFT accuracy depends on window size, sequence length and homogeneous wavefield in the region of interest. As stated in [146], FFT method yields larger bias and RMS errors than cross-spectral algorithms in shallow waters.

Indeed, this doctoral dissertation evaluates a cross-spectral methodology based on EOF analysis and Hilbert transform, instead of traditional FFT method, to infer nearshore water depth from radar imagery. Besides, sensors in [146] were deployed at too far locations (4 km) from each other, that means there are not enough overlapping footprints over a dense area of interest. Thus, data fusion test was not properly carried out.

Recently, Honegger *et al.* [166], [167] implemented the *cBathy* depth estimate algorithm on X-Band radar data at micro- [166] and macro-tidal [167] nearshore areas. As stated above, *cBathy* was originally designed from video cameras. They added a time lag correction between pixel time series in order to reduce possible error source, since *cBathy* algorithm has been exclusively applied to snapshot video images. Water depth estimates from X-Band radars show mean bias errors and RMSE of 0.26 m and 0.49 m, respectively, by applying the Kalman filter but without considering non-linear effects [166]. Hence, significantly higher errors are achieved at locations shallower than 2 m depth (surf zone). In contrast, bathymetric inversion from video imagery shows mean bias errors and RMSE of 0.23 m and 0.44 m, respectively [166]. In the extended case where tidal currents are considered on the linear dispersion relation [167], the mean bias error is 0.02 m with RMSE of 0.35 m. Therefore, inherent limitations of *cBathy* algorithm remain [166].

A data-model assimilating method, *Beach Wizard* [193], was able to reduce nearshore subtidal bathymetry bias error applying an optimal least-square estimator. Water depth was updated considering wave celerity and time-averaged radar and video images. In-situ measurements were not available. Model-predicted errors increase with periods of low wave heights, mainly in the deeper seaward areas. In surf zone areas, incorrect video image rejection yields false bathymetry update. In contrast, Wilson *et al.* [17] predicted bathymetry by assimilating 5 hours of in-situ and remotely sensed measurements (including IR, radar and video imagery) through the ensemble Kalman filter. Bathymetry is rapidly corrected and a surf zone rip current is observed only using remote sensing data. Shoreline and wave current are obtained from variance and timestack ARGUS images, respectively. Wave celerity and wavenumber is derived from both radar and video data. However, radar data are disregarded in a cross-shore range of 0-250 m from the detected shoreline because pixel resolution is inferior than optical systems, yielding an under-estimated wavenumber in shallow waters.

2.8   Summary

Coastal systems are sensitive environments where a large number of non-linear processes operate at different space-time scales. Since beaches are the first barrier in front of coastal flooding and their economic and social importance is relevant in terms of tourism economy and outdoor recreation, several studies of nearshore zones have been performed to better understand coastal processes. Remotely sensed data are of the particular interest because they can measure wave characteristics in large coastal areas even at high-energetic storm conditions unlike in-situ sensors. This Chapter introduces a variety of definitions and previous studies related to wave properties estimation, shoreline detection and depth inversion using X-Band radars and optical video imagery.

On a general basis, radar-derived wave properties algorithms based on spectral analysis approach considers empirical MTF, signal-to-noise ratio and the three-dimensional discrete Fourier Transform with good agreement between estimated and ground truth wave data. However, they depend on several factors and assumptions which make them only approximate for a single location. Hence, they may need to be calibrated by using external reference in-situ sensors when the algorithms are applied on a different study area [1]. In contrast, texture analysis techniques remote calibration procedure, but they demand considerable computation time and the performance needs to be improved relative to the spectral analysis algorithms. Besides, video monitoring systems usually capture noisy signals from remnant foam and wave breaking in the surf zone that hinder the accurate depth inversion and shoreline detection, even in daylight hours with fair weather conditions.

Although previous studies have suggested a potential fusion of radar and video systems, conditions how and when microwave and optical algorithms can be considered as complementary coastal monitoring data sources are still poorly defined. Besides, depth inversion algorithms strongly depend on traditional FFT procedures and linear wave theory, neglecting shadowing modulation and non-linear behaviour of shallow water waves in nearshore areas.

Chapter 3

Datasets

"To receive everything, one must open one's hands and give."

Taisen Deshimaru (1914 – 1982)

3.1   Introduction

Optical cameras and X-Band marine radars have become the most desirable nearshore sampling tools. However, most of applications use fixed video cameras because X-Band radars have only been adapted for wave data retrieval. Marine radars provide day-night sea state data and large spatio-temporal resolution to measure coastal processes, whereby they are good mapping tools for further coastal investigations. Although several studies show that coastal morphology can be described by video cameras [17], optical systems cannot estimate some wave properties such as significant wave height [2]. Hence, it is reasonable to believe that dissimilarities and advantages by which both sensors (i.e. radars and cameras) interact in coastal environments provide interesting opportunities to merge them through the simple addition of individual devices capabilities. Their complementary spatial and temporal resolutions with non-redundant information could yield a more detailed footprint of the nearshore processes.

The challenge of remote sensing in coastal areas is to develop more advanced algorithms and methods to obtain accurate sea state data, water depth and shoreline estimates which can be incorporated into prediction models in shallow areas. Therefore, this doctoral dissertation mainly discusses two hypotheses: (1) *Accurate sea state parameter estimations could be retrieved from X-Band marine radars through the mitigation of shadowing effects*, (2) *coastal morphodynamics and hydrodynamics estimates could improve by merging data from multiple low-cost sensors*. The research performed along this PhD thesis has been the result of the combination of different techniques aimed to be complementary in order to prove the previous hypotheses. Since coastal dynamics is governed by a set of nonlinear processes, the nearshore study requires not only accurate modelling systems but also continuous measurements of nearshore conditions. In this Section we outline some of the techniques applied and developed in the different Chapters where more details are given.

3.2   Field Sites Description

This research requires four distinct datasets that were acquired during different field campaigns at onshore locations in beaches from the Caribbean Colombian coast and the Western Mediterranean coast. A brief description of each study area and an overview map of the experimental setup is given.

Salgar Beach

Salgar beach is one of the beaches of Puerto Salgar, a township in the town of Puerto Colombia seven miles from Barranquilla, in the Colombian Caribbean region. The wide belt of beaches begins on the province of Sabanilla and ends on the rocky cliff of Salgar Castle, a National Historic Landmark. Salgar is located in the Northwestern coast of the Caribbean Sea, as shown in Figure 3.1. From a morphodynamic point of view, Salgar is an intermediated transverse bar and rip beach (TBR) with high wave energy dissipating along its coastline. It is discontinuous along shore, because of alternation of shallow bars and deeper rip channel. Typically, H_s is below 2 m from the northeast, according to in-situ data from the directional wave buoy located at Bocas de Ceniza, Colombia [194], [195]. As depicted in Figure 3.1, the field site is located at 11°1′5.772″ N, 74°56′29.796″ W, on the terrace floor of the Salgar Castle.

Salgar beach is a shocking case of coastal erosion [10], [196]. Some civil coastal defense structures, such as groynes, have been constructed in Salgar beach for damage mitigation and protection of this vulnerable zone. Regarding the hazard rating, this beach corresponds to a moderately hazardous area, with a hazard rate of 6/10 due to the groynes generate topographic rips. It is one of the highest rates in the Colombian Caribbean coast. Besides, Salgar beach has a C public risk level, mainly because human overuse and touristic explotation [194]. Hence, sea state needs to be continuously monitored to manage timely preventive actions against these issues.
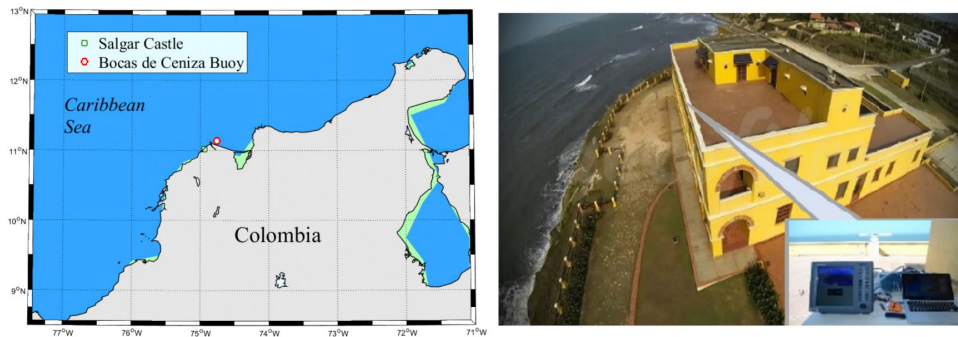
Figure 3.1: Salgar beach location and equipment setup in Salgar Castle (20 m above the mean sea level (MSL): LAT = 11°1′5.772″ N; LON= 74°56′29.796″ W).

Castelldefells

Castelldefels is an open, tideless and dissipative beach located approximately 20 km south-west of Barcelona (Spain), facing southward at the Western Mediterranean Sea, as depicted in Figure 3.2. Castelldefels beach is about 4.5 km long and it belongs to the strech of the Llobregat river delta. The study site is located at 41°15′54.440″ N, 1°59′50.628″ E, scanning 5 km^2 with the

radar signal. This beach is mainly comprised by sand with a uniform sediment size of 0.3 mm. Generally, waves come from both East-Southeast and the Southwest but the highest waves come from the East (mainly between September and March) because the strongest influence of winds that are presented from this direction [125], [135].
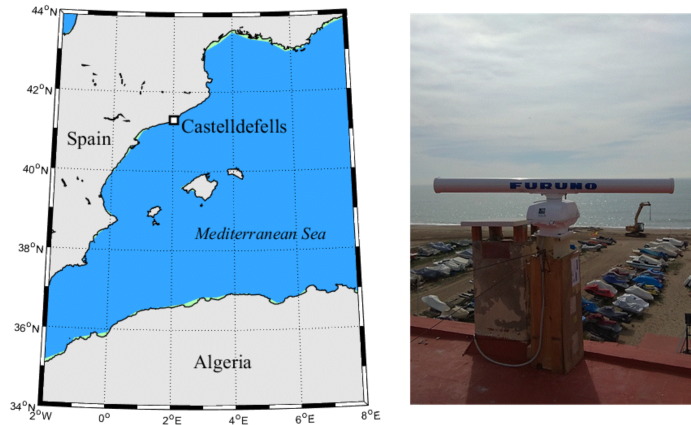
Figure 3.2: Castelldefels beach location and equipment setup in *Marítimo* restaurant (13 m above the mean sea level (MSL): LAT = 41°15′54.440″ N; LON= 1°59′50.628″ E).

Cala Millor

Cala Millor is a semi-stretched and sandy beach located in the North-eastern coast of Majorca, Balearic Islands, Spain, in the Western Mediterranean Sea. The beach area is about 14 km^2 with 1.7 km long and a variable water depth ranging from 6 to 35 m. The seabed is colonized by the endemic *Posidonia oceanica* meadow, which increases bottom roughness modifying the sediment transport [197]. Cala Millor is a microtidal (i.e. with a negligible tidal regime below 0.25 m) and an intermediate beach with a dynamic configuration of transverse and crescentic bars. Due to its semi-enclosed configuration, waves typically come from the NE to the ESE with a significant wave height usually bellow 0.9 m. Bathymetric variations are often more intense than sandbar movement and the occurrence of storm is during 2% of the days of a year with H_s over 1 m [198].

Figure 3.3: Cala Millor beach location and equipment setup in the rooftop of the *SENTIDO Castell de Mar* hotel (46.7 m above the mean sea level (MSL): LAT = 39°35′46.849″ N; LON= 3°22′59.164″ E).

San Andres Island

San Andres Island is a coastal reef environment in the Colombian Caribbean Sea that belongs to Archipelago of San Andres, Old Providence and Sta. Catalina. This territory is at the lower Nicaraguan rise in the Western Caribbean Sea. San Andres Island is located at 750 km from the north-western coast of Colombia with an area of 25 km^2 and a population of more than 60.000 inhabitants. Therefore, it is probably the largest and the most densely populated island in this province, where climate change and human impact over coral reef health must be analyzed [199], [200]. Figure 3.4 shows the study site location at the northeastern coast of San Andres Island, specifically at down-town area. The study site is a tropical area with a plenty of borderline reefs, the most common coral reef type in Colombia, which forms a solid and continuous structure with a lagoon of variable depth.

From a hydrodynamic point of view, wind directions are primarily from the ENE with mean monthly variations between 4 m/s (May, September-October) and 7 m/s (December-January, July). Significant wave height is below 2 m. The predominant surface wave current is from E to W in the Caribbean Sea, which forms a large counter-clockwise eddy in the south-western Caribbean coast. San Andres Island is permanent exposed to long-periodic oceanic swells generated by trade winds over nearly 2000 km wave fetch, whose released energy influences the structure of benthic communities on coral reefs, beach morphology and sediment transport processes.
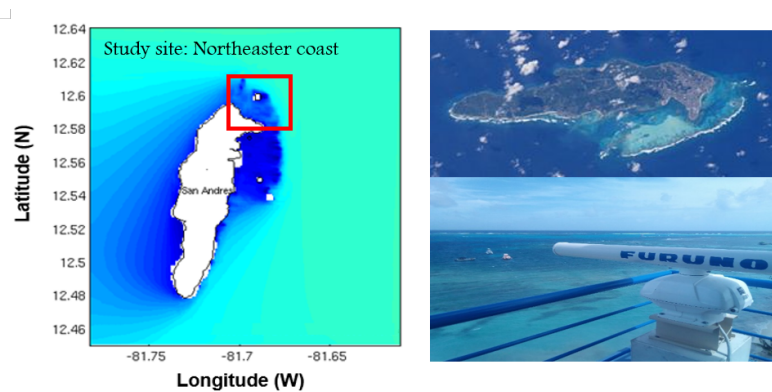
Figure 3.4: Study site at the northeastern coast of San Andres Island. Equipment setup at Calypso restaurant (34 m above the mean sea level MSL: LAT = 12°35′6.2″ N; LON= 81°41′35.8″ W).

3.3   Observations

Field data is acquired by X-Band marine radars, in-situ sensors and video monitoring systems. The in-situ data is necessary to validate the performance of both radar- and video-derived estimates and to establish a clear relationship with radar and video accuracy. In-situ measurements must align spatially and temporally with remote sensor datasets for comparison. Therefore, in-situ data is often interpolated to be spatially similar to radar grid. Figure 3.5 depicts a schematic representation of the relationship between the remotely sensed data and in-situ datasets with the analytical approaches and final products used throughout this doctoral dissertation.
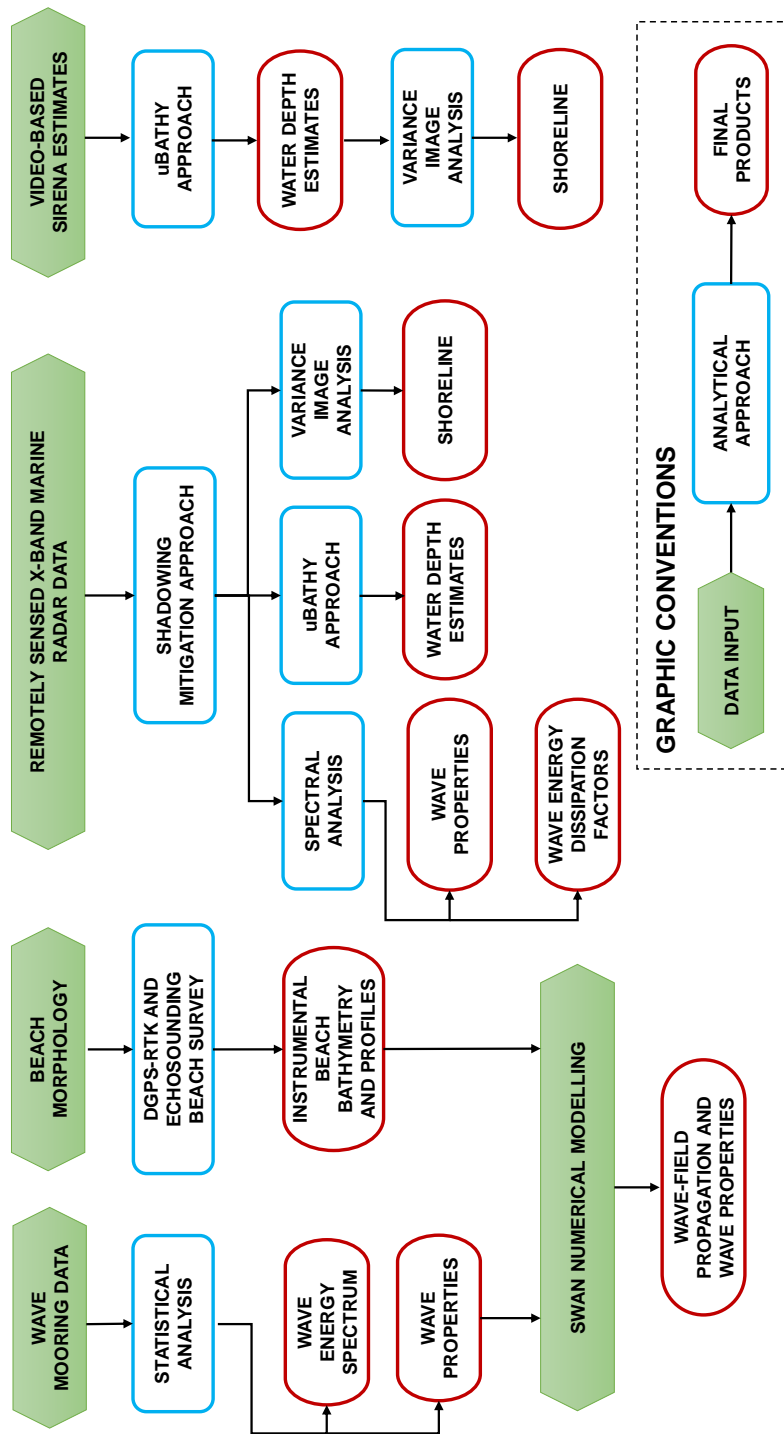
Figure 3.5: Schematic representation of datasets and approaches used in this study

3.3.1   X-Band Radar

In this study, a commercial X-Band marine radar FURUNO 8252 was used for scanning the coastal area. In particular, the pulse nautical radar was equipped with a 6-foot long X-Band antenna (9.41 GHz) rotating in the horizontal plane (HH polarization) at 48 rpm which results in a temporal resolution of 1.25 s. The output peak power of the system is 25 kW and the radar field of view was 180° for the measurement campaigns, thereby the coverage area corresponds to 5 km^2. The radar system transmits short pulses whose length are 80 ns with a horizontal beam width of 1.35°.

The nominal radar range resolution given by $\Delta r_{RADAR} = c\tau/2$, where τ is the length of the electromagnetic transmitted pulses and c is the speed of light. Thus, a $\tau = 80$ ns pulse length corresponds to a $\Delta r_{RADAR} = 12$ m. However, the sample frequency of the acquisition system could be selected in order to obtain a desired range resolution for the digitized images [51].

The range resolution designed for the system can be obtained as $\Delta r = \frac{c}{2f_{ADC}}$, giving $\Delta r = 6$ m. The azimuthal resolution is 0.1° using a sample frequency $f_{ADC} = 25$ MHz for the Analog-to-Digital converter (ADC) [51]. Table 3.1 summarizes some system configuration parameters of the marine radar [201].

TABLE 3.1: Parameters of the radar acquisition system FURUNO FR-8252

Parameter	Value
Frequency	9.41 GHz
Peak power	25 kW
Antenna rotation period ($\triangle t$)	1.25 s
Spatial resolution ($\triangle r$)	6 m
Radar coverage	2500 m
Pulse length	80 ns
Antenna Polarization	HH
Pulse repetition frequency (PRF)	2100 Hz
Horizontal beam width	1.35°
Vertical beam width	22°
Azimuth resolution	0.1°
Antenna speed rotation	48 rpm

Figure 3.6 shows the block diagram of the X-Band radar system developed by the Telecommunication and Signals Group (GT&S) from Universidad del Norte, Colombia. The system employs a FPGA Cyclone I core that incorporates a clock signal of 50 MHz, a 10-bits ADC acquisition card that allows mapping the digitized echo intensity from 0 to 1023, and a LAN controller to send the sea clutter data to a computer via Ethernet port connection [51]. Echo signals received from the sea surface are visualized in the Radar Display Unit. Then, the acquisition system discretizes the sea clutter data using *Trigger*, *Heading* and *Bearing* signals for synchronization. Thereby, time sequence of raw radar images are acquired and transmitted [51]. The radar system measures sea surface through off-line spectral analysis. Sea state parameters as θ_p, T_p, H_s and temporal-spatial images of the sea surface elevation can be obtained.
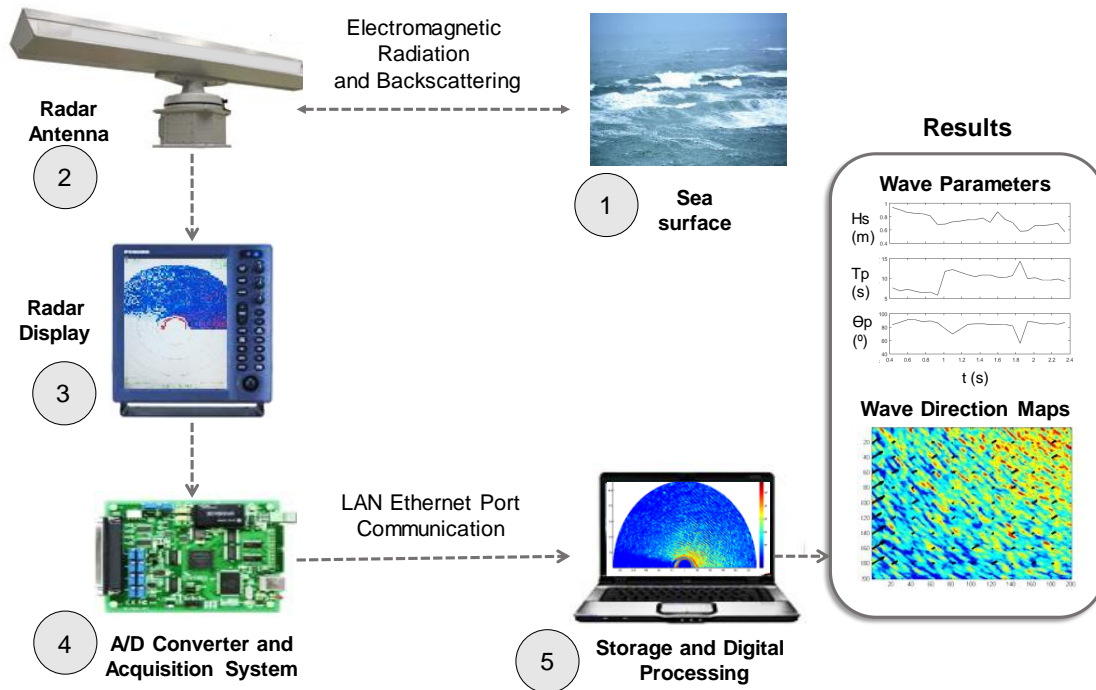
Figure 3.6: Block diagram of the radar acquisition system and settings.

3.3.2 Video Monitoring System

SIRENA video monitoring system [145] operates during the field experiments to capture nearshore images at Castelldefels and Cala Millor beaches. Results are discussed in Chapter 6. The stereo-video system is installed in a 32 m high observation tower at Castelldefels beach, whereas it is deployed at 46.7 m above MSL in Cala Millor beach. Both video-based systems consist of 5 full-colour cameras SONY XCD-SX90CR IEEE1394b that covers a full field of view of the beaches (i.e. 180 degrees overview of the shoreline). Optical cameras are connected to a central *SIRENA Station* with Linux/Ubuntu operating system that stores, digitalizes and transfers the video data to the *SIRENA Network System* that makes images available to the user. This storage system is also a GNU/Linux with CentOS connected to the Internet [145].

SIRENA open source code provides one snapshot image, one *timex* image and one variance image every daylight hour with a resolution of 1298 × 960 pixels. *Timex* and variance images are statistical products that consider the first 10 minutes of each hour (i.e. the mean and the standard deviation of 600 snapshot images at 1 Hz, respectively) to quantify hydrodynamical and morphological coastal data. For instance, shoreline and submerged sandbar detection through the identification of stripes of foam in the video imagery contrast is a useful application for coastal management.

Afterwards, video images are rectified and transformed from image-to-ground local coordinates through standard photogrammetric equations and assuming an invariant vertical coordinate at tidal level. Hence, detailed information about camera position, orientation and focal length are needed. Visible and georeferenced distance temporary ground control points (GCPs) allow

the definition of tilt, pitch and roll to accurately obtain the true camera orientation, which is crucial to identify image coordinates. However, camera orientation can rapidly shift due to strong winds or thermal expansion. Therefore, a periodical calibration procedure is required. Radial lens distortion is corrected using the focal length which is typically measured in the laboratory, but it is only suitable to a particular image geometry.

Finally, ULISES open source code merges the stereo-video imagery from the five cameras into a planview of the shoreline with a size of 2001×601 pixels (i.e. 1000×300 m with a pixel resolution of 0.5 m) [148]. The origin of the coordinate system is the location of the SIRENA video monitoring system. Figures 3.7a and 3.7b show a panoramic photography of the video-based coastal observation system at Castelldefels and Cala Millor beaches, respectively.

(a)   (b)

Figure 3.7: Stereo-video coastal observation system at **(a)** Castelldefels beach and **(b)** Cala Millor beach.

3.3.3 *In-situ* Data

Wave Data

Wave data from the ADV gauges where obtained considering the pressure field associated with a progressive wave and the unsteady Bernoulli equation. Basically, the ADV gauges sense the pressure fluctuations and then we calculate the associated water surface elevation by least-square fitting pressure data to a Fourier series and applying the Equation 3.1 and 3.2 [19]. These expressions consider that pressure measured by the gauge is comprised by a hydrostatic term, which does not rely on the presence of waves, and an oscillating dynamic pressure as a result of the presence of wave motion,

$$\eta = \frac{p_D}{\rho g K_p(-h)} \tag{3.1}$$

and

$$K_p(-h) = \frac{1}{\cosh(kh)} \tag{3.2}$$

where p_D is the dynamic pressure which is isolated by subtracting the mean hydrodynamic pressure, ρ is the ocean water density, g is the acceleration due to gravity and $K_p(-h)$ the pressure response factor, knowing the water depth h of the installed gauge and the angular frequency ω of the reconstructed waves, the linear dispersion relation, $\omega^2 = gk \tanh(kh)$, could be used for determining wavenumber values (k) and finally estimating the free sea surface displacement η, as shown in Equation 2.2 [19].

On the other hand, the X-Band radar scanned the sea surface every 5 minutes during Salgar beach campaign but the deployed ADCP provides currents and wave data only 20 minutes every hour. Therefore, the outputs of the X-Band radar are averaged every hour and the resulting sea state parameters are compared with the in-situ data in order to minimize the error produced by no-matching output time between X-Band radar dataset and the in-situ measurements.

For the MUSAFELS experiment at Castelldefels beach, the three bottom-mounted pressure gauges (ADV) operated during 210 seconds every 30 minutes, the AWAC sensor worked twice times each hour collecting sea state data during 20 minutes on each run and the X-Band radar worked continuously. Therefore, the time exposure radar images were truncated until the measurement period limited by the in-situ sensors. The same procedure is used for field datasets at Cala Millor, Salgar and San Andres Island beaches.

Bathymetric Surveys

Topographic profiles and bathymetric surveys were carried out to describe the nearshore morphological variations in every study site. A differential GPS-RTK with submetrical resolution is used for the description of shallow water depth characteristics in aerial and submerged beach (i.e. from shoreline and up to 1 m depth). Deeper depths at submerged beach is measured in cross-shore transects by using a Biosonics DE-4000 multibeam echo-sounder with a cell size of 1×1 m, which is mounted on a ship yielding a dense mapping of the nearshore area from 0.5 m and up to 30 m depth.

Bathymetric surveys were performed during calm sea state conditions to reduce errors in measured water depth due to wave-induced pitch and roll of the ship. In-situ measured water depth data is often converted to the radar grid by linear interpolation and smoothing techniques. Radar range, i.e. 5 squared kilometres, defines the spatial domain of the bathymetric study in this doctoral dissertation. Particular details are presented on each Chapter, when more information is required.

3.4   Numerical models

The *Simulating WAves Nearshore* (SWAN) model solves the equation of action balance for the propagation of the wave spectrum, allowing realistic estimations of wave parameters in oceanic and coastal zones [202]. To assess the performance of SWAN in the area, the model is first validated in a non-stationary simulation using the Japanese 55-year wind Reanalysis, JRA-55 [203] using a coarse grid of 229×101 points spaced each 12 km in longitude and latitude, that covers the Caribbean basin.

Sea states from a model grid point at the same position of the NOAA buoy # 42058, were used to validate the simulated waves. This buoy is in the central Caribbean at 14.755°N, 74.56°W. Wave growth by wind was set as exponential following the formulation of Komen *et al.* [204] and the deep water non-linear interaction by using the Webb-Resio-Tracy method, as stated in [205]. Besides, wave breaking as well as energy dissipation by whitecapping and bottom friction were took into account for the simulation [205]. The time step was set as 30 minutes and results stored for each sea state condition, i.e. every 3 hours [205].

The mean bias and root mean square error (RMSE) between the buoy and the SWAN model grid point time series are about zero whereas the Willmot and the correlation coefficient are 0.9 and 0.83 respectively, showing a good fit between modelled and observed data, as shown in Figure 3.8. This relationship is statistically significant at a confidence level of 95% according to a two-tailed t-Student distribution with p-value lower than 10^{-5} [205].

Subsequently, validated SWAN model was implemented for the San Andres area in stationary mode. In this case, the SWAN domain had a resolution of 50 x 50 m^2 (i.e. 480×419 grid points) with bottom left UTM coordinates 1375010 N, 413380 E at zone 18 N. Bathymetry was obtained from the nautical charts COL 414, COL 201, COL 202 from the Colombian Hydrographic Institute, with scale ranges of between 1:25000 and 1:100000.
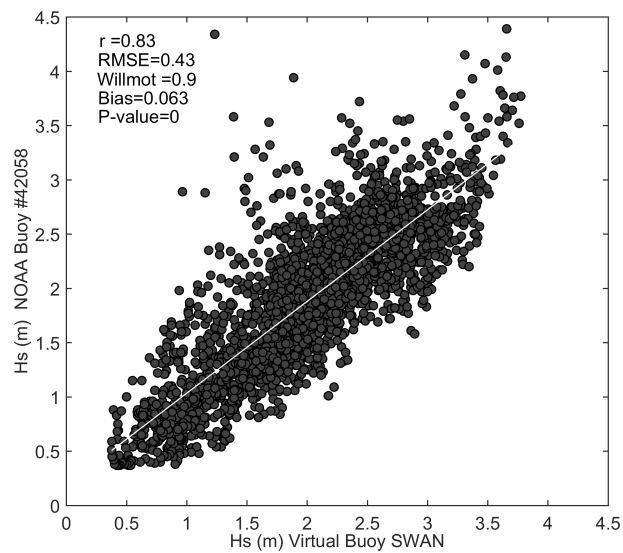
Figure 3.8: Dispersion diagram where the WWIII data propagated with SWAN model are correlated with the wave data of the buoy # 42058 available in the National Data Buoy Center of the NOAA.

Chapter 4

Estimation of Sea State Parameters

"Do not go where the path may lead, go instead where there is no path and leave a trail."

Ralph Waldo Emerson (1803 − 1882)

4.1 Introduction

This Chapter presents a novel procedure to estimate wave parameters in coastal areas considering extreme grazing incidence angles, i.e. shadowing, without external calibration neither the definition of an empirical MTF. The method employs filtering and interpolation approaches to mitigate shadowing effects so as to enhance sea clutter raw radar data (beam by beam). Shadowing influences on sea clutter intensities along range (i.e. the distance from the detected target to the transmitter antenna) are considered, which have not been studied yet in detail [206].

The proposed methodology uses datasets acquired from a FURUNO FR-8252 X-Band marine pulse radar, whose acquisition system was developed by the Telecommunication and Signals Group (GT&S) from Universidad del Norte, Colombia [40]. The radar system was deployed at onshore locations during different field campaigns which took place at beaches in the Caribbean Colombian coast (Salgar, Colombia, on February 2014 and June 2015) and the Western Mediterranean coast (Castelldefels, Spain, on March 2018). Five different pre-processing approaches were tested in order to determine the most appropriate technique to estimate coastal sea state parameters with high resolution and accuracy mitigating shadowing. Results derived from each proposed technique were compared with in-situ data obtained by a Nortek AWAC (*Acoustic Wave and Current*) sensor. In summary, the main contributions of this methodology are:

- To the best of our knowledge, this is the first method that identifies intensities affected by shadowing modulation along range and corrects them using filtering and interpolation approaches to fill in the shaded areas.

- The system was designed using data acquired by coastal radar stations in nearshore applications considering extreme grazing incidence angles from electromagnetic signal over sea surface without calibration.

- Unlike previous studies that use offshore empirical MTF to correct the estimation of coastal wave parameters, the proposed methodology considers intensity data of each beam along range taking advantage of high spatial resolution of radar systems (6 m, in this case).

- Therefore, the procedure is able to reconstruct the wave frequency spectrum at each pixel with a spatial resolution of 6 m covering an area of more than 5 square kilometres. As a result, the estimation of coastal wave parameters derived from X-Band radar systems can be compared with hundreds of in-situ sensors monitoring the total coverage area of the radar system at the same time. However, spatial resolution improvements involve restrictions in the temporal sampling domain [1]. Although X-Band marine radars map hundreds of meters covering large areas during short timescales, they do not get the accuracies of in-situ measurements and they require as well a high computational cost.

The chapter is outlined as follow. Section 4.2 gives a brief description of all datasets used for the analysis. Section 4.3 is devoted at presenting an empirical characterization of shadowing effects in coastal areas defining the methodology to adjust the threshold value for the interpolation. The methodology to estimate wave parameters, such as peak period T_p, peak wave direction θ_p, peak wavenumber k_p and significant wave height H_s, is presented in Section 4.4. Section 4.5 deals with the comparison of the sea state parameters estimation and the measurement provided by an ADCP Nortek AWAC, which was installed at a depth of 8 m in the area. A discussion is presented in Section 4.6. Finally, Section 4.7 concludes the chapter.

4.2   Field Data

The present study considers three datasets acquired at two different beaches: Salgar beach in Colombia and Castelldefels beach in Spain. Table 4.1 summarizes the dates and the number of sea states (*n*) considered. It also includes the code used hereinafter to refer each set. The sea state conditions detailed in Table 4.1 are the average values of T_p and H_s derived from AWAC sensors, as mentioned in Chapter 3.

TABLE 4.1: Summary of the datasets considered for the study

Code: description	Date (yyyy/mm/dd)	*n*
S1: Salgar, 10 m AMSL	2014/02/28	4
S2: Salgar, 20 m AMSL	2014/02/28	4
S3: Salgar, 20 m AMSL ($T_p < 9$ s, $H_s < 2$ m)	2015/06/19	9
C1: Castelldefels, 13 m AMSL ($T_p < 6$ s, $H_s < 0.45$ m)	2018/03/14	3
C2: Castelldefels, 13 m AMSL ($T_p < 8$ s, $H_s < 1.6$ m)	2018/03/15	15
C3: Castelldefels, 13 m AMSL ($T_p < 7$ s, $H_s < 1$ m)	2018/03/16	11
C4: Castelldefels, 13 m AMSL ($T_p < 4.5$ s, $H_s < 0.9$ m)	2018/03/17	6
C5: Castelldefels, 13 m AMSL ($T_p < 10$ s, $H_s < 1.3$ m)	2018/03/18	11
C6: Castelldefels, 13 m AMSL ($T_p < 5$ s, $H_s < 1$ m)	2018/03/19	11

In this study, S1 and S2 datasets (Table 4.1) are used for the characterization of shadowing modulation throughout the distance away from radar antenna location. S3 dataset runs from Salgar field campaing on June 2015 was used for illustrating the technique and explaining the initial results. The technique was then further tested using data collected as a part of the MUSAFELS experiment, conducted during March 14th-19th 2018, at Castelldefels beach (C1-C6 datasets) over different wind and wave conditions.

This study requires wave data from X-Band radar images and a set of in-situ measurements for evaluating the performance of the radar estimates. S1 and S2 datasets were derived from two radar antennas installed on the first and terrace floor at Salgar Castle at 10 m and 20 m above the mean sea level (MSL), respectively. For S3 dataset, a single X-Band marine radar was deployed on the same location than S2. Radar antenna was oriented 27° NW. An ADCP sensor was installed in 8 m water depth to compare its wave data against the X-Band radar estimates.

For MUSAFELS campaing (C1-C6 datasets), a X-Band radar was deployed on the roof of the "*Marítimo*" restaurant at 13 m above MSL with a field view of 180°. The antenna was oriented 193° SW. Wave data were obtained from an array of three wave gauges (ADV 1, 2 and 3) located at 3.8 m, 5 m and 7 m water depth, respectively. Besides, an ADCP sensor was deployed at a depth of 21 m inside the coverage area of the radar antenna. Figures 4.1a and 4.1b give a general layout of the marine radar and in-situ instruments deployment in Salgar and Castelldefels beaches, respectively.

4.3 Shadowing Characterization

In order to characterize the sea clutter intensities affected by shadowing modulation, each radar antenna height of the S1 and S2 datasets corresponds to a stochastic process that has its own realizations along range. The sample space (Ω) of these two stochastic processes is made from 200 realizations corresponding to the intensities of the highest variance beam along range from the sea clutter images. A pre-filtering is first applied in order to identify the highest variance beam in the sea clutter image, eliminating echo signals received from buildings, vessels, land and other objects. If it is not done, the highest variance beam may correspond to *non-clutter* signals distorting the analysis [40], [41].

The variation of shadowing along range has a key role to estimate wave parameters, such as H_s [207]. Considering that geometric shadowing occurs when any echo signal is received from the smallest and obstructed waves forming hidden and noisy areas in the sea clutter images [52], [106], [110], [208], two methods for counting the amount of intensities affected by shadowing are proposed. As a first step, the mean RCS of each antenna height is fitted to a third-order polynomial function since the radar equation explains that the power decay along range is cubic [52]. Figure 4.2a and 4.2b present the polynomial function fitted to the mean RCS at 10 and 20 m above MSL, respectively. The proposed methods for shadowing characterization are as follow:

1. **Method 1** considers that the intensities affected by shadowing are those below the polynomial approximation at each range. The red line in Figure 4.2 corresponds to the adjusted threshold considered in this method, which changes for each distance from the radar antenna. Likewise, the black dots correspond to the mean RCS.

2. **Method 2** takes into account that shadowing can be identified counting all the echo intensities that are below the smallest value of the polynomial approximation, which is usually reached at 2 km away from the radar antenna, as shown in Figure 4.2. After that distance, there are no significant difference between the averaged intensities. Unlike the previous

◇ X-Band Radar (LAT=11°1′ 5.772″ N, LON=74° 56′ 29.796″ W)
● AWAC sensor (LAT=11°1′ 52″ N,   LON=74° 56′ 26.902″ W)

(a)

◇ X-Band Radar (LAT=41°15′ 54.440″ N, LON=1° 59′ 50.628″ E)
● AWAC sensor (LAT=41°15′ 0.3″ N,   LON=2° 0′ 0.36″ E)
○ ADV 1 (LAT=41°15′43.68″ N,   LON= 1° 59′ 23.82″ E)
■ ADV 2 (LAT=41°15′ 37.02″ N,   LON=1° 59′ 23.7″ E)
✦ ADV 3 (LAT=41°15′ 33.36″ N,   LON=1° 59′ 24.24″ E)

(b)
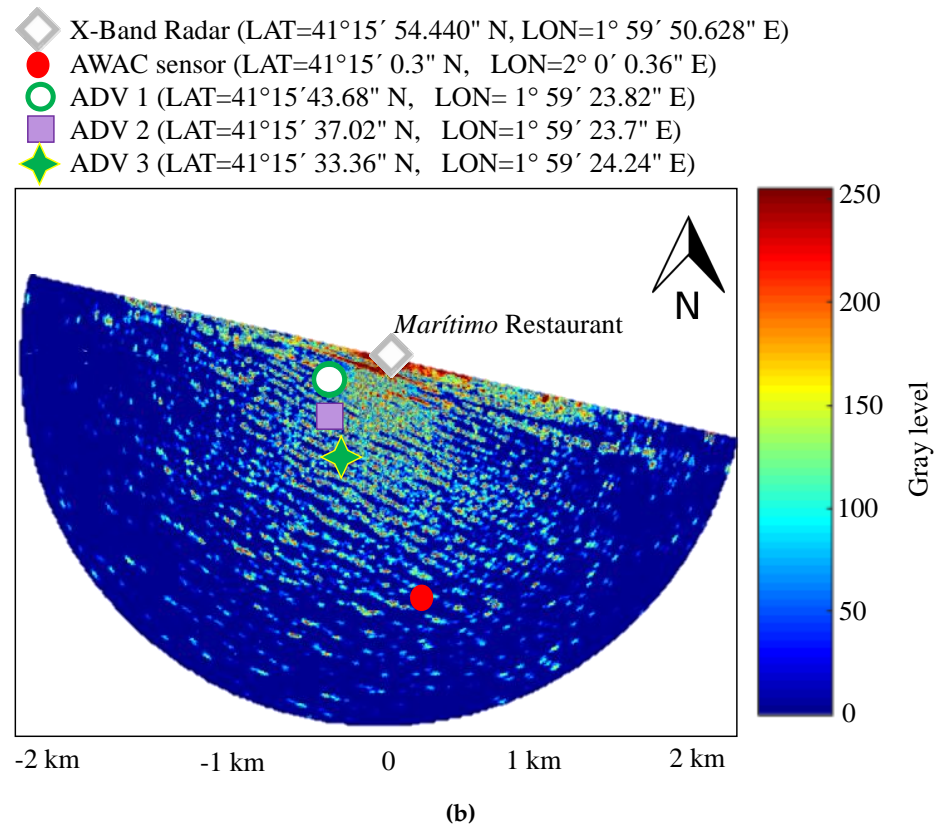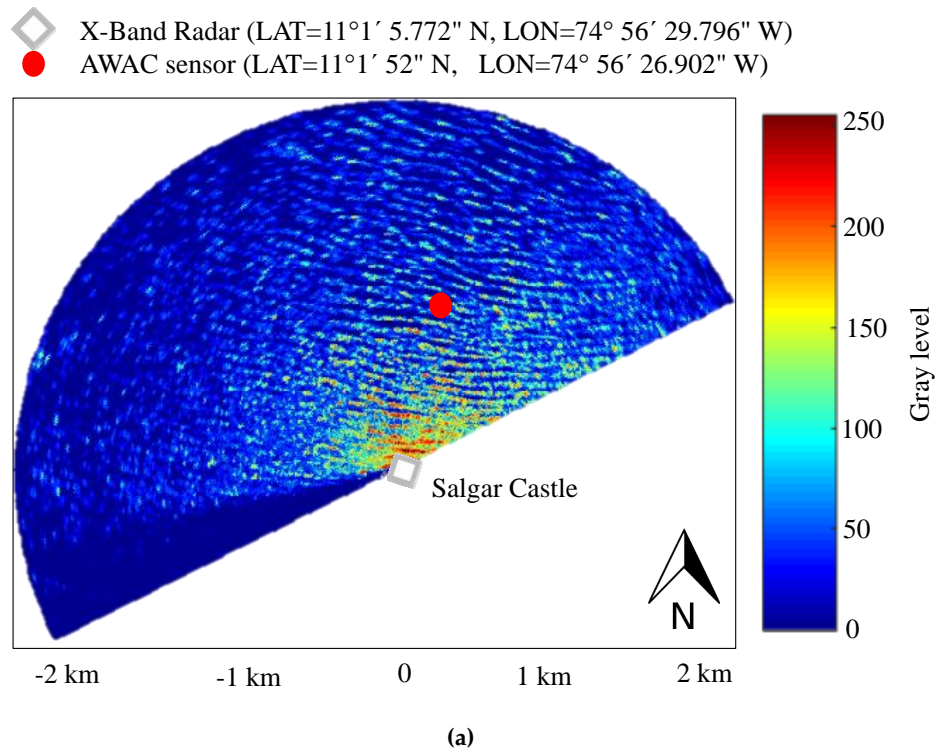
Figure 4.1: General layout of the marine radar and the in-situ sensors in the **(a)** Salgar campaing (S1-S3 datasets), **(b)** MUSAFELS campaing (C1-C6 datasets).
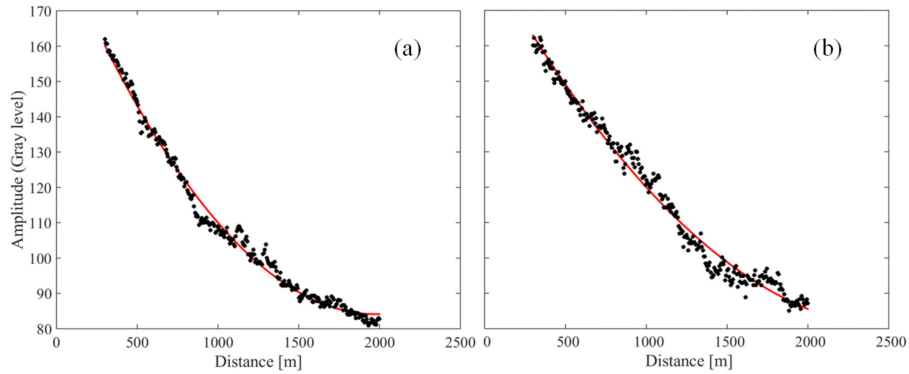
Figure 4.2: Polynomial approximation from the mean RCS (*Radar Cross-Section*) collected by the radar antennas located at **(a)** 10 m and **(b)** 20 m above MSL. Red line represents the best third-order polynomial function fitted to the average RCS (black dots) of each antenna height.

method, the threshold value does not change along range but it may vary for different sea state conditions.

The proposed methods consider principles of geometric shadowing along the surrounding azimuth area of the highest variance beam. However, they can be applied to partial shadowing processes because echo signal from shadowed areas are always weaker than the backscatter signal from illuminated facets [106]. This assumption makes sense since radar signal-to-noise ratio (SNR) is directly derived from wave intensity and variance [40], [41]. Due to azimuth direction of the highest variance beam matches properly with the wave direction, it provides the most accurate description of the current coastal wave conditions and allows searching an appropriate threshold to explain shadowing. Besides, this research is focused on range dependence instead of azimuth dependence since waves approach perpendicular toward shoreline in coastal areas due to bottom refraction (unlike offshore stations) and the azimuth dependence could be neglected [52].

Basic statistical measures are computed for the two stochastic processes of interest. Figure 4.3 depicts the mean, median, mode, standard deviation, maximum and minimum values of the echo intensities along range in gray levels (0-255). According to Figure 4.3, a more stable variance is observed from the intensities captured at 20 m height (black dots) than the echo signals obtained at 10 m above MSL (red dots). Variance peaks arise due to the radar antenna delay and the original operation of a pulse X-Band radar [91], [209].

Figure 4.3g depicts the kurtosis (κ) behaviour using the mean RCS from 200 intensity points at each distance. Since kurtosis is a measure of how outlier-prone a distribution is, we found the mean kurtosis value ($\bar{\kappa}$) to characterize the entire dataset along range. As it can be seen, majority of points are concentrated around $\kappa \approx 3$ for both heights. Indeed $\bar{\kappa}$ is 2.97 ± 0.38 and 3.04 ± 0.40 for dataset collected at 10 m and 20 m above MSL, respectively. Hence, data behave as a Gaussian distribution at both heights. Besides, 11.8% and 15.4% of total kurtosis data (416 distances) are higher than $3 \pm \sigma_{\bar{\kappa}}$ at 10 m and 20 m above MSL, respectively. Hence, it can be concluded that intensity data at both heights are normally distributed and they can be described as a mesokurtic distribution with a great concentration around the mean values. It is worth to

note that the maximum κ is obtained in the most remote distance, mainly more than 2 km away from the radar antenna taking into account dataset at 10 m height. Higher κ values are presented for nearshore distances (less than 300 m from antenna). Considering Figure 4.3, these irregular areas have been eliminated from the analysis to avoid including greater variability in the process.
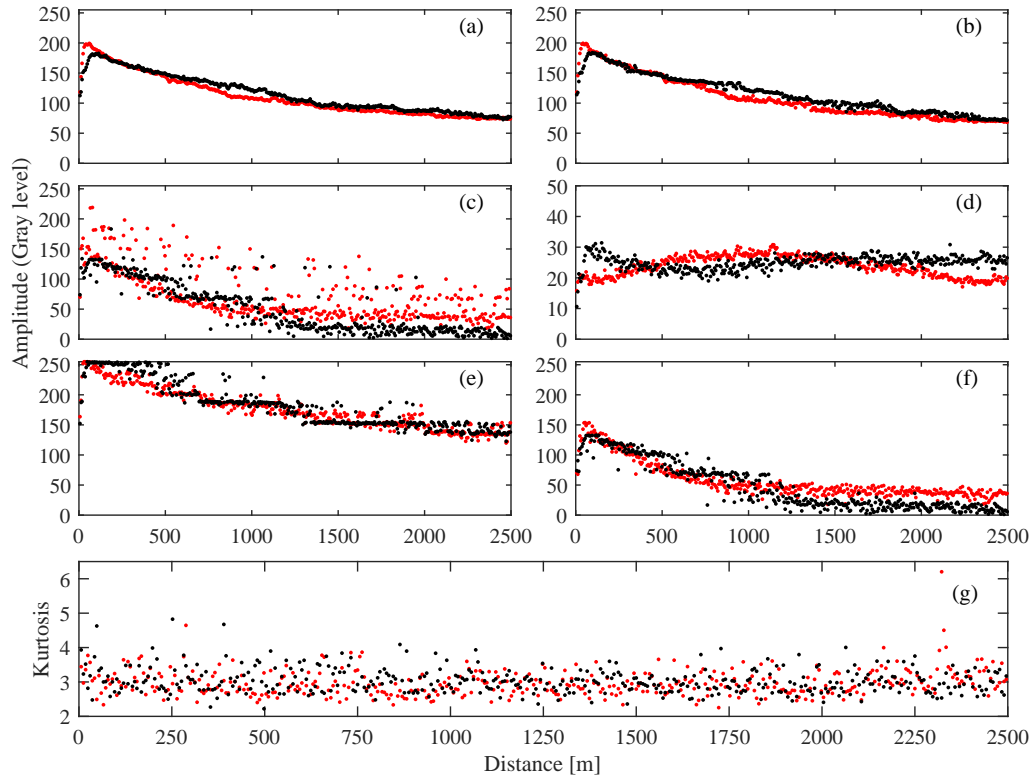
Figure 4.3: Descriptive statistical measures of the stochastic processes with respect to the range: **(a)** mean, **(b)** median, **(c)** mode, **(d)** standard deviation, **(e)** maximum and **(f)** minimum of the echo intensities along range in gray levels (0-255), **(g)** kurtosis coefficient (i.e. the fourth standardized moment, κ) along range considering mean amplitude values. Red and black dots represent the measured radar data at 10 m and 20 m above MSL, respectively. Each distance considers 200 intensity points at both heights.

Figures 4.4a and 4.4b depict the scatter plots from the probability of shadowing along range considering the method 1 and 2, respectively. According to Figure 4.4b, the number of intensities affected by shadowing increases when the distance from radar antenna also increases, being affected up to 60% of the total intensities in the most remote areas. It is in agreement with the hypothesis proposed in [207] for synthetic radar images. However, it does not occur for method 1 considering the irregular behaviour along range depicted in Figure 4.4a.

Table 4.2 shows percentages of change from the total number of intensities affected by shadowing at 10 and 20 m above MSL for method 1 and 2. These data are a measure of the average change from the total shadowing effect. Considering method 2, the percentage of change between radar antenna height at 10 and 20 m exceeds 5%, unlike results from method 1 which are below 5%. In general, this result allows inferring that if the radar antenna height decreases, the shadowing effects increase, as expected. However, an *Analysis of Variance* (ANOVA) test is carried out to validate that method 2 is the most appropriate to explain shadowing.
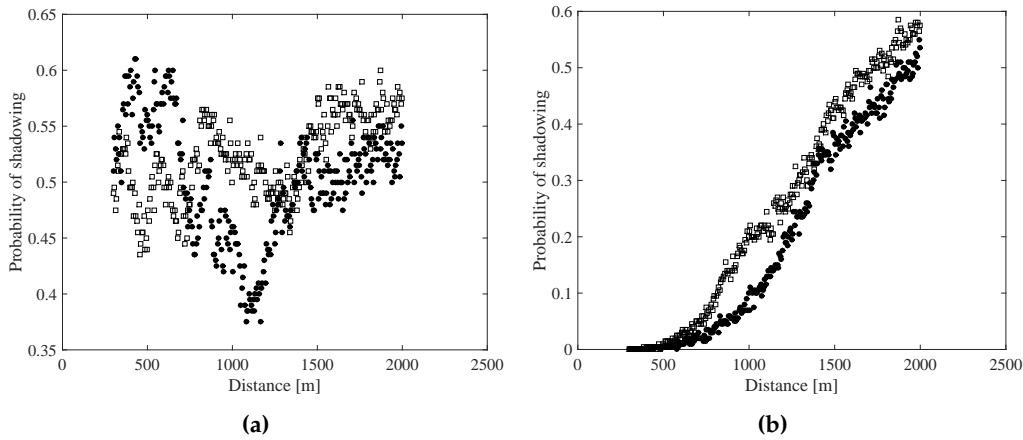
Figure 4.4: Scatter plots of the probability of shadowing along range considering **(a)** method 1 and **(b)** method 2. Square markers and black dots represent the percentage of intensities affected by shadowing at 10 m and 20 m above MSL, respectively. Each distance considers 200 intensity points at both heights.

TABLE 4.2: Total number of intensities affected by shadowing along range and change percentages.

Method	Antenna height	Total intensities	Percentage change
1	10 m	29691	4.31%
	20 m	28463	
2	10 m	14655	27.04%
	20 m	11536	

Table 4.3 summarizes the ANOVA results for method 2 using the decomposition of squares sum [210]. The radar antenna height considers two levels (10 m and 20 m above MSL) with 200 repetitions per range. The entire process considers 284 ranges from 300 m to 2000 m with a spatial resolution of 6 m, resulting in 568 surveyed data. The critical F-value of the Fisher test is lower than the observed F-value. Thereby, it indicates with a confidence level of 95% that the radar antenna height is a significant factor for explaining shadowing modulation effects in sea clutter images. Similarly, due to P-value (0.0006) is lower than $\alpha = 0.05$, there is a statistically significant difference between the means of the radar antenna heights considered.

To validate the ANOVA results, the assessment of normality, homoscedasticity and independence of residuals assumptions is performed [210]. Figure 4.5a illustrates the normal probability plot of the residuals obtained from the ANOVA test. Residuals comply with the normality assumption. Figure 4.5b depicts a scatter plot of the probability of shadowing against the radar antenna height above MSL. It can be seen that both heights present a similar variance, indicating that ANOVA residual comply with the homoscedasticity assumption. Besides, the homoscedasticity assumption is examined running a Bartlett test. The P-value is 0.227, which is greater than $\alpha = 0.05$. Thereby, it can be concluded with a confidence level of 95% that there is no statistically difference between the variances by height. Considering this behaviour, it is not possible to reject the homoscedasticity assumption. In addition, the confidence interval of Lag 1 (i.e. the first delay of the autocorrelation function) is [-0.065, 0.082] that contains zero value. This fact validates analytically the independence of residuals.

Figure 4.5c shows 24 estimated autocorrelations coefficients from the ANOVA residuals and the confidence interval of 95% around zero. Since all the probability limits contain the estimated coefficient, the autocorrelation coefficients do not have a statistically significant correlation, implying that the time series are completely random.

(a)   **(b)**

(c)
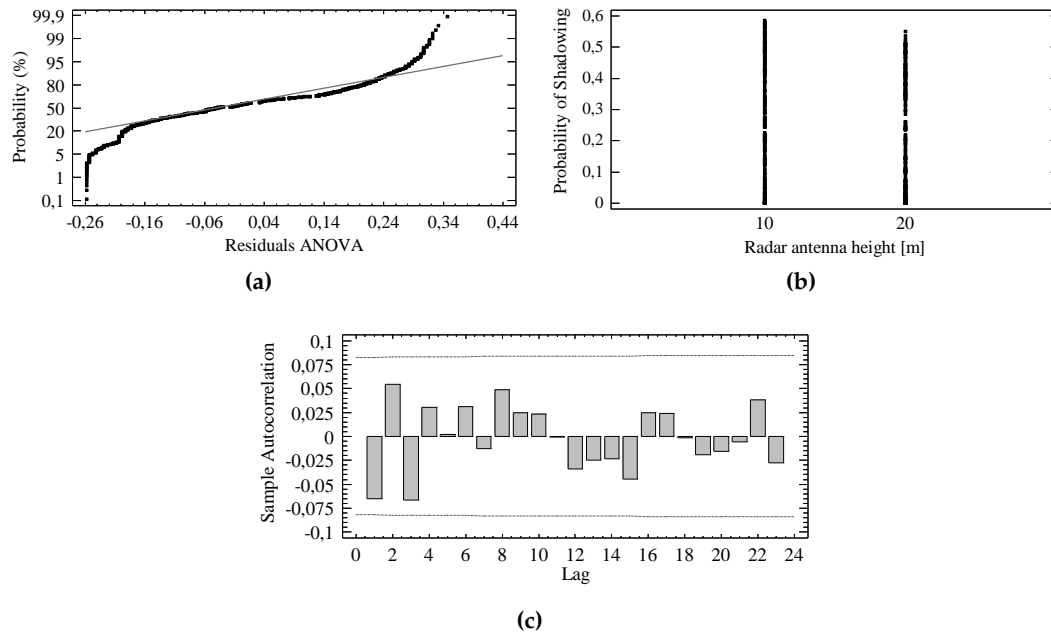
Figure 4.5: Validation of the ANOVA assumptions: **(a)** Normal probability plot to validate the normality of residuals. **(b)** Scatter plot of radar antenna heights and the probability of shadowing to evaluate the homoscedasticity. **(c)** Estimated autocorrelations for ANOVA residuals to examine the independence assumption. Dashed lines depict the confidence interval limits of 95% from the first 24 autocorrelation coefficients, which values are shown as gray bars.

TABLE 4.3: Simple ANOVA results from data of the radar antenna heights (10 m and 20 m above MSL) considering method 2.

Source of Variance	Square Sum	dof	Mean Square	Fo	Fcrit	P-value	Conclusion
Antenna Height [m]	0.428	1	0.428	11.95	3.85	0.0006	Significant
Error	20.28	566	0.036				
Total	20.708	567					

A LSD test (*Fisher's Least Significant Difference between means*) is performed to determine if the radar antenna heights leads to a different shadowing behaviour [210]. Table 4.4 summarizes the LSD results. There are two homogeneous zones of operation considering the LSD value of 0.031. Thus, when the radar antenna height decreases, the amount of intensities with shadowing effects increases being in good agreement with the range dependence of shadowing. We conclude that method 2 allows a better characterization of shadowing effects throughout range.

TABLE 4.4: Results from Fisher's Least Significant Difference (LSD) test.

Height	Mean	Groups		Description
20 m	0.203	X		Few intensities affected by shadowing
10 m	0.258		X	Many intensities affected by shadowing

4.4 Proposed Approach for Sea State Monitoring in Coastal Environments

Considering the shadowing characterization described above, it is possible to remove shadowing effects on sea clutter images applying image enhancement techniques based on filtering and interpolation approaches. The proposed method can be described following the steps presented in Figure 4.6.
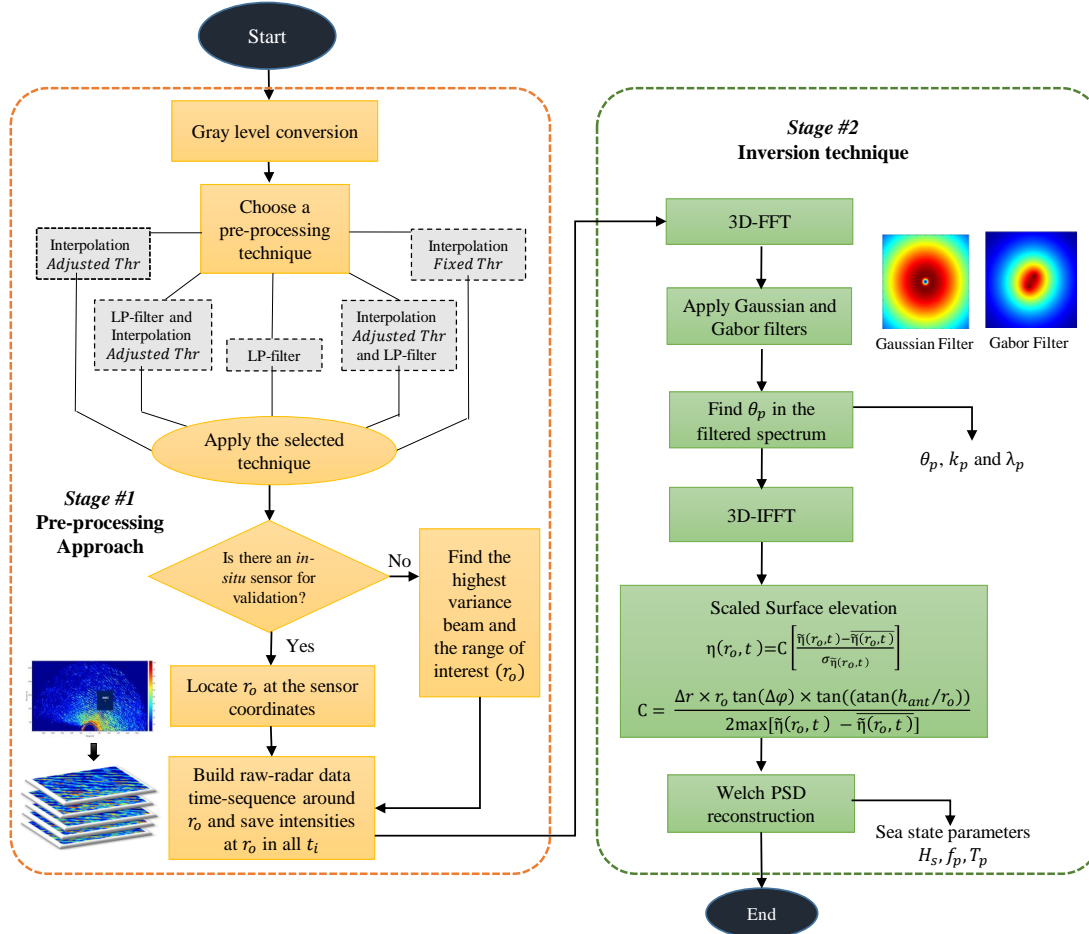
Figure 4.6: Flow diagram of the data processing approach for sea state monitoring in coastal areas.

The procedure considers two main stages: a pre-processing approach and an inversion technique, which are described in detail in this section. The pre-processing approach aims to compensate the distortions introduced by the radar acquisition process and shadowing effects. The inversion technique applies Gauss and Gabor filters on the image spectrum instead of an empirical MTF adjust to estimate sea state parameters from the directional wave spectrum [2], [40].

4.4.1   Pre-processing approaches

To determine the most appropriate image enhancement technique for improving the estimation of sea state parameters in coastal areas, five different approaches based on filtering and interpolation are examined. The proposed methods are: (1) filtering, (2) interpolation with adjusted threshold, (3) interpolation with fixed threshold, (4) filtering and interpolation with adjusted threshold (in this order) and (5) interpolation with adjusted threshold and filtering (in this order).

The assessment of each technique considers the recognition of clear wave patterns, the stability of the sea clutter intensities along range and the mitigation of shadowing effects in the sea clutter images. It is worth to note that the pre-processing approaches are applied on each intensity beam of the entire raw sea clutter images collected by the X-Band radar system in the coverage area.

Filtering

The filtering approach considers the design of a zero-phase Butterworth Low-Pass (LP) selective filter with order n= 44 and cutoff frequency of 0.5 Hz. The wind wave frequencies are considered to be between 0.033 Hz and 0.485 Hz [211]. Figure 4.7a illustrates the raw and filtered RCS from the highest variance beam of the sea clutter image obtained by the X-Band radar from S3 dataset at 11:08 UTC. It can be seen that the LP filter intensifies lower intensities and reduces higher sea clutter data at the most remote distances from the radar antenna.

Interpolation

The interpolation approach considers that shadowing modulation and the power decay of the radar signal along range can be compensated interpolating the lowest intensities using at least two neighbouring pixels. The threshold value from the interpolation procedure defines whether a RCS is affected by shadowing modulation.

Considering the method 2 of the empirical shadowing characterization above described, pixels from the sea clutter images whose intensities are lower than the proposed threshold are considered to be affected by shadowing. In this regards, two linear interpolation approaches are proposed. The first one considers a fixed threshold of 350 units of intensity quantized to 10 bits (which corresponds to a gray level of 87) taking into account the methodology proposed in [212]. The second approach proposes an adjusted threshold that has the value of the smallest intensity obtained from the third-order polynomial approximation that is fitted to the mean RCS along range.

Figure 4.7b presents the raw and interpolated RCS from the highest variance beam of a sea clutter image (S3 dataset at 11:08 UTC). Both interpolation approaches with fixed (dark blue dotted line) and adjusted threshold (light blue dotted line) are considered. As depicted Figure 4.7b, the adjusted threshold value remains constant along range for the beam of interest. However, it can vary with time and wave conditions, whereby the interpolation approach considers a threshold value that is adjusted for each radar image.

In addition, the overlaid plot in Figure 4.7b shows that the interpolation with fixed threshold causes a significant distortion on the sea clutter signal along range, changing the sea state information obtained from X-Band radar images.

Combination of filtering and interpolation with adjusted threshold approaches

Considering the advantages obtained by using filtering and interpolation approach on raw radar images, the improvement resulting from the combination of these both techniques is evaluated. As already stated, the interpolation approach with adjusted threshold reduces significantly shadowing effects causing irregular areas in the most remote ranges and the LP filter intensifies lower RCS and reduces higher sea clutter data. The *a priori* results suggest that the combination of both approaches can improve the estimation of sea state parameters. The combinations consider the filtering and interpolation as well as the interpolation and filtering techniques that are applied on the raw radar image in this order.

The overlaid plot in Figure 4.7c depicts the sea clutter data along range from the highest variance beam of the raw radar and the processed image using the combinations of filtering and interpolation approaches. According to Figure 4.7c, when the radar images are interpolated after applying the LP filter, the RCS of the shaded areas is filled with information of the surrounding pixels, whereby sea state data are intensified in these regions.
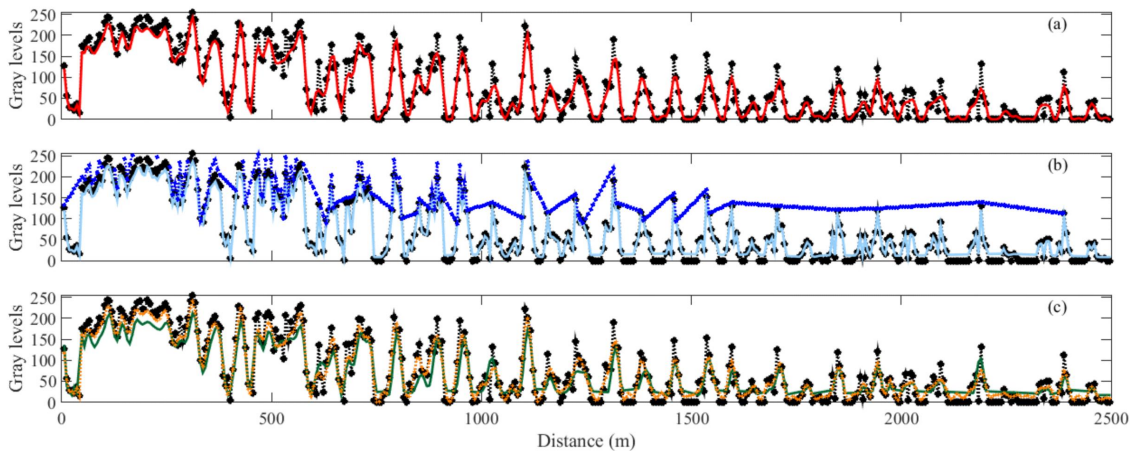
Figure 4.7: Pre-processing techniques in comparison to raw RSC: **(a)** filtering (red line), **(b)** interpolation with adjusted threshold (light blue line) and fixed threshold (dark blue line) and **(c)** using the combination of filtering and interpolation approaches from the highest variance beam intensities of S3 dataset at 11:08 UTC. Black and orange dotted line represent the raw and the interpolated and filtered RCS, respectively. Green line corresponds to the filtered and interpolated sea clutter data.

Figure 4.8 shows the differences between gray level intensities obtained from each preprocessing approach and the raw radar amplitudes, which are normalized by the maximum gray level value (255). According to Figure 4.8a, wave patterns imaged by the radar system are clearer than those observed in the raw radar data reducing higher sea clutter data at the most remote distances using the LP filter. It can be seen that the adjusted interpolation reconstructs the wave fields and enhances raw radar data in Figure 4.8b. However, in some areas, mainly more than 2 km away from the radar antenna, the interpolation technique cannot be applied properly since there are not sufficient neighbouring pixels whose intensities are higher than the threshold resulting in irregular sea clutter areas [91], [209]. As shown in Figure 4.8c, the wave patterns imaged by the radar are more distinguishable using the LP filter and the interpolation approach, providing clearer wave field information. Section 4.5 examines the improvement resulting from

each pre-processing technique to estimate sea state parameters through spectral analysis.
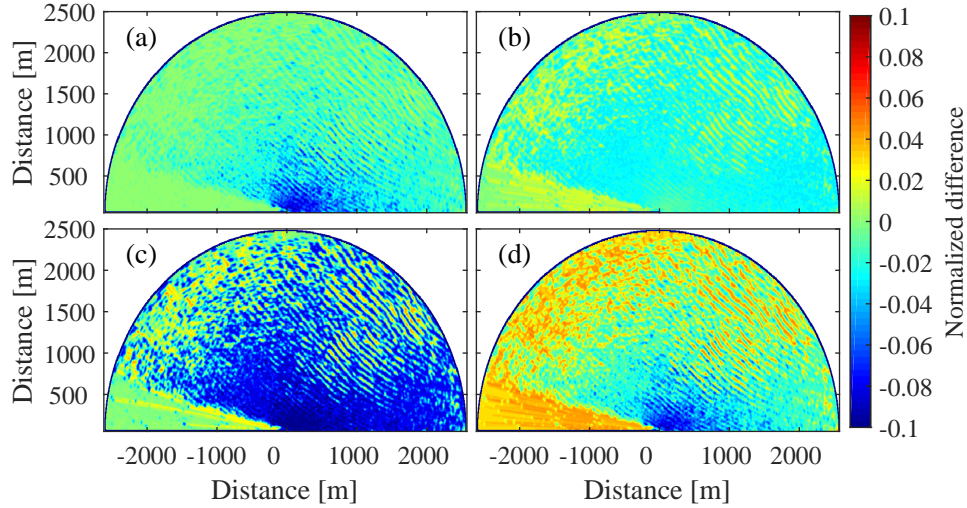
Figure 4.8: Normalized differences between the raw radar image and processing images acquired in Salgar beach from S3 dataset at 11:08 UTC using **(a)** filtering, **(b)** interpolation, **(c)** filtering and interpolation, **(d)** interpolation and filtering approaches.

Afterwards, time-sequence regions of 128×128 pixels are built centred at in-situ sensor coordinates (r_0) or at a range of interest from the highest variance beam. Then, processed regions are turned on gray scale and intensities at r_0 are saved for all t_i.

4.4.2   Inversion technique

The three-dimensional Fast Fourier Transform (3D-FFT) from the processed radar time-sequence is computed and the Gauss and Gabor spatial filters applied. The effect of the two-dimensional Gaussian smoothing is to blur the radar image eliminating the dependence on modulation effects along range.

As depicted in Figures 4.9a and 4.10a, the Gauss High-Pass (HP) filter eliminates the peak spectral intensity that appears around $f = 0$ Hz due to the mean RCS decay along range direction that can be defined as function of the antenna height above the mean mean sea level. The Gabor Band-Pass (BP) filter intensifies the swell peaks that appear in the directional (k_x, k_y) spectrum, as shown in Figures 4.9b and 4.10b. The spectral peaks are identified convolving a square window of ones (3×3 pixels) with the two-dimensional wave spectrum filtered through the Gaussian smoothing. This window moves around overlapping region of equal size inside the two-dimensional spectrum.

The 2D-FFT is obtained from the sum of the magnitudes derived from 3D Fourier coefficients in the third dimension (i.e. time). The maximum values of this convolution correspond to the swell peaks $(k_{x_{max}}, k_{y_{max}})$, as explained in Appendix B. It is worth to note that k_{max} vector has two maximum values due to the symmetrical form of the directional wave spectrum. Considering

these spectral peaks, the peak wavenumber, $k_p = \sqrt{k_{x_{max}}^2 + k_{y_{max}}^2}$, and the peak wavelength defined as $\lambda_p = 2\pi/k_p$ are estimated.

Analytically, the Gauss $\hat{\Psi}(k_x, k_y)$ and Gabor $\hat{\Omega}(k_x, k_y)$ filters are

$$\hat{\Psi}(k_x, k_y) = \exp\left(\frac{-|\vec{k}|^2}{2\sigma_{k_x}^2}\right) - \exp\left(\frac{-|\vec{k}|^2}{2\sigma_{k_y}^2}\right) \tag{4.1}$$

$$\hat{\Omega}(k_x, k_y) = \exp\left(\frac{-|\,(k_x - k_{x_{max}}) + (k_y - k_{y_{max}})\,|^2}{2\sigma_k^2}\right) + \\ \exp\left(\frac{-|\,(k_x + k_{x_{max}}) + (k_y + k_{y_{max}})\,|^2}{2\sigma_k^2}\right) \tag{4.2}$$

where $|\vec{k}|$ corresponds to the magnitude of the wavenumber vector defined as $\sqrt{k_x^2 + k_y^2}$. Besides, σ_{k_x}, σ_{k_y} and σ_k are the standard deviation that define the filter bandwidth in the corresponding dimensions. The spatial filters are multiplied with the complex Fourier coefficients of the directional wave spectrum in order to remove the Fourier coefficients with non-relevant information about sea state.

Figure 4.10b depicts the processed directional spectrum obtained by S3 dataset at 11:08 UTC using both Gauss and Gabor filters, in this order. The directional spectrum has one dominant spectral wave direction around 25.6° (north-east).
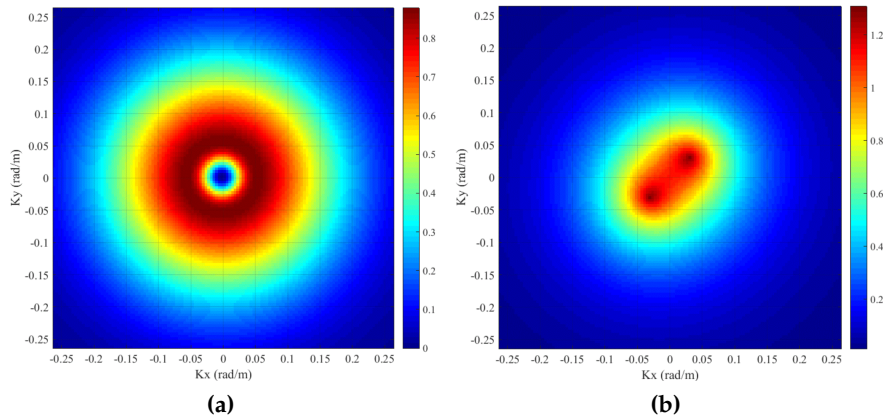
Figure 4.9: (a) High-Pass Gauss filter and **(b)** Band-Pass Gabor filter.

Sea surface elevation $\tilde{\eta}(r, t)$ is reconstructed by inverse Fourier Transform (3D-IFFT) using the filtered directional spectrum (Figure 4.10b). It is worth to note that $\tilde{\eta}(r, t)$ corresponds to not properly scaled values in gray levels of the true sea surface elevation $\eta(r, t)$ because sea clutter data depicts directly the electromagnetic echo intensities rather than sea surface displacement [82]. Here, $\tilde{\eta}(r_0, t)$ represents the sea surface elevation at range r_0 that is scaled as $\eta(r_0, t) = CZ_{\tilde{\eta}(r_0,t)}$, being C defined as [2],

$$C = \frac{\triangle r \tan(\Phi) r_0 \tan(\triangle\varphi)}{2\max(\tilde{\eta}(r_0, t) - \overline{\tilde{\eta}(r_0, t)})} \tag{4.3}$$
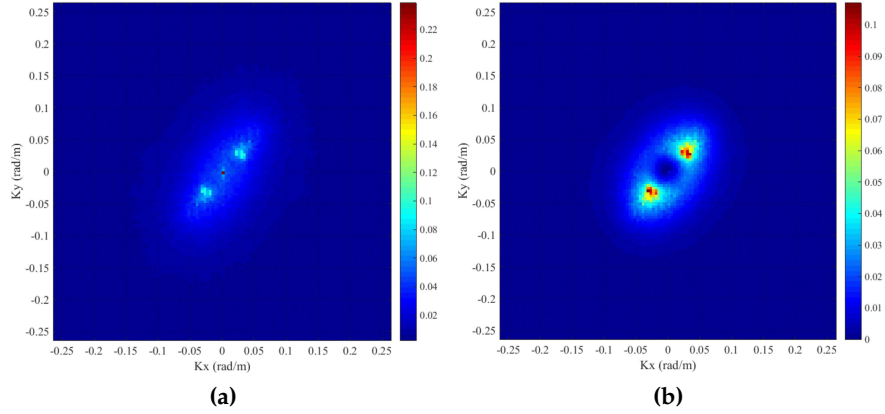
Figure 4.10: (a) Raw and **(b)** processed directional wave spectra using Gauss and Gabor filters to suppress spectral noise components.

and $Z_{\tilde{\eta}(r_0,t)}$, the normalization of the $\tilde{\eta}(r_0,t)$ values with respect to the noise level using its standard deviation, is given by,

$$Z_{\tilde{\eta}(r_0,t)} = \frac{\tilde{\eta}(r_0,t) - \overline{\tilde{\eta}(r_0,t)}}{\sigma_{\tilde{\eta}(r_0,t)}} \tag{4.4}$$

where $\triangle r$ and $\triangle \varphi$ are the spatial resolution and the horizontal beam resolution of the radar system (6 m and 1.35°, respectively). In addition, the maximum value of $\tilde{\eta}(r_0,t)$ is used for normalizing the area computed in the numerator of the relation. Besides, the grazing incidence angle Φ is defined as $\arctan(h_{ant}/r_0)$ being h_{ant} the radar antenna height, as shown in Figure 4.11a [110]. Finally, $\sigma_{\tilde{\eta}(r_0,t)}$ and $\overline{\tilde{\eta}(r_0,t)}$ represent the standard deviation and the mean value of $\tilde{\eta}(r_0,t)$, respectively. Note that empirical MTF correction is replaced by a scale factor using radar parameters instead of external in-situ reference data as a novel contribution.
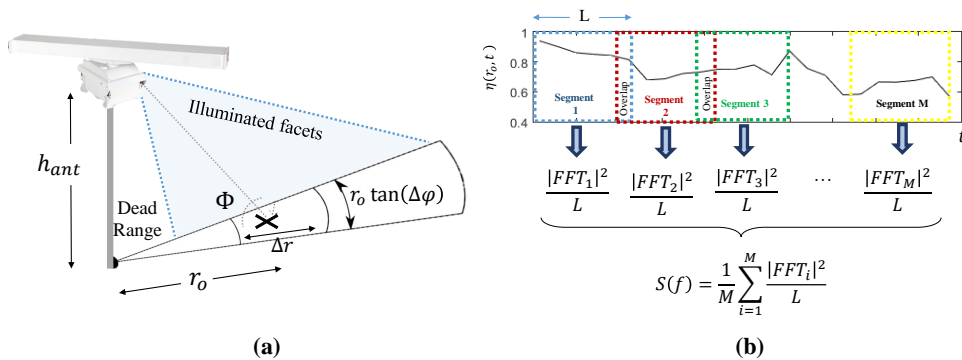
Figure 4.11: (a) Geometrical parameters considered to obtain $S(f)$ from a single illuminated facet located at r_0. **(b)** Welch PSD method to compute periodograms through overlapping Hamming windows of length L.

Wave energy spectral density is obtained considering the temporal sequence of scaled $\eta(r_0,t)$ by using Welch PSD methodology. Welch method divides each set of 128 samples in 16 overlapping Hamming windows of equal size to compute periodograms. These periodograms are averaged

to obtain an adequate estimation of wave spectral density. Figure 4.11b describes this spectral procedure [2], [40]. H_s, T_p and f_p are estimated by means of the frequency spectrum derived from the computed wave elevation map taking into account that $H_s = 4\sqrt{E}$, where E is the energy of the frequency spectrum and $T_p = 1/f_p$, where f_p is the peak frequency of the wave spectral density $S(f)$.

Wave energy spectra derived from radar data are compared agaltts the spectrum recorded by the in-situ system as well as the semi-empirical JONSWAP spectrum proposed by Hasselmann *et al.* [213]. The JONSWAP formulation describes local wind-generated seas with limited *fecth* defined as,

$$S(\omega) = \frac{\alpha g^2}{\omega^5} \exp\left[\frac{-5}{4}\left(\frac{\omega_p}{\omega}\right)^4\right] \gamma^{\exp\left[-(\omega-\omega_p)^2/2\sigma^2\omega_p^2\right]} \tag{4.5}$$

where $\omega = 2\pi f$ is the wave angular frequency in radians, ω_p is the peak ω that is computed with the peak frequency f_p in Hz of the wave frequency spectrum, γ is the peak-shape parameter that is usually chosen as 3.30 and σ is 0.07 for $\omega \leq \omega_p$ and 0.09 for $\omega > \omega_p$. The values of γ vary approximately from 1 to 6 even for a constant wind speed since γ is actually a random variable normally distributed with mean 3.30 and variance of 0.62. However, γ is obtained from analysis of the measured data [20].

In this case, γ is adjusted to 3.49 according to radar measurements and the constant αg^2 is obtained from the peak value of the wave frequency spectra $S(\omega_p)$. In addition, the mean value of the scale parameter, α, is 0.0267 with a standard deviation of 0.0145. The values of these parameters are in good agreement with the analysis presented in [214] for the Colombian Caribbean coast. The JONSWAP formulation is used for the validation of sea clutter data obtained from radar system through the assessment of good agreement between radar wave frequency spectrum and JONSWAP semi-empirical spectrum.

4.5 Results

4.5.1 Salgar beach dataset

The proposed algorithm uses regions of 128×128 pixels from the digitized radar image. The sea state information derived from nine 128 time-sequence radar images sets (S3 dataset) is analysed in detail. According to hourly AWAC data, H_s was 1.92 m and 1.93 m, T_p was 8.75 s and 8.47 s, f_p was 0.1142 Hz and 0.1181 Hz, and θ_p corresponded to 21.61° and 25.65° from 09:29:17 and 10:29:17 (UTC), respectively. Table 4.5 presents the percentage relative error, $R(r_0)$, and the corresponding bias error, $D(r_0)$, between X-Band radar estimates $\hat{\chi}(r_0)$ of the ground truth values $\chi_{true}(r_0)$ from the sea state parameters H_s and θ_p derived from AWAC data, which are computed to measure the performance of the proposed techniques.

Results show that T_p is estimated with the same accuracy using the different pre-processing approaches. This fact suggests that the enhancement procedure of the raw radar images does not affect the estimation of the sea state parameter retrieved with high accuracy. From 09:29:17

TABLE 4.5: Percentage relative error and absolute error between radar estimation
and AWAC in-situ data

Pre-processing approach	Time (UTC)	H_s	θ_p
Raw image	09:29:17	9.64% (-0.19 m)	2.20% (0.48°)
	10:29:17	8.35% (-0.16 m)	9.354% ($-2.39°$)
Filtering	09:29:17	7.31% (-0.14 m)	2.20% (0.48°)
	10:29:17	5.97% (-0.12 m)	9.354% ($-2.39°$)
Interpolation with adjusted threshold	09:29:17	13.63% (0.26 m)	2.20% (0.48°)
	10:29:17	15.38% (0.30 m)	5.94% ($-1.52°$)
Filtering and interpolation	09:29:17	1.25% (0.02 m)	2.20% (0.48°)
	10:29:17	2.72% (0.05 m)	5.94% ($-1.52°$)
Interpolation and filtering	09:29:17	14.22% (0.27 m)	2.20% (0.48°)
	10:29:17	16.05% (0.31 m)	5.94% ($-1.52°$)

and 10:29:17 (UTC), the estimation errors are 1.67% (-0.15 s) and 1.59% (0.14 s) for T_p, 1.70% (1.88mHz) and 1.56% (-1.79 mHz) for f_p, respectively. In addition, k_p and λ_p are estimated from the radar data using the directional wave spectrum, being retrieved as 0.0818 rad/m and 76.8 m, respectively.

Analysing the measurements in Table 4.5, the best performance is obtained from filtered and interpolated radar images with an adjusted threshold. In this regards, the significant wave height was retrieved with a maximum error of 2.72% (about 0.05 m). The estimation errors of the peak period and the peak wave direction were below 0.15 seconds and 2°, respectively. As shown in Table 4.5, the significant wave heigh is over-estimated by the interpolation with adjusted threshold and using the interpolation and filtering procedure. Besides, H_s is under-estimated by the raw radar and the filtering method mainly because shaded areas are still present. However, the assessment of the statistical difference among the estimation of the sea state parameters derived from each pre-processing method needs to be examined in order to identify whether the percentage of relative error is significant and to determine a single pre-processing approach with the best results.

Figure 4.12 illustrates the comparison of the average frequency spectra derived from the estimated wave elevation map using the different pre-processing approaches described above (dashed gray line), the semi-empirical JONSWAP spectrum adjusted with the peak amplitude and frequency of the radar $S(f)$ (red line), and the AWAC record (black line) at 8 m depth at $r_0 = 1.4$ km away from the radar antenna. Note that the three spectra present the best agreement for the filtered and interpolated radar images. Besides, a good agreement between the spectra derived from AWAC record and radar data is obtained. It is of interest to note that the shape of the JONSWAP spectrum does not completely coincide with the radar data because it considers older waves (i.e. waves whose ratio between their speed of propagation and the wind speed tends to infinity) but the measured waves are not necessarily saturated.

4.5.2   Castelldefels beach dataset

The proposed techniques are tested using regions of 128×128 pixels from the MUSAFELS datasets C2, C3 and C5, whose peak periods are five times higher than the temporal resolution
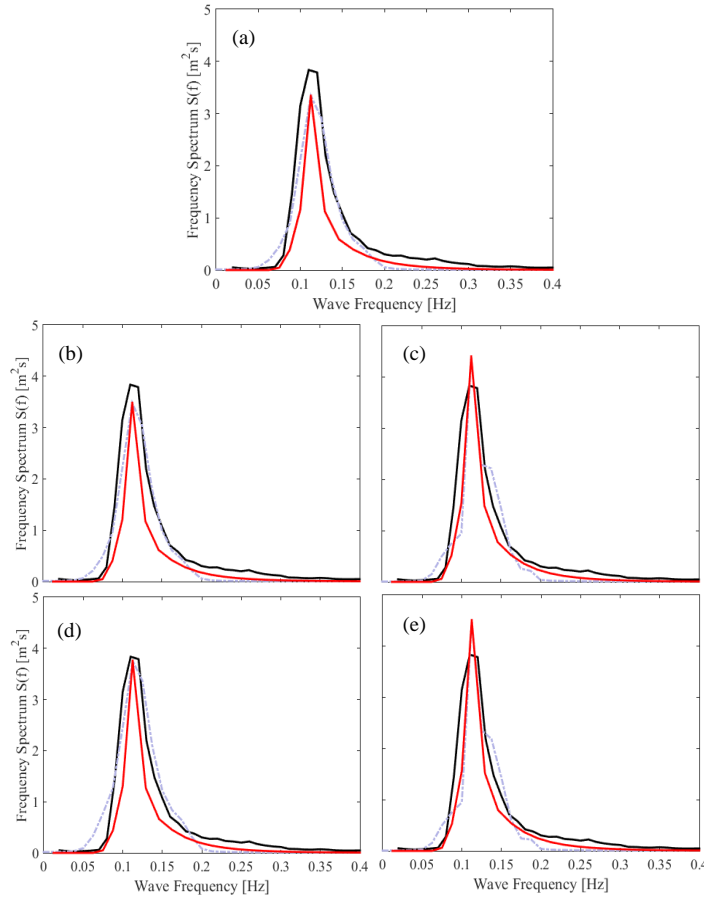
Figure 4.12: Comparison of the wave frequency spectra derived from the AWAC record (black line), the X-Band radar wave elevation maps (gray dashed line) and the JONSWAP adjust (red line) from S3 dataset using the **(a)** raw, **(b)** filtered, **(c)** interpolated with adjusted threshold, **(d)** filtered and interpolated and **(e)** interpolated and filtered time sequence radar images.

of the radar system ($5\triangle t = 6.25$ s). The other three datasets (C1, C4 and C6) will be used for discussing the strengths and weaknesses of the system in Section 4.6.

Figure 4.13 presents the scatter plot between the radar-retrieved H_s, T_p and θ_p and the AWAC-retrieved data for all the pre-processing techniques. From Figure 4.13, it can be observed that the combination of filtering and interpolation approaches (square markers) has a better performance than the others pre-processing techniques. In this case, the correlation coefficients, r, between the radar estimates and the external reference are 0.8, 0.91 and 0.46 for H_s, T_p and θ_p, respectively. Besides, the root mean square error (RMSE) of the raw images is 0.16 m for H_s but the RMSE of the best performance technique is 0.12 m. Additionally, the scattered distribution is more concentrated when applying the combination of filtering and interpolation approaches than the others techniques. In general, it can be seen that T_p estimates are in good agreement with in-situ measurements for all the analysed approaches. Therefore, the pre-processing techniques do not affect significantly the performance of this sea sate parameter, as mentioned above for the data retrieved in Salgar.

To further verify the effectiveness of the filtering and interpolation approach, Figures 4.14a and
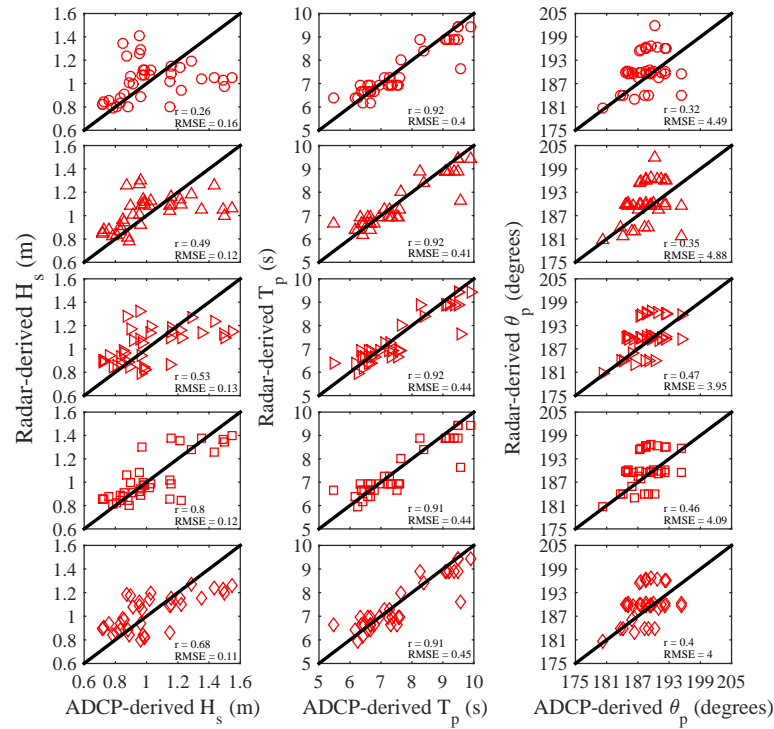
Figure 4.13: Scatter plots of H_s, T_p and θ_p between the radar-retrieved data and the AWAC record using all the pre-processing techniques. Circles depict the estimates from the raw radar images. Triangles are the results from the filtering approach. Triangle toward right markers represent the interpolation technique. The filtering and interpolation are the square markers. Finally, the results from the interpolation and filtering approaches are presented using the diamond markers.

4.14b depict the scatter plots for H_s and T_p, respectively, from March 16th to March 18th at the ADV locations. According to these scatter plots, the best performance pre-processing technique is the combination of filtering and interpolation approaches with a correlation coefficient of 0.9, 0.85 and 0.86 for H_s radar estimates derived from ADV-1 ($h = 3.8$ m), ADV-2 ($h = 5$ m) and ADV-3 ($h = 7$ m) data, respectively.

As mentioned above, T_p is estimated with high accuracy for all the pre-processing approaches. However, the performance for H_s radar estimates is gradually improved when the distance from the radar antenna decreases. It could be explained considering the shoaling theory and the morphology of the Castelldefels beach that cause better defined waves with stronger echo intensities and higher wave heights in the nearshore area than at the AWAC location (21 m depth).

Figure 4.15a illustrates the comparison of the average frequency spectra derived from the estimated wave elevation map using the pre-processing approaches and the AWAC record (black line). Figure 4.15b, 4.15c and 4.15d consider the ADV 1, 2 and 3 record, respectively. Note that the four spectra present the best agreement for the filtered and interpolated radar images. Besides, the peak amplitude of the wave energy spectra increases when the distance from the radar antenna decreases because of shoaling and beach morphology of the Castelldefels coast, as mentioned above. These experimental results confirm that the filtering and interpolation technique can improve the accuracy of the sea state parameter estimates, even at closer distances from the radar.
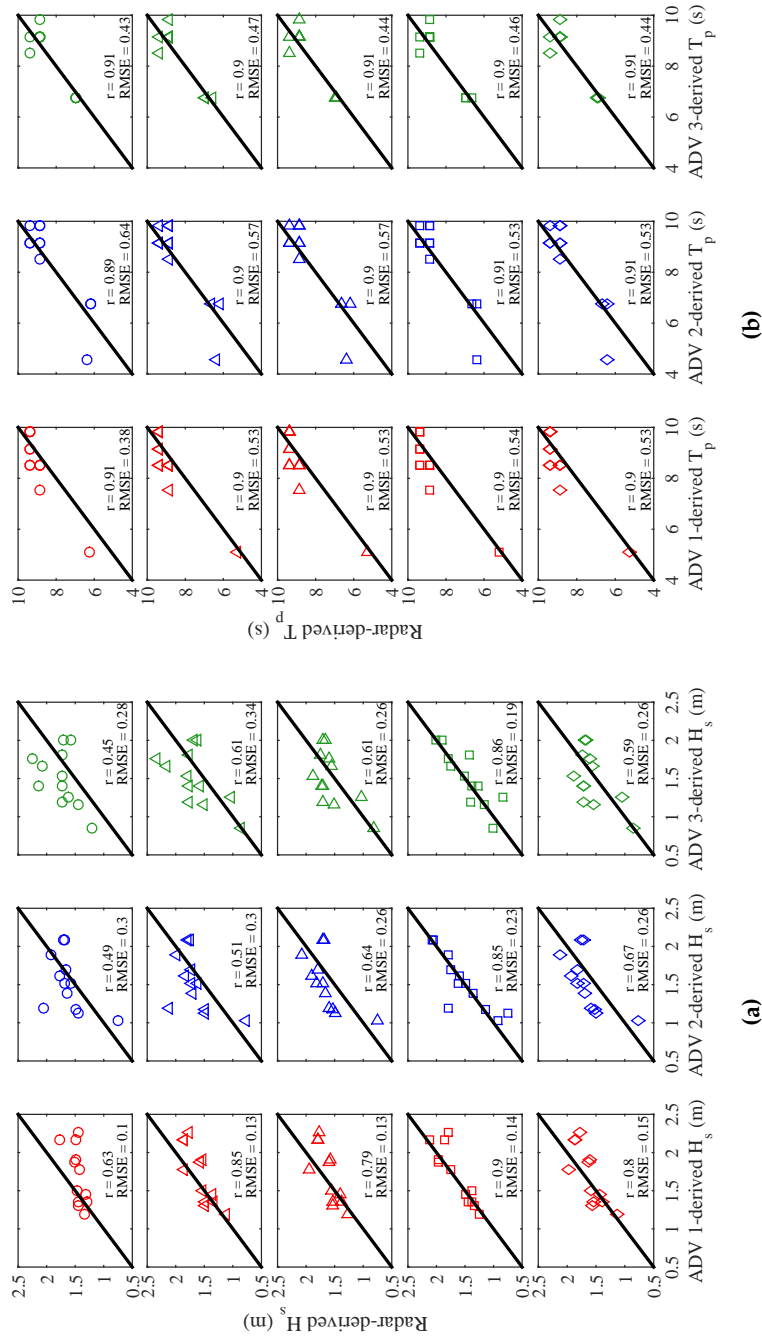
Figure 4.14: Scatter plots of (a) H_s and (b) T_p between the radar-retrieved data and the ADVs record using all the pre-processing techniques. Circles depict the estimates from the raw radar images. Triangles are the results from the filtering approach. Triangle toward right markers represent the interpolation technique. The filtering and interpolation are the square markers. Finally, the results from the interpolation and filtering approaches are presented using the diamond markers. Red, blue and green markers corresponds to ADV-1 ($h = 3.8$ m), ADV-2 ($h = 5$ m) and ADV-3 ($h = 7$ m) data, respectively.
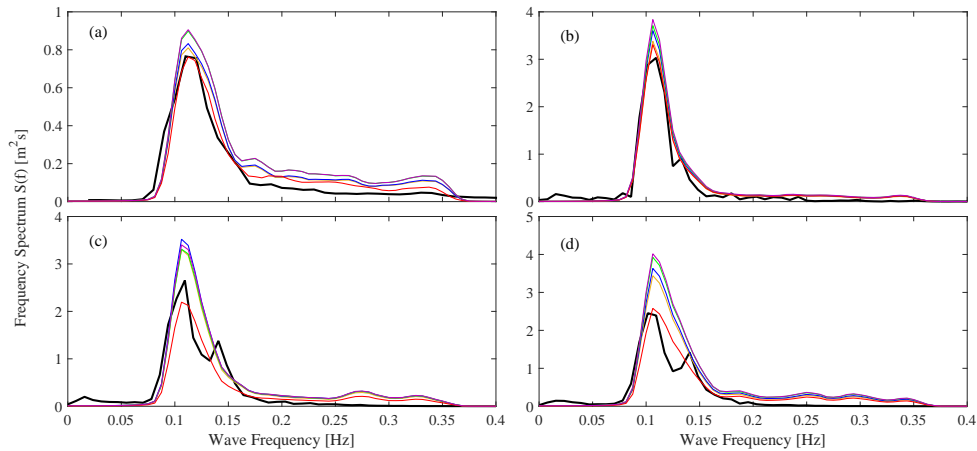
Figure 4.15: Comparison of the wave frequency spectra derived from radar processed images and the **(a)** AWAC, **(b)** ADV-1, **(c)** ADV-2 and **(d)** ADV-3 record at 21 m, 3.8 m, 5 m and 7 m water depth, respectively. Black lines represent the spectra obtained from in-situ measurements. Yellow lines show the corresponding wave frequency spectra using raw radar data. Blue and green lines represent the radar-retrieved spectra from filtered and interpolated images, respectively. Finally, the wave frequency spectra from the combination of filtering and interpolation approaches are depicted using red lines for the filtered and interpolated time-sequence radar images and purple lines for the interpolated and filtered sea clutter images.

4.6 Discussion

4.6.1 Salgar beach dataset

An ANOVA test is performed using the estimation of H_s obtained from the different methods listed in Table 4.5. This sea state parameter gives relevant information to identify statistical differences among the pre-processing methodologies. Results are summirazed in Table 4.6. SoV, SS, MS and dof refer to Source of Variance, Square Sum, Mean Square and degrees of freedom, respectively.

TABLE 4.6: ANOVA results from S3 dataset. H_s estimates are obtained from raw radar images and using filtering, interpolation and the combinations of filtering and interpolation approaches.

SoV	SS	dof	MS	Fo	Fcrit	P-value	Conclusion
Method	1.720	4	0.43	61.07	3.06	0.0	Significant
Error	0.282	40	0.007				
Total	2.002	44					

The ANOVA is computed using the decomposition of squares sum procedure [210] and considering nine H_s estimates retrieved from five different methods. This fact produces an entire process of 45 values of H_s analysed. According to Table 4.6, the critical F-value (3.06) is lower than the observed F-value (61.07) whereby the pre-processing method affects significantly the estimation of H_s. In addition, a statistically significant difference can be observed with a confidence level of 95% since P-value is lower than $\alpha = 0.05$.

According to the P-value of the Shapiro-Wilks test (0.477) which is greater than $\alpha = 0.05$, the residuals obtained from the ANOVA test can be fitted to a normal distribution with a confidence level of 95%. The Bartlett test has a P-value of 0.965 (greater than $\alpha = 0.05$) whereby the homoscedasticity assumption of residuals is complied with a confidence level of 95%. Finally, the confidence interval of Lag 1 contains the zero value [-0.1997, 0.2921] that allows the validation of the independence assumption.

Once the ANOVA results have been validated, a LSD test is performed to examine the mean values of H_s estimates retrieved from the different methods using a confidence intervals of 95%. Table 4.7 summarizes the LSD results. It can be seen that three homogeneous groups are identified which do not exceed LSD value of 0.079 m.

TABLE 4.7: Results of Fisher's Least Significant Difference (LSD) test.

Method	Cases	Mean	Homogeneous groups			Group description
Raw Image	9	1.750	X			Under-estimation of H_s
Filtering	9	1.795	X			Under-estimation of H_s
Filtering and interpolation	9	1.961		X		Accurate estimations of H_s
Interpolation	9	2.202			X	Over-estimation of H_s
Interpolation and filtering	9	2.214			X	Over-estimation of H_s

As shown in Table 4.7, H_s estimates are statistically equal using the raw radar images and the LP filter approach. Besides, these methods under-estimate H_s since they have the lowest mean values (1.75 m and 1.795 m, respectively). In addition, an over-estimation of H_s is obtained from the interpolated and the interpolated and filtered images without statistical difference between both procedures. Finally, the filtering and interpolation approach gives the most accurate estimations of H_s. It can be concluded that the filtering and interpolation approach allows removing shadowing in coastal areas, obtaining the estimation of the sea state parameters with the highest resolution and accuracy.

4.6.2 Castelldefels beach dataset

In order to examine the performance of the filtering and interpolation technique during very mild sea state conditions (lower peak periods and wave heights), Figure 4.16 depicts the bias error, $D(r_0)$, including the C1, C4 and C6 datasets. It can be seen that the estimation accuracy relies on both peak period and significant wave height. The highest bias errors are obtained from waves of the C1 dataset, where $T_p < 6$ s and $H_s < 0.45$ m. Besides, Figure 4.16 shows that the bias error is acceptable even for waves whose T_p are lower than 6.25 s (i.e. $T_p < 5\Delta t$, where $\Delta t = 1.25$ s is the temporal resolution of the radar system) but with $H_s \geq 0.5$ m.

Since the filtering and interpolation technique depends on recording high signal-to-noise ratio (SNR) sea clutter data, the method needs sufficient wave action to operate properly. Therefore, it is possible to obtain the most accurate wave parameters estimates in nearshore areas when the following conditions are fulfilled simultaneously: (1) H_s is at least 0.5 m and preferably higher; (2) $T_p \geq 4$ s. Besides, the best quality data are collected when T_p is higher than the temporal resolution of the radar system and the first criteria is fulfilled. In this case, bias error is almost zero, as shown in the right side of Figure 4.16.
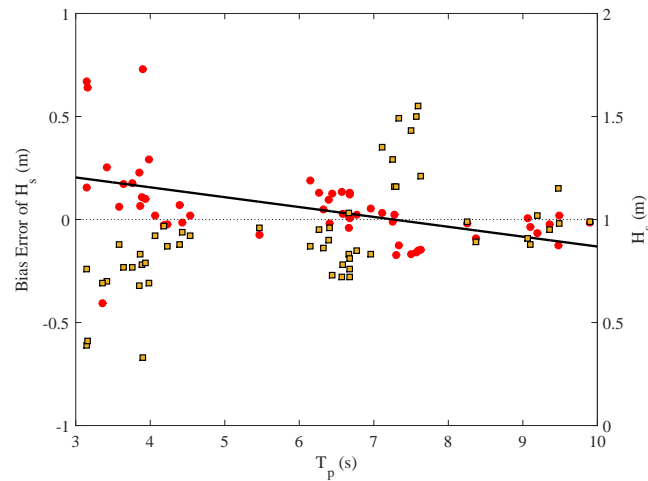
Figure 4.16: Scatter plot of the error bias of H_s estimates with respect to peak period, considering the AWAC record as the true values of H_s, which are depicted as yellow square markers. Red circles represent the retrieved error bias and the black line corresponds to the first-order polynomial function that best fit their behaviour along T_p with r = 0.49.

4.7   Summary

The proposed shadowing mitigation method allows the estimation of sea surface elevation distribution in coastal areas through sea clutter data obtained from X-Band marine radar systems in extreme grazing incidence angles without calibration neither empirical MTF adjusts. This method considers temporal sequences of processed marine radar images and inversion techniques based on FFT analysis to obtain wave properties in the frequency domain. The FFT analysis is physically meaningful when the intensity sea clutter signals are a reasonable proxy of actual wave conditions. Therefore, shadowing effects in extreme grazing incidence angles need to be removed in order to eliminate noise and to improve the estimates of sea state parameters in shallow waters. The method compensates distortions introduced by the radar acquisition process and the power decay of the radar signal along range applying image enhancement techniques through a couple of pre-processing steps based on filtering and interpolation of the images [2].

To mitigate shadowing, an investigation was carried out to examine empirically the behaviour of the sea clutter intensities along range direction to determine the best threshold value for the interpolation approach that explains shadowing behaviour. The characterization considers data provided by X-Band radar systems deployed at two different heights above the mean sea level (10 and 20 m). Results reveal that an ever-increasing amount of intensities affected by shadowing arises as the distance from the radar antenna increases as expected. In this regards, the threshold value for the interpolation approach considers the influence of the antenna height above the mean sea level on shadowing modulation effects. Shadowing has not previously analyzed in detail considering beam intensities behaviour along range at two different radar antenna heights.

To develop the methodology, the improvement resulting from five pre-processing approaches are evaluated considering sea clutter data collected by a FR-8252 X-Band marine radar. A LP

filter and an interpolation with adjusted threshold were proposed. Results reveal that filtering intensifies lower intensities and reduces the sudden peaks of sea clutter data that appear at the most remote distances from the radar antenna. In addition, the interpolation approach reduces significantly shadowing modulation effects. Wave patterns imaged by the radar are more distinguishable by using the combination of these two approaches (filtering and interpolation, in this order). The inversion technique considers High-Pass Gauss and Band-Pass Gabor filters instead of MTF approach. The effect of the Gaussian smoothing is to blur the radar image eliminating the dependence on modulation effects along range. The Gabor Band-Pass (BP) filter intensifies the swell peaks that appear in the wave directional spectrum which contain relevant information about sea state.

Regarding filtering and interpolation approach, errors for H_s, θ_p and T_p calculated as the difference between estimated and true data show a mean bias and a relative value of 0.05 m (2.72%), 1.52° (5.94%) and 0.15 s (1.67%), respectively. In addition, the directional wave spectrum yields accurate θ_p, k_p and λ_p estimates using this pre-processing technique. The results also show good agreement in the overlaid plot of the wave frequency spectra derived from in-situ data, radar estimates and JONSWAP spectrum. It is worth to note that T_p is generally estimated with high accuracy for all the pre-processing techniques. Hence, the accuracy of H_s estimates is the principal criteria that has been taken into account to evaluate the effectiveness of each approach.

According to LSD results, it can be concluded that H_s is under-estimated by the raw radar and filtering method mainly because shaded areas are still present. Besides, the interpolated and the interpolated and filtered radar images over-estimates H_s. Finally, the filtering and interpolation approach gives the most accurate estimations of H_s in extreme grazing incidence angles. The scattered distribution of H_s between the radar estimates and the external reference data is more concentrated using the combination of filtering and interpolation approaches than the others techniques, obtaining correlation coefficients higher than 0.8 which are good outcomes for field datasets. Therefore, the proposed method is able to remove the shadowing and to reproduce with high accuracy the sea state parameters. Finally, the best performance of the method is achieved when H_s is at least 0.5 m and preferably higher and $T_p \geq 4$ s. However, the bias error of H_s is acceptable even for waves whose T_p are lower than 6.25 s but with $H_s \geq 0.5$ m. The flexibility of the mobile radar acquisition system is a significant advantage beside HF radar stations and offshore applications.

Chapter 5

Wave Energy Dissipation in a Shallow Coral Reef Lagoon

"Look at a day when you are supremely satisfied at the end. It is not a day when you lounge around doing nothing, it is when you have had everything to do and you have done it."

Margaret Thatcher (1925 – 2013)

5.1 Introduction

Coral reefs are diverse and vulnerable ecosystems that provide crucial coastal protection services from wave action in tropical and subtropical nearshore regions [215]. They can attenuate about 97% of the wave energy mainly through wave breaking and frictional dissipation processes [216]. The complex structure of coral reefs yields particular wave transformation processes that differ significantly from those of sandy bed systems in at least two main issues. Firstly, coral reefs often form steep and irregular transitions between offshore and shallow water areas that increase the complexity of local bathymetry [13]. Secondly, the presence of canopy-forming benthic organisms produces very rough bottom topography, also named *submerged canopies* [217], [218], which promote bottom friction as an important or even dominant wave energy dissipation mechanism [219], [220]. As a result, both experiments and numerical modelling of coral reef hydrodynamics impose considerable difficulty, since existing theoretical descriptions developed on beaches cannot be successfully extended to coral reef communities [221].

Circulation due to wave breaking on the reef rim provides wave-driven flows and currents that facilitate sediment transport, nutrient uptake and the distribution of massive surrounding biota, e.g. larval fishes and plankton, determining coral reef ecology and productivity [215]. Bottom roughness of coral reefs is closely correlated with ecological diversity, reef health and the permanent hydrodynamics influence of waves and bed shear stress, which in turns define coral reef capabilities of protection and wave energy attenuation [222], [223]. In this context, wave energy dissipation rates provide a quantitative description of coral reef health. Hence, reduced rugosity due to sustained degradation of benthic structural complexity yields lower frictional dissipation and higher probability of erosion and coastal inundation [223].

Climate change and human impacts substantially deteriorate coral reef health through destructive coastal development practices, pollution, overfishing, global warming, ocean acidification and overexploitation. By 2011, global reef mortality reached 19% and 75% of reefs were threatened to suffer coral bleaching which is directly linked to anomalous ocean warming [224]. Hence, detailed and continuous measurements of coral reef systems are considered as a priority to develop protection actions. Most field monitoring global initiatives (e.g. Reef Check program [225]) examine coral reefs from a biological point of view, but rarely are focused on detailed description of hydrodynamics processes of coastal reef-lagoon systems [224].

Echo-sounders and acoustic sensors are traditionally used to map topographic complexity of reef areas. However, they are unable to characterize very shallow waters, reef crest and reef flats due to tide, sea state and shallow-limited performance [224]. In contrast, a variety of remote technologies have been used for habitat mapping and environmental stress assessment including satellite imagery, airborne sensors, unmanned aerial systems, LiDARs and autonomous underwater vehicles. Indeed, SAR satellites (e.g. RADARSAT-1) have provided multiple daily data on coral reefs since 1984, sensing a limited geographic area with higher resolution than scatterometers whose extension is restricted by spatial resolution. Data cost and processing effort establish the level of detail achievable and determine which field survey approach is more appropriate to use [224]. Thereby, remote sensors are complementary and alternative approaches that provide superficial large-scale and often low-resolution data, which are unable to measure seabed features directly, e.g. bottom roughness. Hence, they require in-situ surveys for ground-truth validation [226].

Several studies combine in-situ data and optical multi-spectral satellite imagery with moderate resolution (i.e. pixel sizes from 10 to 30 m) not only to establish sources and causes of coral bleaching [227] but also to obtain detailed classification [228] and delineation [229] of coral reef areas. Future trend suggests the combination of multiple data sources (e.g. remote sensors, in-situ data and numerical modelling) to improve spatial assessment of coral reefs threats, thereby supporting coastal management and conservation services [224].

HF radars (e.g. WERA system [227]) are the one marine radar technology that have been deployed on reef coasts to measure surface currents, wind direction and wave height up to 150 km from the shore, mainly for the assessment of coral bleaching, a phenomenon that leads to long-term coral mortality [230], [231]. This analysis is performed by observing the relationship between stratification of the water column and anomalous warming of the surface water. Using HF radar data, required surface currents to produce vertical mixing are identified, distributing confined heat and minimizing any temperature rise that might lead to coral bleaching [232].

Since X-Band marine radars scan the ocean surface with high spatio-temporal resolution, they may be suitable to measure some prominent features of coral reefs, e.g. wavefields in the outer coral barrier, wave transformation once wave break on the reef front and the remnant energy in the lagoon [233]. However, wave energy dissipation and coastal hydrodynamics have not yet been studied using X-Band marine radars in coral reef environments. Hence, field measurements and validation are still poor [233]. In contrast, dissipation has been extensively studied using in-situ sensors (e.g. ADVs and ADCPs) placed in a straight line, perpendicular to the coastline. Therefore, this Chapter introduces a completely novel use for X-Band radars in coral reef environments by

obtaining wave energy dissipation rates through remotely sensed marine radar data.

The Chapter is outlined as follow. Section 5.2 describes available field datasets collected at San Andres Island, a Colombian Caribbean coral reef system which represents one of the most extensive reef areas in the western Atlantic region [234]. Section 5.3 presents the spectral methodology to compute bottom roughness and friction factors on coral reefs. In Section 5.4, radar-derived H_s data are compared with modeled wavefields and in-situ measurements to verify its performance in a coral reef system. Reef morphology structure is also studied. Besides, two physical wave energy dissipation approaches (Nielsen [12], [13] and Madsen *et al.* [14], [15]) are assessed using radar data. Then, the best performance spectral procedure is identified in Section 5.5 and finally, Section 5.6 concludes the Chapter.

5.2 Field Data

A field experiment was conducted on the barrier reef at the northeastern coast of San Andres Island in 16-17th December 2016. A FURUNO-8252 X-Band marine radar was deployed on the roof of "*Calypso*" hotel at 34 m above MSL with a field view of 180° (12°35′6.2″ N, 81°41′35.8″ W). Radar antenna was oriented 36° NE. Two tide-gauges were located in 4.9 m and 8 m water depth acquiring wave data at 6 Hz. Figure 5.1a gives a general layout of the instrument locations. Chapter 3 gives a more detailed description about the study area.
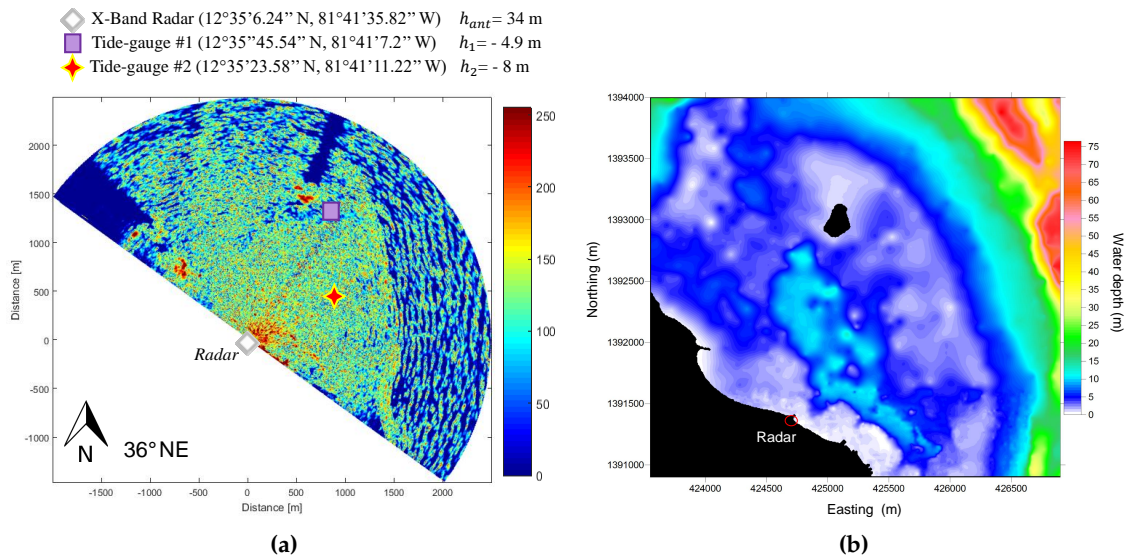
Figure 5.1: (a) General layout of San Andres Island field experiment. Here, h_{ant} and h denote the antenna height and water depth, respectively. Colour bar is the gray level scale used for plotting the radar wavefield. **(b)** Local bathymetry. Red circle indicates the X-band marine radar position.

Local waver depth is depicted in Figure 5.1b using a spatial resolution of 6 m, similar to Δr for the X-Band marine radar system. Bathymetric survey was performed by CIOH Colombian Institute using a multi-beam echo sounder. As it can be seen, water depth is highly heterogeneous in the study area. Reef structure is clearly identifiable from Figure 5.1b. The shallow reef flat has a mean water depth that does not exceed 1 m with an average slope of approximately 1:5. In

contrast, the relatively deep lagoon has heterogeneous water depths ranging from 0.2 to 12.1 m.
Reef morphological structure is also assessed using remotely sensed radar data in Section 5.4.

5.3   Spectral Wave Energy Dissipation Algorithm

Coral reefs protect the coast from wave action through breaking and frictional dissipation in
a highly heterogeneous bathymetry [219], [229]. Figure 5.2a depicts a typical reef morphology
where lagoon depths range from 0.5 to 20 m and gradually descend seaward with mild slopes
until reef flat zone. Then, seabed drops off steeply to the outer reef, where water depths are
greater than 60 m. Thus, the complex geomorphology of a typical barrier reef can be sketched
as Figure 5.2b. Three main regions compose a coral reef barrier: (1) a sloping fore reef, (2) a
shallow reef flat (also named barrier reef or reef rim), and (3) a lagoon with variable depths. This
morphological structure allows transformation of larger incoming waves as they propagate into
back-reef environments [13], [219].
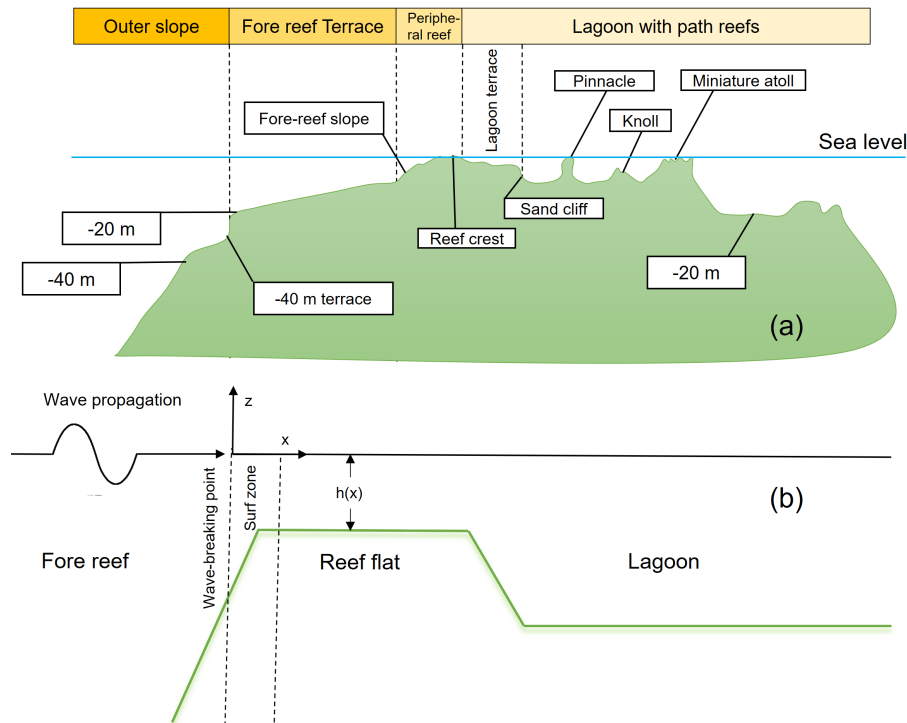
Figure 5.2: Barrier reef structure. **(a)** Geomorphology of a typical barrier reef and some terminology. **(b)**
Cross section of a typical coral reef system

Indeed, fore reef is the first region of interaction between ocean waves and the complex barrier-
reef morphology, where wavelength is reduced up to be comparable to local water depth, h.
Therefore, barrier reef works like a low-pass wave height filter, where h is the cut-off frequency
that restricts the maximum wave height allowed to pass and forces incoming waves to dissipate
some of their energy to maintain a constant energy flux [13]. As stated in [13], wave breaking
occurs when wave heights become some critical fraction of water depth, $H_{rms} < \beta h$, where

H_{rms} is the root-mean squared (RMS) wave height and β is a critical breaking parameter. When H_{rms}/h ratio is lower than β, waves pass onto the reef flat and propagate into lagoon area. This wave breaking relation provides a surf zone region where an important part of wave energy is dissipated by depth-limited breaking. Wave breaking is the predominant wave energy dissipation mechanism on sandy beaches unlike coral reefs, where dissipation due to bottom friction is also strong. Hence, only frictional dissipation factors are estimated in the study site. Results are shown in Section 5.4.3.

A number of empirical and semi-empirical models have been proposed to predict wave energy dissipation rate due to bottom friction in coral reefs, porous media and submerged canopies. These models are formulated considering the integral form of the conservation of mechanical energy equation [235]. However, most methodologies consider monochromatic waves to determine energy dissipation factor.

Dalrymple *et al.* [236] proposed the pioneer approach to modelling wave energy dissipation on an idealized canopy formed by a cluster of cylinders. This model predicts wave friction factor as a function of the canopy geometry without considering wave conditions. Nielsen [12] developed an empirical formulation to estimate the wave friction factor by fitting laboratory data from monochromatic wave-driven flows, where bottom roughness was known and controlled. However, this approach is not in accordance with propagation of coastal waves in coral reefs, where superposition of individual random wave components often occurs when they pass onto a reef flat. Hence, Madsen *et al.* [14], [15] extended the monochromatic Nielsen's formulation to spectral wave conditions, which are much closer to random nature of coastal waves.

Madsen *et al.* [14], [15] defined representative flow parameters as a weighted average of spectral components that assigns more weight on the components that have higher wave energy. Considering the above models, Figure 5.3 summaries the spectral procedure used for the wave energy dissipation analysis in this Chapter.

Frictional dissipation analysis considers an array of transects oriented in the cross-reef direction, perpendicular to the detected shoreline. Chapter 6 gives more detailed information about the shoreline detection algorithm. Firstly, wave parameters significant wave height H_s, peak period T_p and peak wavelength λ_p are estimated from sea clutter radar data. The peak wavenumber k_p is determined by solving the linear dispersion relation for a given water depth h at each transect point. Then, we apply FFT on radar-derived sea surface elevation data to convert time series into frequency domain for spectral wave conditions. Empirically, the first seven frequency components of the wave amplitude spectrum that contain more energy are selected to estimate wave friction coefficients and the equivalent bottom roughness factor. Hence, continuous wave spectrum is described by $N = 7$ discrete frequency components of sub-index j. Afterwards, the maximum near-bottom horizontal orbital velocity $u_{b,j}$ is determined by applying linear wave theory as [13],

$$u_{b,j} = \frac{a_j \omega_j}{\sinh k_j h} \tag{5.1}$$

where a_j and k_j denote wave amplitude and wavenumber of the jth frequency component that can be obtained as,

Field Measurements
Raw-radar, in-situ data and water depth h

Pre-processing
Gauss and Gabor Filtering
Wave propagation direction θ_p

3D-IFFT Procedure
Scaled $\eta(r_0, t)$

Welch PSD Method
Sea state parameters H_s, T_p
Wave energy spectrum $S(f)$

Frictional Dissipation Parameters
• $f_{e,r}$ energy dissipation factor
• $f_{w,r}$ wave friction factor
• k_w equivalent bottom roughness

FFT of $\eta(r_0, t)$
$j = 1, 2, ...N$ frequency components with higher energy

Initial Spectral Parameters
For each transect, f_j and a given h, we have $S(f_j)$, a_j, ω_j and k_j
1. Compute F_j, E_j and $C_{g,j}$
2. Compute $u_{b,j}$ and RMS values $u_{b,r}$, ω_r
3. Find $\epsilon_{f,j} = \Delta F_j / \Delta x \cos\theta$
4. Compute $f_{e,j}$ and RMS value $f_{e,r}$

Iterative Spectral Procedure
1. Assume $\phi_r = 33°$ and $k_{w,j_0} = u_{b,r}/\omega_r$
2. Find $f_{w,r} = f_{e,r}/\cos(\phi_r)$
3. Obtain k_{w,j_i} from Nielsen (1992) or Madsen (1994)
4. Verify tolerance, $tol = |k_{w,j_i} - k_{w,j_{i-1}}|$
5. If $tol > 10^{-6}$, $\phi_r = 33° - 6\log_{10}\left(u_{b,r}/k_{w,j_i}\omega_r\right)$, Repeat 2-4.
6. If $tol \leq 10^{-6}$, $k_{w,j_i} = k_{w,j_i}$

Figure 5.3: Block diagram of the spectral wave energy dissipation procedure by coral reefs and submerged canopies.

$$a_j = \sqrt{2S_j \Delta f_b} \tag{5.2}$$

where S_j is the jth component of the wave energy spectral density S, which is obtained by overlapping Hamming windows of equal size over sea surface elevation time series according to Welch algorithm. Indeed, Δf_b, $1/64$ in this case, represents the bandwidth of the considered Hamming windows. Then, the representative maximum near-bed horizontal orbital velocity, $u_{b,r}$, and the representative wave radian frequency, ω_r, can be determined by [13],

$$u_{b,r} = \sqrt{\sum_{j=1}^{N} u_{b,j}^2} \tag{5.3}$$

$$\omega_r = \frac{\sum_{j=1}^{N} \omega_j u_{b,j}^2}{\sum_{j=1}^{N} u_{b,j}^2} \tag{5.4}$$

Considering that all frequency components propagate in the same wave direction x, the one-dimensional wave energy equation is [13],

$$\frac{\delta F_j}{\delta x} = -\epsilon_{b,j} - \epsilon_{f,j} \tag{5.5}$$

where $\epsilon_{b,j}$ and $\epsilon_{f,j}$ are the energy dissipation rate due to wave breaking and bottom friction, respectively [235]. F_j is the wave energy flux defined as [13],

$$F_j = E_j C_{g,j} \tag{5.6}$$

where E_j denotes the wave energy density and $C_{g,j}$ represents the group velocity, which can be defined by applying linear wave theory as [13],

$$E_j = \frac{1}{2} \rho g a_j^2 \tag{5.7}$$

where ρ is the seawater density and

$$C_{g,j} = \frac{1}{2} \left(1 + \frac{2 k_j h}{\sinh 2 k_j h} \right) \frac{\omega_j}{k_j} \tag{5.8}$$

where k_j, ω_j and a_j are the wavenumber, angular wave frequency and wave amplitude for each jth frequency component, respectively.

Regarding wave dissipation, ϵ_{total} is the total wave dissipation rate that considers the resulting effect of both breaking (ϵ_b) and frictional (ϵ_f) dissipation mechanisms. It is given by [13],

$$\epsilon_{total} = \sum_{j=1}^{N} \epsilon_{total,j} = \sum_{j=1}^{N} \epsilon_{b,j} + \epsilon_{f,j}. \tag{5.9}$$

Since lagoon in the study area has a rough bottom surface, mild bottom slopes and less wave breaking behind the reef barrier, wave energy dissipation is assumed to be mainly caused by frictional dissipation [235]. Therefore, ϵ_{total} is approximately equivalent to ϵ_f [13],

$$\epsilon_{total} \approx \epsilon_f = \frac{\Delta F}{\Delta x \cos \theta} \tag{5.10}$$

where Δx is the distance between two arbitrary adjacent points A and B inside the lagoon and θ is the angle formed between the line connecting A and B and the wave propagation direction in this zone [235].

An alternative procedure to find ϵ_f considers the representative wave parameters $u_{b,r}$ and ω_r, Equations (5.3) and (5.4), respectively. Therefore, ϵ_f can be defined as [13],

$$\epsilon_f = \sum_{j=1}^{N} \epsilon_{f,j} = \frac{1}{4}\rho \sum_{j=1}^{N} f_{e,j} u_{b,r} u_{b,j}^2 \tag{5.11}$$

where $f_{e,j}$ is the jth component of the energy dissipation factor f_e, which can be described as a function of the *wave friction factor*, $f_{w,j}$, by [13],

$$f_{e,j} = \sqrt{f_{w,r}} \sqrt{f_{w,j}} \cos \phi_j \tag{5.12}$$

where $f_{w,r}$ and $f_{w,j}$ are the representative and the jth component of the wave friction factor, respectively. Besides, ϕ_j is the angle between the bottom shear stress τ_w and the near-bed horizontal orbital velocity u_b. Hence, the representative dissipation factor, $f_{e,r}$, can be determined by using the weighted average approach as [13],

$$f_{e,r} = \frac{\sum\limits_{j=1}^{N} f_{e,j} u_{b,j}^2}{\sum\limits_{j=1}^{N} u_{b,j}^2} \tag{5.13}$$

giving a single value for the energy dissipation factor that represents the contributions of the different wave frequency components in spectral conditions.

According to Nielsen [12], [13] and Madsen *et al.* [14], [15] approaches, equivalent bottom roughness, k_w, can be determined as a function of the wave friction factor, f_w. Wave friction factor f_w is parametrized as a ratio of the near-bed horizontal wave orbital excursion amplitude $A_b = u_b/\omega$ and k_w. As a general formula for both methodologies [15],

$$f_{w,j} = \exp\left[a_1 \left(\frac{C_\mu u_{b,r}}{k_w \omega_j}\right)^{a_2} + a_3\right] \tag{5.14}$$

where a_1, a_2 and a_3 are empirical coefficients. In Nielsen's formula [12], [13], $a_1 = 5.5$, $a_2 = -0.2$ and $a_3 = -6.3$. Madsen *et al.* [14], [15] stated that these coefficients correspond to $a_1 = 7.2$, $a_2 = -0.078$ and $a_3 = -8.82$, respectively. C_μ is an empirical coefficient, which is defined in the range of $0.2 < C_\mu u_{b,r}/k_w \omega_j < 10^2$ according to the strength of wave-current flows. This Chapter

uses both formulations to describe frictional energy dissipation. In this case, $(C_\mu = 1)$ because wave-current interaction is neglected.

According to Equation 5.12, the phase angle ϕ_r is required to estimate the representative wave friction factor $f_{w,r}$ for a given energy dissipation factor $f_{e,r}$. Therefore, the phase angle ϕ_j in degrees for each jth frequency component can be determined by [13],

$$\phi_j = 33 - 6.0 \log_{10} \left(\frac{u_{b,r}}{k_w \omega_j} \right) \tag{5.15}$$

where the representative phase lag, ϕ_r, is obtained by substituting ω_j for ω_r. Finally, $f_{w,r}$ is calculated as [13],

$$f_{e,r} = f_{w,r} \cos \phi_r \tag{5.16}$$

As shown in Figure 5.3, ϕ_r is estimated through an iterative procedure which assumes $\phi_{r_0} = 33°$ as the initial value. On the first iteration, $i = 1$, the representative dissipation factor $f_{e,r}$ is expressed as a function of the representative wave friction factor $f_{w,r}$ using Equation (5.16) and considering an initial value defined by Equation (5.13). Bottom equivalent roughness, k_w, is estimated using Madsen's *et al.* and Nielsen's coefficients, as defined in Equation (5.14). Finally, a new value of ϕ_r is obtained for a given k_w which is updated until the new value of k_w does not exceed the minimum difference of 10^{-6}. A list of symbols used in the spectral wave energy dissipation analysis is given in the Table of Symbols of this doctoral dissertation.

5.4 Results

5.4.1 Reef Morphology

In this section, reef morphology of the study site is evaluated through raw-intensities and surrounding wavefields detected by the marine radar in the barrier-reef lagoon system. Figure 5.4 indicates the approximate position for the fore reef (seaward from the reef rim at $x = 0$), reef flat (reef crest or rim) and lagoon (between the beach and the reef flat), which are identified by visual inspection. As it can be observed, ocean waves move shoreward from deep waters to coral barrier-reef system from NE, whose wave propagation direction θ is mainly dominated by fetch. In this offshore area, waves can be described by linear wave theory. Then, depth-limited wave breaking occurs when waves pass onto reef flat forming the irregular wavefield inside lagoon, as shown in Figure 5.4, due to wave transformation processes (e.g. breaking and diffraction).

It is worth to note that not only reef morphology and wavefields are observed in the total coverage area of the radar system. As shown in Figure 5.4, Johnny Cay and a sand beach section can be also detected through the discrimination of large shaded areas with low intensity. Applying digital image processing and first-order derivative filters, the magnitude of the image gradient is computed and therefore shoreline and coral reef barrier (i.e. reef rim) are delineated.

Results are depicted in Figure 5.5b for a normalized sea clutter image acquired at 15:00 UTC. Chapter 6 gives more detailed information about this methodology.
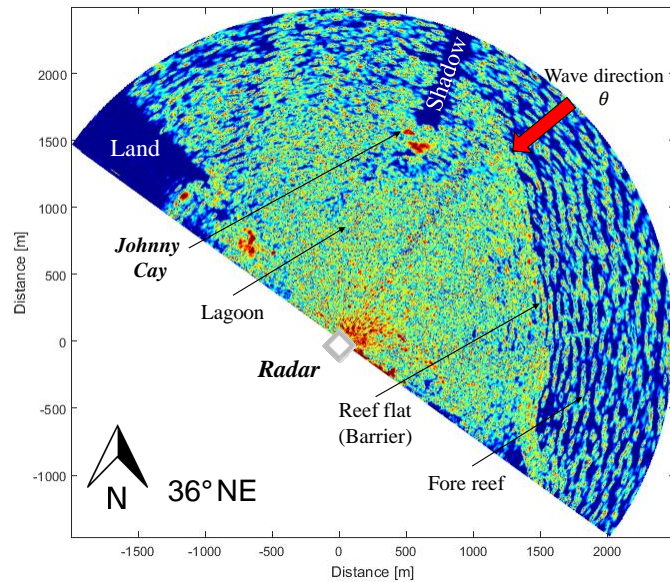
Figure 5.4: Reef morphology and surrounding wavefields detected by the X-Band marine radar in the coral reef system. Fore reef, reef flat and lagoon areas are identified by visual inspection. Johnny Cay and a sand beach section are also detected.
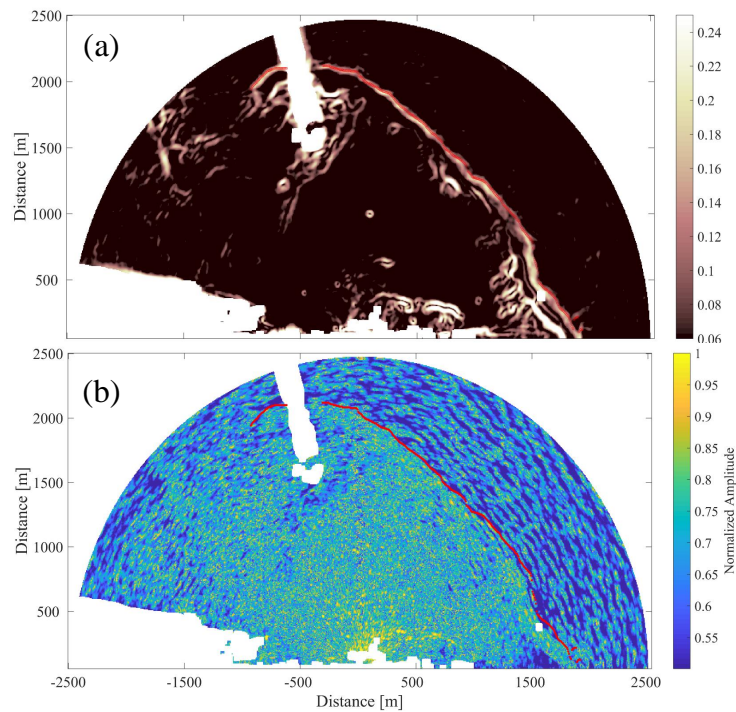
Figure 5.5: Reef rim detection using first-order derivative filters: **(a)** Magnitude of the image gradient. **(b)** Coral reef barrier (red line) detected at 15:00 UTC by using the variance image of sea clutter and normalized sea clutter intensities.

5.4.2 Radar-Measured Wave Parameters in a Barrier-Reef System

In order to verify the effectiveness of the marine radar to estimate sea state parameters in coral reefs, model-predicted significant wave height and radar-measured H_s data are compared at three different hours (12:00, 15:00 and 18:00 UTC). Figure 5.6 shows the model-predicted H_s wavefield at 15:00 UTC in the outer and the inner coral reef using the SWAN numerical model with a spatial resolution of 50 m, as mentioned in Section 3.4. As it can be seen, offshore wave conditions present a mean H_s of 2.08 m. However, H_s is reduced up to 0.25 m in the reef lagoon due to wave breaking and frictional energy dissipation.
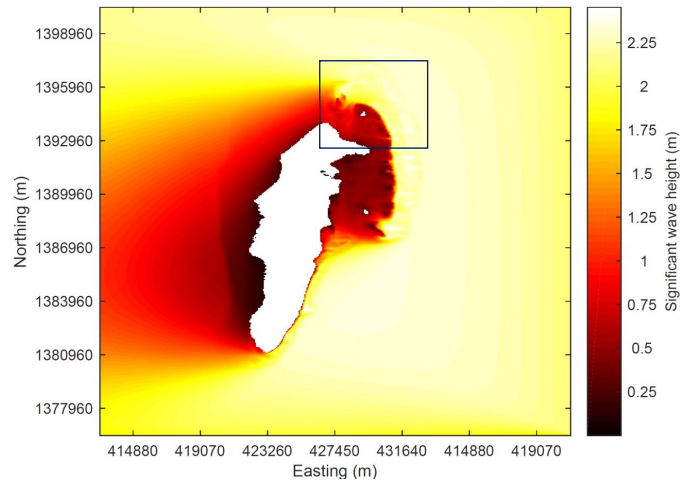
Figure 5.6: Model-predicted H_s wavefield at 15:00 UTC. Square indicates the study area.

Figure 5.7 presents the scatter plots between the radar-retrieved H_s and the model-predicted data in the fore reef and the lagoon regions. It can be observed that X-Band marine radar estimates are in good agreement with model-predicted H_s data in both reef regions with high correlation coefficients $r \geq 0.84$ and RMSE ≤ 0.24.

Tide-gauges data are also used for the assessment of radar estimates in the lagoon region. According to hourly in-situ measurements, $H_{s1} = 1.13$ m, $H_{s2} = 0.69$ m, $T_{p1} = 7.15$ s and $T_{p2} = 7.68$ s at 15:00 UTC, where sub-index denotes the data source instrument (i.e. H_{s1} is the significant wave height measured by tide-gauge #1). For tide-gauge #1, H_{s1} and T_{p1} show mean bias and relative errors of 0.089 m (9.34%) and 1.20 s (22.77%), respectively. In contrast, the estimation errors are 0.06 m (10.35%) and 0.32 s (7.04%) for H_{s2} and T_{p2} considering tide-gauge #2. Although both instruments were installed in the reef lagoon, tide-gauge #1 is closer to reef flat. Hence, local depth-limited wave breaking hinders data acquisition explaining the large errors for T_{p1}.

Besides, an alternative unsupervised classification procedure to delineate the inner and the outer reef zones (i.e. lagoon and fore reef areas, respectively) is applied. The method considers H_s data retrieved from radar. From Figure 5.8a, the bi-modal distribution of H_s in the barrier-reef system allows the identification of two main zones with (1) mild and (2) rough wave conditions, which in turns represent the inner and the outer reef areas, respectively. Therefore, we define an
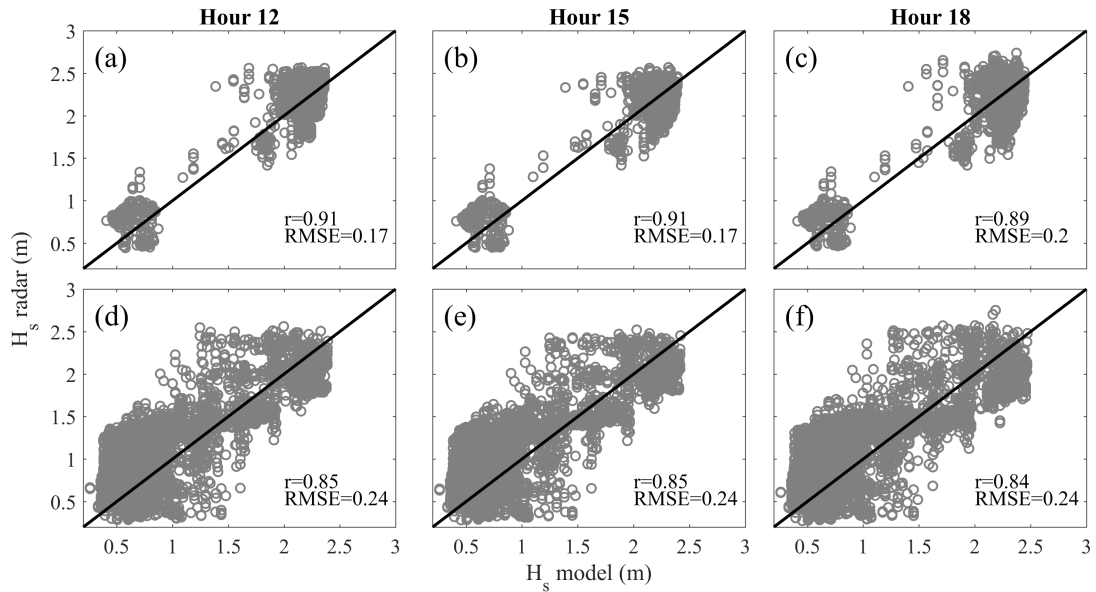
Figure 5.7: Scatter plots of H_s between radar-retrieved and model-predicted data in **(a)-(c)** the fore reef and **(d)-(f)** the lagoon. Wave data were collected at 12:00, 15:00 and 18:00 UTC.
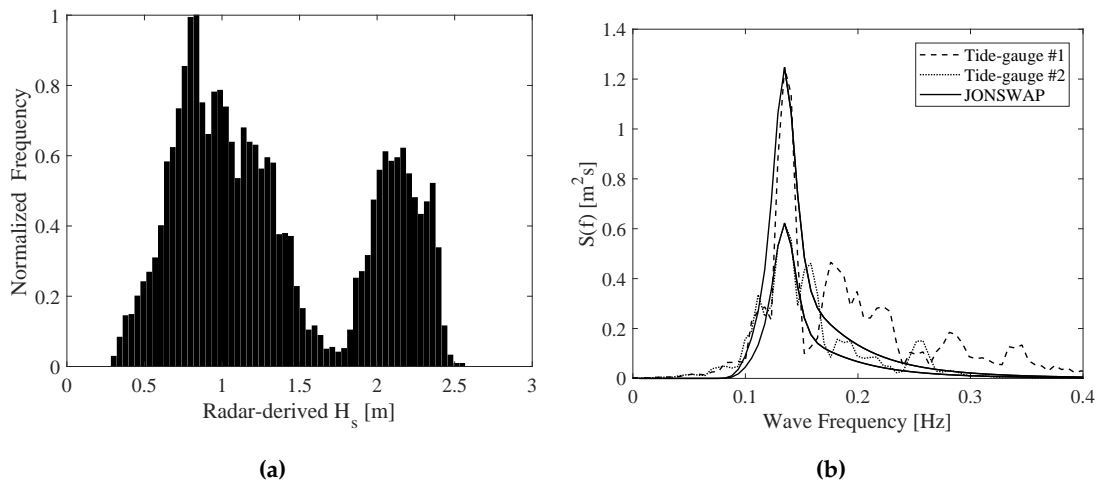
Figure 5.8: Assessment of wave conditions in the barrier-reef system. An unsupervised classification procedure is defined to delineate the inner and the outer reef zones by using **(a)** the mean normalized histogram of radar-retrieved H_s data and **(b)** the wave energy spectra from two tide-gauges located in the shallow coral reef lagoon.

empirical H_s threshold by computing the normalized histogram from mean radar-retrieved H_s data to decide where each pixel is located. According to Figure 5.8a, the empirical threshold is $H_s = 1.8$ m considering the average wave conditions during the field measurement campaign.

Regarding in-situ data, Figure 5.8b illustrates the comparison of wave frequency spectra from tide-gauges data and the semi-empirical JONSWAP spectrum at 15:00 UTC. As stated above, stronger waves and highly spread wave energy spectrum for tide-gauge #1 suggest that the instrument is closer to non-linear wave breaking processes in the fore reef.

5.4.3 Spectral Wave Dissipation Analysis

Nielsen [12], [13] and Madsen *et al.* [14], [15] approaches are tested using remotely sensed radar data to determine frictional dissipation in the shallow coral reef lagoon. Since these methods originally consider wave and currents data from an array of in-situ sensors installed in a cross-reef direction, 210 transects perpendicular to the detected shoreline are analyzed to measure the energy dissipation rate. Therefore, each pixel of the radar image is considered as a single virtual sensor which provides wave data from the sea surface as demonstrated in Chapter 4.

Figure 5.9 shows the radar-retrieved and model-predicted H_s data in a cross-reef transect at 12 m away from the radar antenna (transect #104, black dashed line in Figure 5.9a). According to Figure 5.9b, ocean waves move shoreward from the fore reef ($-500 < x < 0$ m) with a mean significant wave height of $H_{s0} = 2.1$ m. Then, waves break when they pass onto reef rim at $x = 0$ and H_s is reduced with a steep slope due to wave breaking dissipation in the fore reef and the reef rim. Hence, fore reef combines effects of both wave breaking and bottom friction to dissipate wave energy of incoming waves. As it can be seen, H_s is about $H_{s0}/4$ in the lagoon due to bottom friction and wave breaking dissipation.
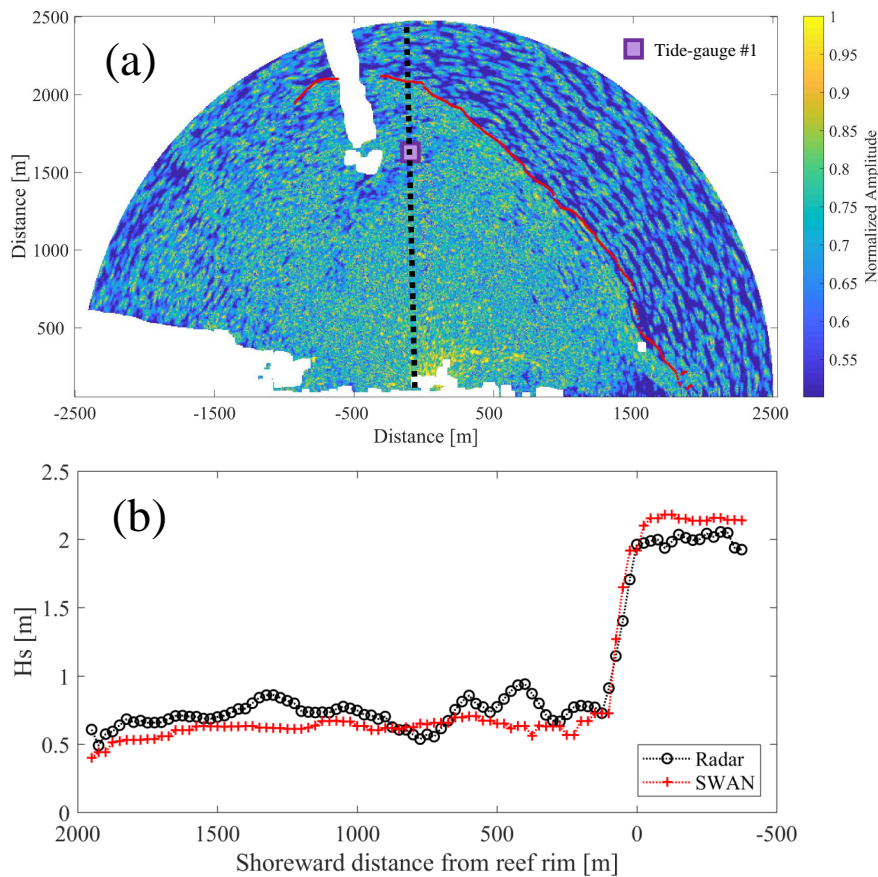
Figure 5.9: (a) Transect of virtual instruments in cross-reef direction at 12 m away from the radar antenna (transect #104, black dashed line). The transect considers tide-gauge #1 position. **(b)** Radar-retrieved and model-predicted H_s data throughout the transect #104; $x = 0$ corresponds to reef rim.

In order to analyze the frictional dissipation in transect #104, wave friction factor k_w and the equivalent bottom roughness k_w are determined using Nielsen's [12], [13] and Madsen's *et al.* [14], [15] coefficients. Results are shown in Figure 5.10. Water depth is highly irregular along this transect. As expected, both k_w and f_{wr} reach their higher values in shallower water depths, e.g. $1.9 < x < 2$ km and $1.15 < x < 1$ km from the reef rim. That means these shallower areas strongly contribute to wave energy dissipation due to bottom friction. Besides, k_w and f_{wr} drop with a steep slope at $x = 0$ which indicates the reef rim location in this transect. Note that $f_{wr,Nielsen}$ and $f_{wr,Madsen}$ are in good agreement. However, the equivalent bottom roughness values obtained from Nielsen's model are often higher than Madsen's *et al.* estimation.
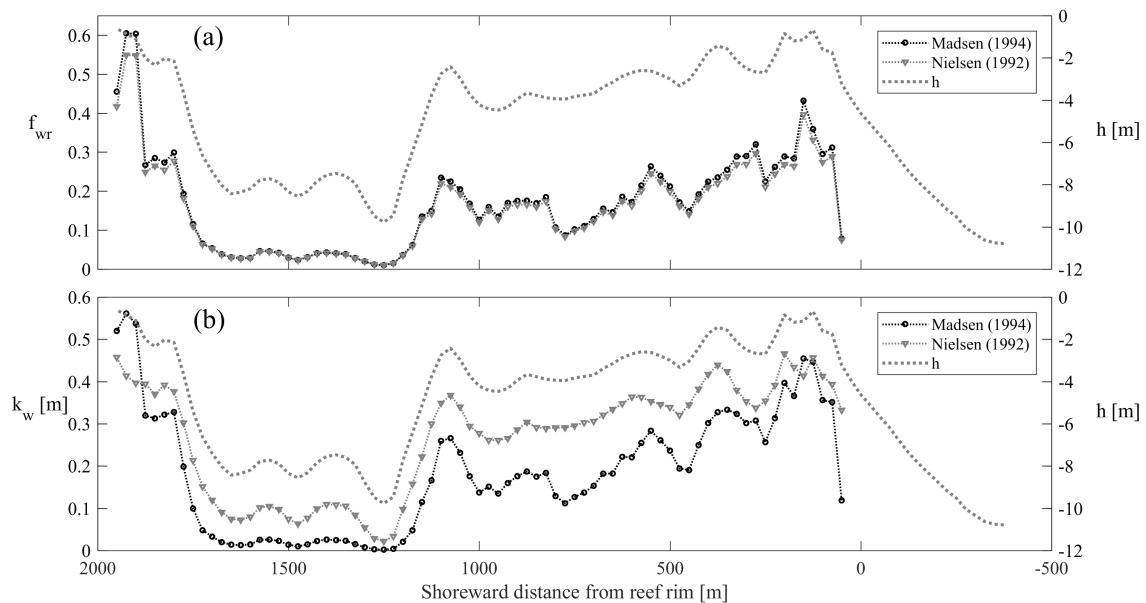
Figure 5.10: (a) Wave friction factor f_{wr} and **(b)** the equivalent bottom roughness k_w in transect #104 by applying Nielsen's [12], [13] and Madsen's *et al.* [14], [15] coefficients; h represents the local water depth.

Results in Figure 5.10 reveal that wave friction factor f_{wr} and the equivalent bottom roughness k_w are strongly correlated with water depth h but they cannot be described as a function of the incident significant wave height height due to non-linear amplitude effects. Besides, frictional dissipation in reef flats is strong because they are one of the shallowest and roughest regions in coral reef systems.

To further verify the performance of both methodologies using remotely sensed radar data, Figure 5.11a and 5.11b depict mean values of k_w and f_{wr} in the coral reef lagoon, respectively. Note that only the lagoon region where water depth data are available will be considered. Black and red lines delineate the detected shoreline and reef rim, respectively. Again, k_w obtained from Nielsen's model is about twice the equivalent bottom roughness estimated using Madsen's *et al.* coefficients, mainly in shallower depths.

Total average value and mean standard deviation (σ) of the wave friction factors f_{wr} in Figure 5.11 considering Nielsen's [12], [13] and Madsen's *et al.* [14], [15] empirical coefficients are 0.167 ($\sigma = 0.136$) and 0.18 ($\sigma = 0.15$), respectively. Similarly, mean results for the equivalent bottom

(a)

(b)
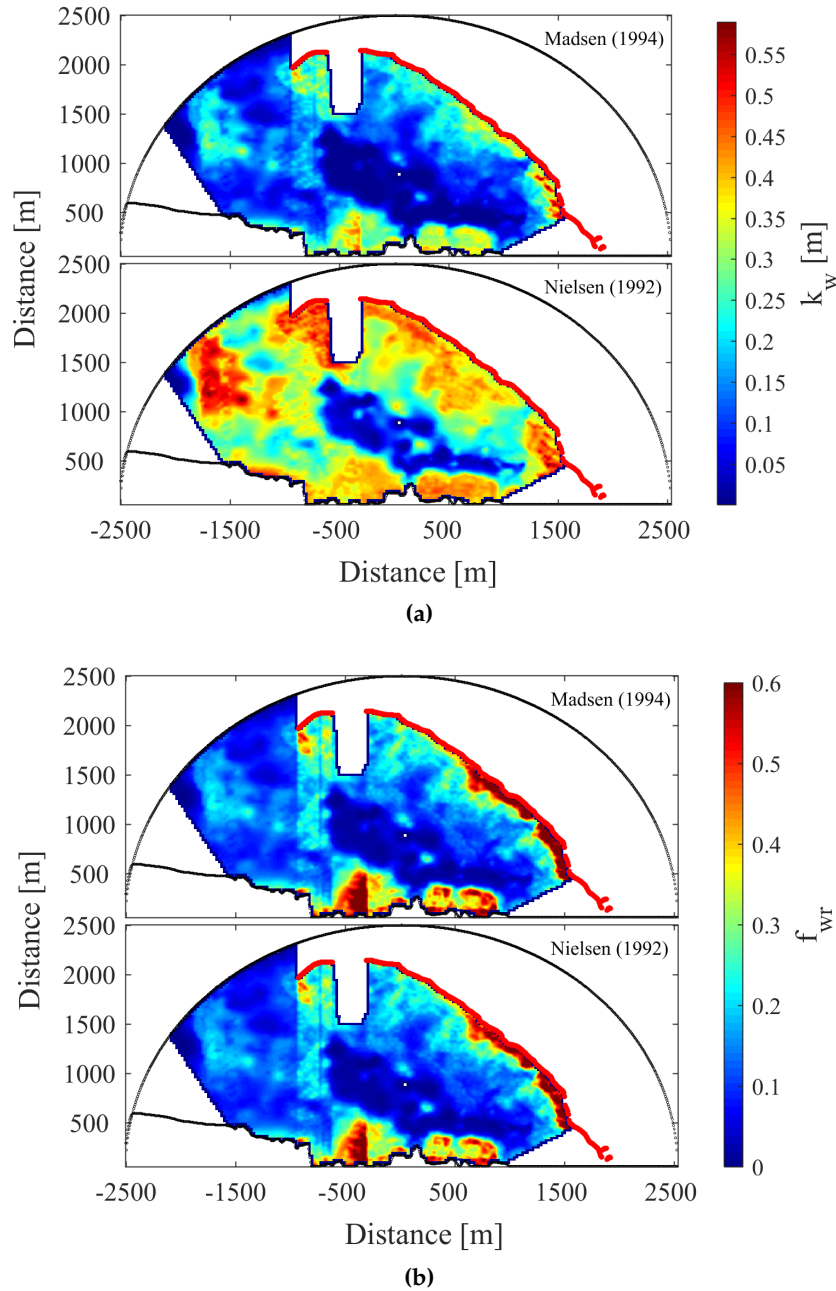
Figure 5.11: Mean values of **(a)** k_w and **(b)** f_{wr} in the coral reef lagoon using Nielsen's [12], [13] and Madsen's *et al.* [14], [15] coefficients. Black and red lines delineate the detected shoreline and reef rim, respectively.

roughness k_w are 0.30 m ($\sigma = 0.12$ m) and 0.20 m ($\sigma = 0.14$ m) using Nielsen and Madsen *et al.* approaches, respectively.

Indeed, mean values of f_{wr} and k_w are in good agreement with the values calculated by Lowe *et al.* in [13] for each pair of in-situ pressure sensors aligned in a cross-reef direction transect on the barrier reef in Kaneohe Bay, Hawaii ($f_{wr} = 0.28$ and $k_w = 0.16$ m, according to [13]). Besides, mean k_w obtained in San Andres Island is comparable to $k_w = 0.4$ m calculated for meadow canopies in Cala Millor beach, Spain [197], [237].

5.5   Discussion

Considering the mean values of k_w and f_{wr} obtained from both Nielsen's [12], [13] and Madsen's *et al.* [14], [15] empirical coefficients in the coral reef lagoon (See Figure 5.11), the mean bias error is calculated to give a quantitative comparison of both techniques and thereby measure their agreement. Results are depicted in Figure 5.12. For the equivalent bottom roughness k_w, this performance statistic is calculated as $k_{w,Nielsen} - k_{w,Madsen}$. Similarly, mean bias of f_{wr} estimates is determined by $f_{wr,Nielsen} - f_{wr,Madsen}$.

In general, the correlation coefficients between both formulations are 0.806 and 0.99 for k_w and f_{wr}, respectively. Besides, the root mean square errors (RMSE) for k_w and f_{wr} are 0.01 and 0.09, respectively, by comparing both approaches and considering all k_w and f_{wr} estimated in the lagoon. However, Nielsen's coefficients slightly overestimate k_w in most of the tested locations, as shown in Figure 5.12a. Therefore, a total mean bias, $\overline{\text{Bias}}$ is calculated to determine the general agreement between Nielsen's and Madsen's *et al.* estimates. For the equivalent bottom roughness k_w, it is given by,

$$\overline{\text{Bias}} = \frac{1}{M} \sum_{j=1}^{M} k_{w,Nielsen} - k_{w,Madsen} \tag{5.17}$$

where M is the number of locations where k_w is determined. Total mean bias and the corresponding relative errors are 0.102 m (12.99%) and -0.012 (0.05%) for k_w and f_{wr}, respectively. The highest mean bias errors for k_w and f_{wr} are 0.33 m and -0.1, respectively.
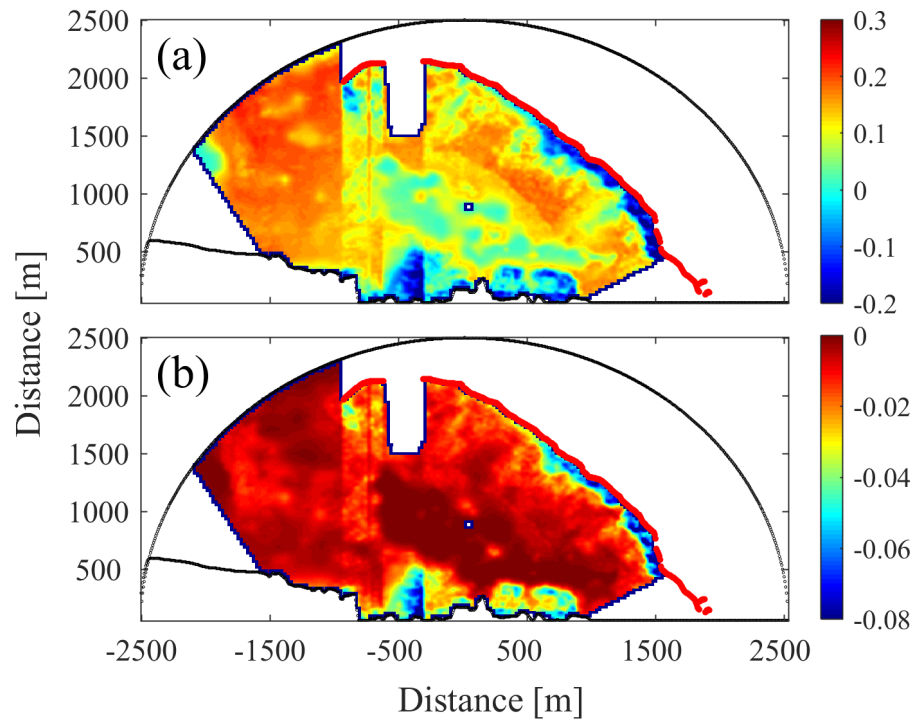
Figure 5.12: Mean bias error of **(a)** k_w and **(b)** f_{wr} between Nielsen's [12], [13] and Madsen's *et al.* [14], [15] models by using remotely sensed radar data.

Since Nielsen's coefficients estimate the wave friction factor by fitting laboratory data from monochromatic wave-driven flows and fixed three-dimensional roughness, it may be questionable to apply Nielsen's formula in the rough lagoon. In contrast, Madsen's *et al.* spectral wave model can be applied to a relative roughness range of $0.2 < C_\mu u_{b,r}/k_w \omega_j < 10^2$, where spectral wave conditions are much closer to random nature of coastal waves. Therefore, Madsen *et al.* approach adequately estimate k_w.

As Lowe *et al.* stated in [13], the equivalent bottom roughness, also named the equivalent Nikuradse roughness, can be determined by $k_{w,Nielsen} \simeq 4\sigma_b$, where σ_b is the standard deviation of the measured bed elevation. σ_b was obtained in [13] by using a roughness profiler which measured the height of the roughness every 5 cm in a cross-reef transect of 3 m with a vertical resolution of ± 2 mm. Similarly, Madsen *et al.* [14], [15] reported $k_{w,Madsen} \simeq 4H_{bed}$, where H_{bed} is the height of the bottom roughness elements, i.e. the mean height of the coral elements. Figures 5.13a and 5.13b depict the estimated H_{bed} and σ_b obtained from $k_{w,Madsen}$ and $k_{w,Nielsen}$, respectively.

As it can be observed in Figure 5.13, mean H_{bed} and σ_b are 5 cm and 7.66 cm, respectively. These values are in good agreement with the geometric parameters proposed by Lesser *et al.* [238], Reindenbach *et al.* [239] and Marshall [240] to model in-canopy flows for branched species, such as *Stylophora* and *Pocillopora* (Table 4 in [218]), which are also common in the San Andres Island's coral carpets [199]. Moreover, the highest $H_{bed} = 0.25$ m and $\sigma_b = 0.17$ m are comparable to values obtained by Huang *et al.* [215] in Lady Elliot Island (the Great Barrier Reef, Australia), where $H_{bed} = 0.272$ m and $\sigma_b = 0.14$ m.
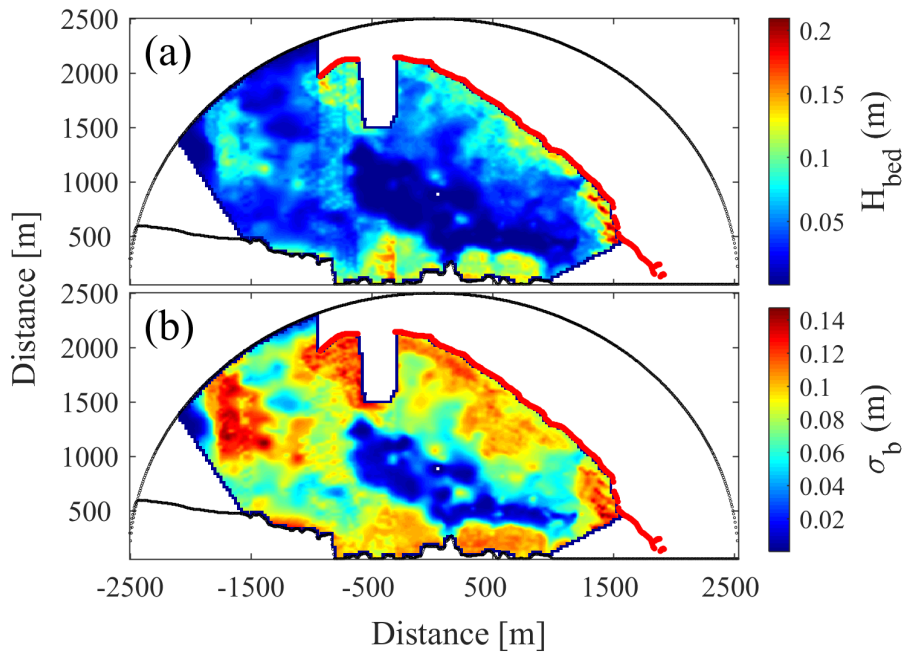
Figure 5.13: (a) Height of the bottom roughness elements H_{bed} and **(b)** the standard deviation of the bed elevation σ_b estimated in the shallow coral reef lagoon using remotely sensed radar data.

5.6   Summary

This Chapter introduces a completely novel use for X-Band radars by remotely sensing wave energy dissipation rates, wave friction factors and the equivalent bottom roughness in the San Andres Island barrier-reef system. Until now, wave energy dissipation had been extensively studied by deploying a line of in-situ sensors (e.g. ADVs and ADCPs) in a cross-reef direction, perpendicular to the coastline. Due to radar estimates are in good agreement with model-predicted H_s data and in-situ measurements, results reveal that X-Band marine radars can describe prominent features of coral reefs, including the delineation of reef morphological structure, wave energy dissipation and wave transformation processes in the lagoon.

Considering raw-radar intensities, the fore reef, reef flat and lagoon regions can be identified by visual inspection. However, an alternative unsupervised classification procedure to delineate the inner and the outer reef zones (i.e. lagoon and fore reef areas, respectively) is applied. This method uses an empirical threshold ($H_s = 1.8$ m) derived from the bi-modal distribution of radar-measured H_s, where two main zones with mild and rough wave conditions are identified. These zones in turn represent the inner and the outer reef areas, respectively. Johnny Cay and a sandy beach section are also detected through the discrimination of large shaded areas with low intensity. Shoreline and reef rim are delineated using the magnitude of the image gradient. Chapter 6 gives more detailed information about this methodology.

In order to determine frictional dissipation in the reef lagoon, Nielsen [12], [13] and Madsen *et al.* [14], [15] approaches are tested considering each pixel of the radar image as a single virtual sensor. Correlation coefficients between both formulations are high (r_{k_w} =0.806 and $r_{f_{wr}}$ =0.99) with root mean squared differences of 0.01 and 0.09 for k_w and f_{wr}, respectively. However, Nielsen's coefficients slightly overestimate k_w in most of the tested locations because they were originally determined by fitting laboratory data from monochromatic waves over a fixed rough bottom. Therefore, Madsen's *et al.* spectral wave model adequately estimates k_w as 0.20 m.

It is worth to note that the reef attenuates incident waves by approximately 75% due to both frictional and wave breaking dissipation. According to results, mean values of $f_{wr,Madsen} = 0.18$ and $k_{w,Madsen} = 0.20$ m calculated in the study area are comparable with estimates obtained by Lowe *et al.* [13] in Kaneohe Bay, Hawaii ($f_{wr} = 0.28$ and $k_w = 0.16$ m) and Infantes *et al.* [197], [237] for meadow canopies in Cala Millor beach, Spain ($k_w = 0.4$ m), both using in-situ wave and currents data.

Finally, the standard deviation of the measured bed elevation σ_b and the height of the bottom roughness elements H_{bed}, i.e. the mean height of the coral elements, are estimated considering $k_{w,Nielsen} \simeq 4\sigma_b$ [13] and $k_{w,Madsen} \simeq 4H_{bed}$ [14], [15]. According to results, mean values of H_{bed} and σ_b are 5 cm and 7.66 cm, respectively. These values are in good agreement with the geometric parameters proposed by Lesser *et al.* [238], Reindenbach *et al.* [239] and Marshall [240] to model in-canopy flows for branched species, such as *Stylophora* and *Pocillopora* (Table 4 in [218]), which are also common in the coral carpets of San Andres Island [199]. Moreover, the highest values of $H_{bed} = 0.25$ m and $\sigma_b = 0.17$ m are comparable to values obtained by Huang *et al.* [215] in Lady Elliot Island (the Great Barrier Reef, Australia), where $H_{bed} = 0.272$ m and $\sigma_b = 0.14$ m.

For future studies, velocity measurements may improve the understanding of radar performance. However, results presented above suggest a new research line in the assessment of coral reefs threats by combining multiple data sources, i.e. marine radars, in-situ sensors and numerical modelling, to provide more detailed information that can be used for coastal management services.

Chapter 6

Coastal Morphodynamics Study Using X-Band Marine Radar Data

"Anyone who stops learning is old, whether at twenty or eighty. Anyone who keeps learning stays young. The greatest thing in life is to keep your mind young."

Henry Ford (1863 – 1947)

6.1 Introduction

Monitoring coastline evolution and bathymetry changes are crucial tasks to support coastal management services including the assessment of flooding risks, crescentic sand bar formations and beach erosion/accretion. Indeed, environmental boundary conditions, bottom coastal morphology and incoming waves significantly modify the wave climate in specific sites. Human overexploitation in a given coastal zone is one of the most common causes of decline of ecosystem stability that yields important morphological changes on beach structure. Since coastal dynamics is governed by a set of nonlinear processes, the nearshore study requires not only accurate modelling systems but also continuous measurements. Therefore, the coarser pixel resolution of satellite imagery and the expensive, time-consuming and spatially-limited LiDAR and sonar surveys often preclude the continuous morphological mapping of coastal areas. In this context, shore-based remote sensing technologies, such as stereo-video imagery and microwave X-Band radars, can be used to describe the coastal dynamics in detail.

This Chapter is devoted to determine morphological mapping facilities of X-Band radars which are compared with the performance of video systems reported in the literature and results previously obtained from SIRENA [145] and ULISES [148] video monitoring systems at the study sites. Therefore, this Chapter mainly discusses the second hypothesis of this doctoral dissertation: *Coastal morphodynamics estimates could improve by merging data from multiple low-cost sensors*.

The chapter is outlined as follow. Section 6.2 describes all datasets used for the morphological analysis at Castelldefels and Cala Millor beaches. Section 6.3 gives an extended explanation of the the proposed approaches to estimate water depth and to detect shoreline using X-Band radars. Subsection 6.3.1 outline the *uBathy* algorithm [16] which is based on *empirical orthogonal functions* (EOF) and Hilbert Transform, as a novel bathymetric inversion algorithm from video

imagery, which is adapted to radar data. The shoreline detection algorithm derived from radar data is stated in Subsection 6.3.2. Section 6.4 deals with the comparison of the radar-retrieved morphological estimates and the measurements provided by in-situ surveys at the study sites. A discussion is presented in Section 6.5 comparing radar performance with video estimates in nearshore areas. Finally, Section 6.6 summaries the Chapter.

6.2   Field Data

Field experiments were conducted at Castelldefels and Cala Millor beaches during March 14th-19th and October 22th-24th 2018, respectively, to describe the nearshore morphodynamics using X-Band radars. Indeed, Castelldefels dataset allows the evaluation of water depth mapping skills from marine radars in coastal areas, whereas the assessment of shoreline detection is performed through Cala Millor dataset. The radar antenna was deployed at 13 m above MSL at Castelldefels beach (41°15′54.440″ N, 1°59′50.628″ E) and at 46.7 m height in Cala Millor (39°35′46.849″ N, 3°22′59.164″ E). Figure 6.1 shows the instruments deployment at Cala Millor beach, where an AWAC sensor was installed at 17 m depth and 1.5 km away from radar antenna (39°35′32.5″ N, 3°23′59.1″ E).
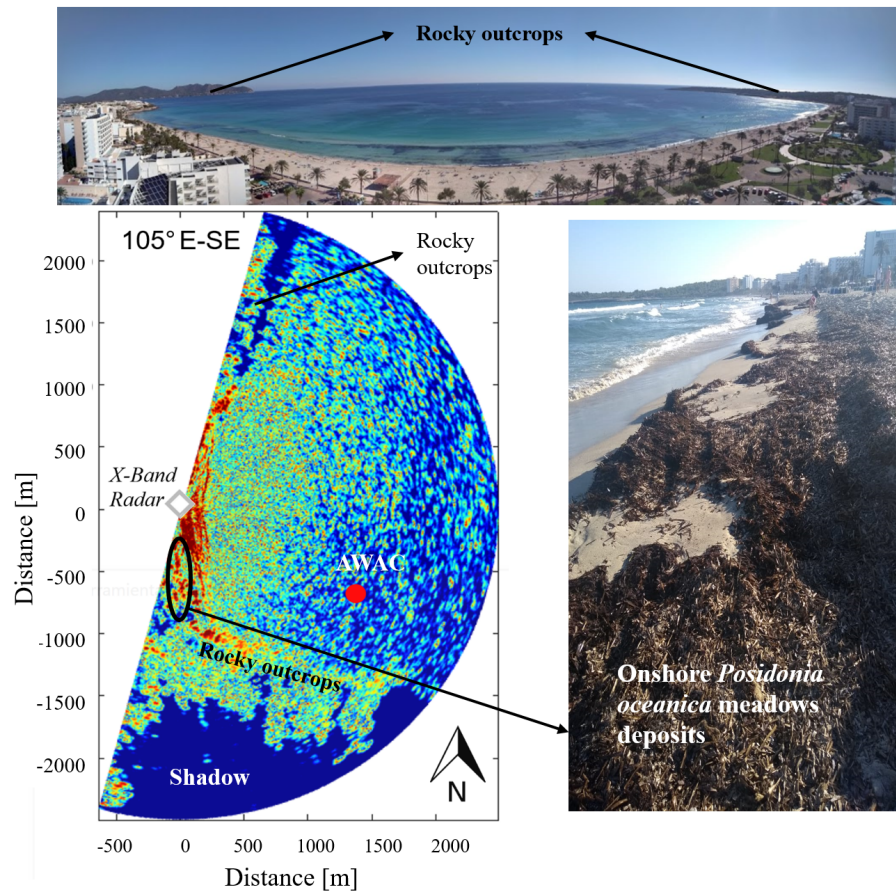
Figure 6.1: General layout of the marine radar and the in-situ sensor in Cala Millor. Onshore deposits of *Posidonia oceanica* meadows and surrounding rocky outcrops are identified in radar image.

As shown in Figure 6.1, the irregular and shaded areas correspond to radar backscatter from onshore deposits of *Posidonia oceanica* meadows and surrounding rocky outcrops. Since radar image seabed is colonized by the endemic *Posidonia oceanica* meadow, bottom roughness modifies wave propagation and dissipates energy due to bottom friction [197]. An extended analysis of wave energy dissipation in a coral reef coastal environment is given in Chapter 5.

The Coastal Ocean Observatory (`http://coo.icm.csic.es/`) from the Institute of Marine Science (ICM-CSIC) in Castelldefels has a set of 5 cameras located at 30 m height ($41°15'54.7''$ N, $1°59'29.1''$ E), and at about 500 m from the radar antenna location. In Cala Millor, the Marine-Terrestrial Beach Monitoring Facility (`http://www.socib.eu/`) from the Balearic Islands Coastal Observing and Forecasting System (SOCIB) also deployed 5 unattended video cameras located at $39°35'46.9''$ N, $3°22'59.33''$ E in the rooftop of the *SENTIDO Castell de Mar* hotel, i.e. at 6 m from the radar system location.

Topographic profiles and bathymetric surveys were carried out at both beaches to describe the nearshore morphological variations. Water depth survey at Castelldefels beach has dimensions of 1500 m $\times$ 1750 m (i.e. alongshore and cross-shore distances, respectively) from 1 m depth until 22 m depth. In contrast, topographic measured data in Cala Millor is extended up to about 13 m depth in a region of 1880 m $\times$ 720 m.

Besides, a differential GPS-RTK with submetrical resolution was used to measure shoreline data and submerged water depth profilers in both study sites. Figure 6.2c presents the measured shoreline on a planview *timex* image from SIRENA system in Castelldefels (14th March 2018) [125]. More detailed explanation is given in Chapter 3.

Figures 6.2a and 6.2b depict locations of remote sensors and water depth in-situ surveys in both study areas, i.e. Castelldefels and Cala Millor. Red squares and black diamonds markers indicate locations of video cameras and radar system, respectively. Red dotted line in Figure 6.2a delineates a cross-shore bathymetric transect measured during MUSAFELS experiment, whereas black dashed square outlines the radar analysis region in Castelldefels.

6.3 Methods

6.3.1 Bathymetric Inversion Algorithm from Video Imagery (*uBathy*)

The *uBathy* algorithm [16] is a novel approach to estimate water depth from stereo-video imagery that applies Principal Component Analysis (PCA) on the Hilbert Transform of the video images. Wave frequency ω and wavenumber k are determined by algebraic decomposition of the retrieved wave patterns from the spatio-temporal complex EOF-PCA analysis. For a given snapshot video image X in a spatio-temporal domain, i.e. $X_{mn} = f(x_m, t_n)$, with $m = 1, 2, .., M$ and $n = 1, 2, .., N$, each X_{mn} value can be obtained by [16],

$$X_{mn} = \overline{f_m} + \sum_{q=1}^{Q} \text{EOF}_q(x_m)\text{PC}_q(t_n) \tag{6.1}$$
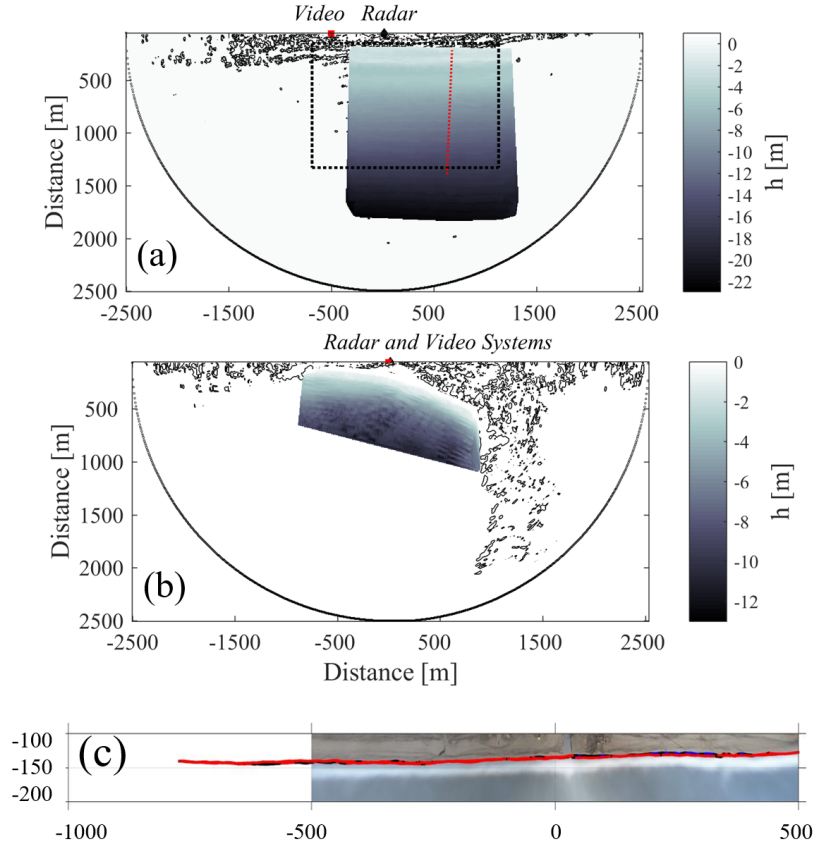
Figure 6.2: Remote sensors deployment and in-situ measured water depth data at **(a)** Castelldefels beach and **(b)** Cala Millor beach. Red squares and black diamonds indicate locations of video cameras and radar system, respectively. Red dotted line in **(a)** delineates a cross-shore bathymetric transect measured during MUSAFELS experiment. Black dashed square outlines the radar analysis region at Castelldefels beach. **(c)** Measured shoreline using RTK data on a planview *timex* image from SIRENA system in Castelldefels (March 14th 2018).

where $\overline{f_m}$ is the time average space-vector, EOF_q is the qth empirical orthogonal complex-valued vector in space and PC_q is the qth orthogonal complex-valued vector in time domain. Note that each pair $\{\text{EOF}_q, \text{PC}_q\}$ is a *mode*, whose contribution to the total complex-valued signal is quantified by the explained variance, σ_q^2, i.e. a real value [16].

Considering the propagation of J different small-amplitude wave components onto a flat seabed described as [16],

$$f = \sum_{j=1}^{J} a_j \cos(\mathbf{k}_j \cdot x - \omega_j t + \varphi_j) \tag{6.2}$$

where a_j is the amplitude and $\mathbf{k}_j = (k_{xj}, k_{yj})$ is the wavenumber vector of the jth wave component. Besides, ω_j and φ_j are the wave frequency and wave phase lag, respectively. This expression is an extended version of Equation 2.1 for sea surface elevation maps.

The Hilbert transform can be applied on wave patterns of X_{mn} to obtain the corresponding space-time discretized wave image that is given by [16],

$$X_{mn} = \sum_{j=1}^{J} a_j \exp(-i(\mathbf{k}_j \cdot x_m + \varphi_j)) \exp(i\omega_j t_n) \qquad (6.3)$$

where each jth component of the wave field can be determined as a *mode* of the PCA for large time domain. Therefore, ω_j and $k_j = |\mathbf{k_j}|$ are given by [16],

$$\alpha_t = \text{angle}\{PC(t)\} \approx \text{angle}\{\exp(i\omega_j t)\} = \omega_j t \qquad (6.4)$$

and

$$\alpha_x = \text{angle}\{EOF(x)\} \approx \text{angle}\{\exp(-i(\mathbf{k}_j \cdot x + \varphi_j))\} = -(\mathbf{k}_j \cdot x + \varphi_j) \qquad (6.5)$$

More detailed explanation about Hilbert transform is given in Appendix D.

The *uBathy* algorithm uses sub-videos obtained from a moving time window of width w_t, in which the dominant PC *mode* of each complex EOF is analyzed. Then, each time window t_i gives a $\{\omega_i, \sigma_{\omega i}\}$ pair by fitting α_t in a vicinity radius R_t to a polynomial function as $p_0 + p_1(t - t_0)$ at a certain time t_0. The ratio between the standard deviation $\sigma_{\omega i}$ and ω_i must be lower than 15% to select accurate ω_i values. Thus, wavenumber k can be obtained from each window t_i using the first EOF and the phase fitting procedure, as stated in [16] . Correlation coefficient of the fitted α_x has to be higher than 0.70 to properly recover k. Finally, local water depth is estimated fitting all pairs $\{\omega_i, k_i\}$ with the linear dispersion relation (Equation 2.5) on a neighborhood R_x. More detailed information about *uBathy* algorithm is given in [16] for synthetic wave trains and real field site video data.

The above methodology is adapted to radar systems considering more than 120 time windows with $w_t = 80$ s, $\triangle t = 10$ s, $\triangle x = 150$ m, $R_x = 250$ m and $R_t = 40$ s for each hourly sea clutter dataset during March 14th-19th 2018. Therefore, more than 35000 sub-videos were analysed with an average duration of the total video $t_{max} = 15$ minutes. Since more sub-videos are available, the windowing analysis will filter better the wave patterns, as stated in [16]. Hence, ω and k can be recovered from each radar sub-video with high accuracy.

According to Simarro *et al.* [16], the temporal parameters ($\triangle t$ and R_t) of the *uBathy* algorithm are defined considering $\triangle t \leq R_t \leq T/2$, where T is the wave period. Besides, the optimal spatial parameters must comply with the condition $\triangle x \leq R_x \leq \lambda/2$, where λ is the wavelength [16]. In contrast, $\triangle x \leq R_x \leq 6\lambda$ is considered for radar analysis, where λ ranged from ~ 25 m to ~ 65 m in this case. The condition for temporal parameters remains unchanged. Note that spatial parameters, i.e. $\triangle x$ and R_x, that optimize the bathymeric inversion using radar data are larger than those used for video imagery in [16], mainly due to the coarser spatial resolution of marine radars relative to video systems, i.e. $\triangle r_{radar} = 6$ m and $\triangle r_{video} = 0.16$ m [125].

Finally, the main *mode* for the PCA analysis of each time window must explain more than 80% of the total variance from the radar-retrieved wave patterns.

6.3.2   Proposed Shoreline Detection Approach

The proposed method for automatic extraction of the shoreline applies digital image processing techniques and first-order derivative filters on remotely sensed radar data. Basic steps include enhancement, smoothing and edge extraction of the radar images, as shown in Figure 6.3. Enhancement and smoothing procedures use both non-linear Gaussian filtering and morphological filters to intensify the edge discontinuities in the image intensity. Therefore, impulse noise in the image is suppressed while the edges are preserved.
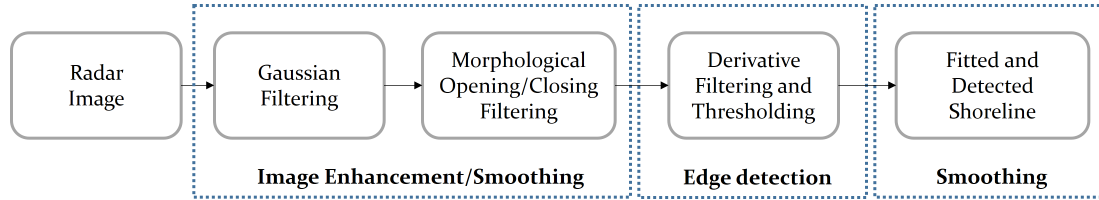
Figure 6.3: Shoreline detection procedure.

Considering each radar image as a spatial function $f(x, y)$ over a defined time t_i, the morphological operators, i.e. erosion and dilatation, and their combinations, i.e. opening and closing, can be used to describe curves and mixed texture of shorelines [241]. The erosion of an image by a moving window W, also known as structuring element, is given by $f \ominus W$ and describes the infimum backward-shifted versions of f in all points of the neighborhood of size W. In contrast, the dilatation of an image, $f \oplus W$, is the point-wise supremum of forward-shifted versions of f in all convolved points of the structuring element W. That means that erosion returns the minimum value of all pixels that are completely contained inside the moving window W, whereas dilatation returns the maximum intensity of f within W. Therefore, the shapes contained in f are reduced or expanded by eroding or dilating the input image, respectively.

By combining the above morphological operators, opening and closing techniques can be defined. Opening is the dilatation of the erosion of f by a structuring element W and is given by [241],

$$f \circ W = ((f \ominus W) \oplus W) \tag{6.6}$$

Similarly, dilating an image f by a moving window W and then eroding the result by the same structuring element W yields the closing of f by W as [241],

$$f \bullet W = ((f \oplus W) \ominus W) \tag{6.7}$$

In this case, morphological closing is firstly applied on Gaussian filtered radar image using a disk structural element of radius $r = 3$ pixels and then this result is enhanced by opening the resulting image through a line structural element with 15 pixels length and oriented 45 degrees with respect to the origin of the input image. Then, first-order derivative filtering is applied to calculate the gradient of the processed image, $\triangledown f$, that is defined as [242],

$$\bigtriangledown f = \begin{bmatrix} \dfrac{\delta f}{\delta x} \\[2ex] \dfrac{\delta f}{\delta y} \end{bmatrix} = \begin{bmatrix} G_x \\[1ex] G_y \end{bmatrix} \tag{6.8}$$

where $\delta f / \delta x$ is the partial derivative of the image $f(x, y)$ with respect to x, i.e. the gradient in the x direction (G_x), and $\delta f / \delta y$ corresponds to the partial derivative of the image $f(x, y)$ with respect to y, i.e. the gradient in the y direction (G_y). Besides, the magnitude of the gradient $|\bigtriangledown f|$ and the gradient direction θ can be calculated by [242],

$$|\bigtriangledown f| = \sqrt{G_x^2 + G_y^2} \tag{6.9}$$

and

$$\theta = \arctan \frac{G_y}{G_x} \tag{6.10}$$

After gradient image has been computed, a thresholding procedure is applied considering that continuous pixels with larger values of $|\bigtriangledown f|$ are possible edge locations, which in turns represent the detected shoreline. Finally, the detected edge pixels are fitted to a high order polynomial function to smooth the results and to obtain the final shoreline estimation.

6.4 Results

6.4.1 Water Depth Estimation

The *uBathy* algorithm is applied on the radar images measured at Castelldefels beach. The k and h estimates from a radar sub-video are shown in Figure 6.4 considering the first EOF that explains 82 % of the total variance. Note that some outliers in k estimates distort the radar-derived water depth, mainly in that pixels where wave fields are discontinuous. This discontinuity is due to radar antenna rotation that yields a slightly time lag between consecutive pixels. However, this time lag is indeed shorter than the temporal parameters of the *uBathy* algorithm (i.e. $\triangle t$ and R_t). Therefore, sea clutter data after a complete radar rotation is considered as a *snapshot* image for practical reasons and simplicity (See Figure 2.1 in Section 2.4).

After all sub-videos have been processed, composite images are built using the mean, median and mode statistics of the retrieved wave frequency, wavenumber and water depths at the study area. Then, a median filter with a kernel size of 7×7 pixels is applied to remove outliers in k and to further enhance h estimates from radar images. Figure 6.5 illustrates the enhancement procedure to remove outliers using the median composite image depicted in Figure 6.6b. Figure 6.5a depicts the wavenumber estimates, where white dots represent outliers. Note that water depth outliers of up to 59 m in Figure 6.5b corresponds to pixel locations of k outliers in Figure 6.5a. Finally, radar-derived wavenumber and water depths are enhanced using the median filtering procedure (See Figures 6.5c and 6.5d, respectively). It is worth to note that k estimates
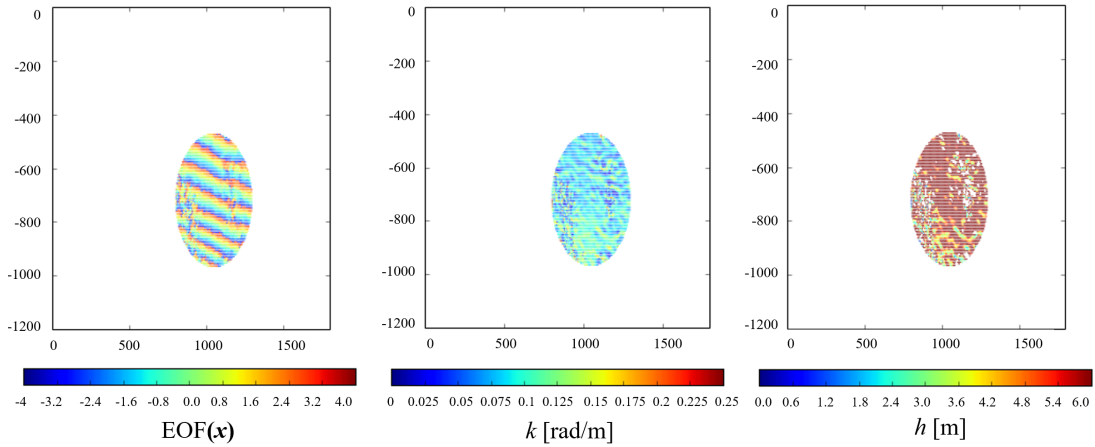
Figure 6.4: Wavenumber and water depth estimates from a radar sub-video using the main *mode* for the PCA analysis that explains 82 % of the total variance.
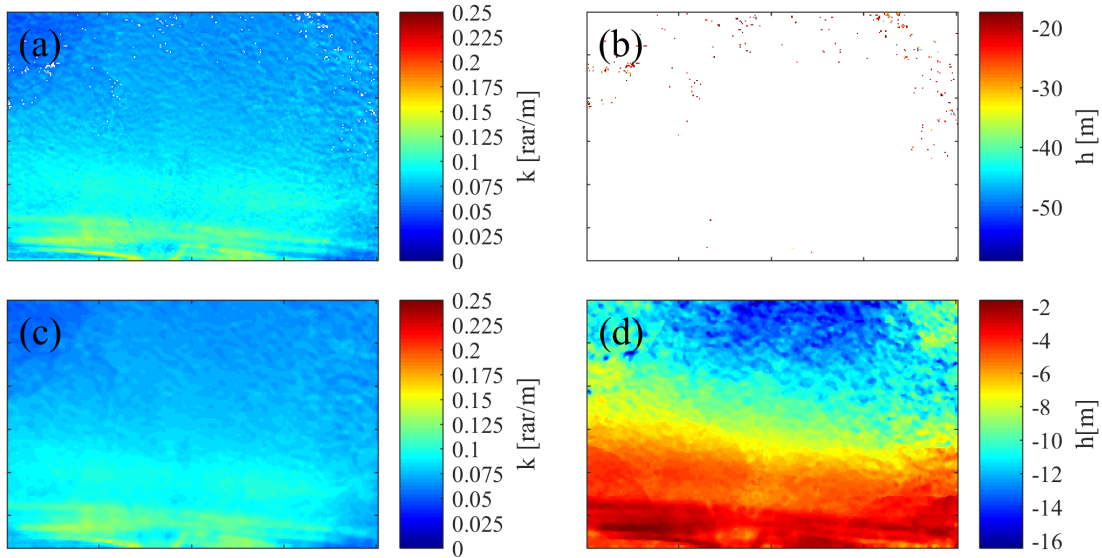
Figure 6.5: Enhancement procedure to remove outliers in k and h estimates using *uBathy* algorithm from remotely sensed radar images. **(a)** Wavenumber estimates; white dots represent outliers. **(b)** Water depth outliers. **(c)** Filtered wavenumber and **(d)** the enhanced bathymetric inversion.

are larger than the deep-water wavelength ω^2/g and shorter than the corresponding k at the minimum measured depth, i.e. $k < \omega/\sqrt{gh_{\min}}$ where $h_{min} =$0.87 m in this case.

Figures 6.6a to 6.6c show the processed and filtered mean, median and mode water depth composite images, respectively. These inferred depths are compared with in-situ measurements at a cross-shore transect, as shown in Figure 6.6d. Figure 6.2a indicates the transect location by the red dotted line. As it can be observed, mode composite image returns the largest error compared with in-situ data and hence Figure 6.6c is discarded for the analysis. Since mean and median bathymetric estimates behave similarly, both images are further analyzed in order to measure the quality of the recovered water depths inferred by the radar.

In this context, Figures 6.7a to 6.7c illustrate the bias error distribution from inferred mean
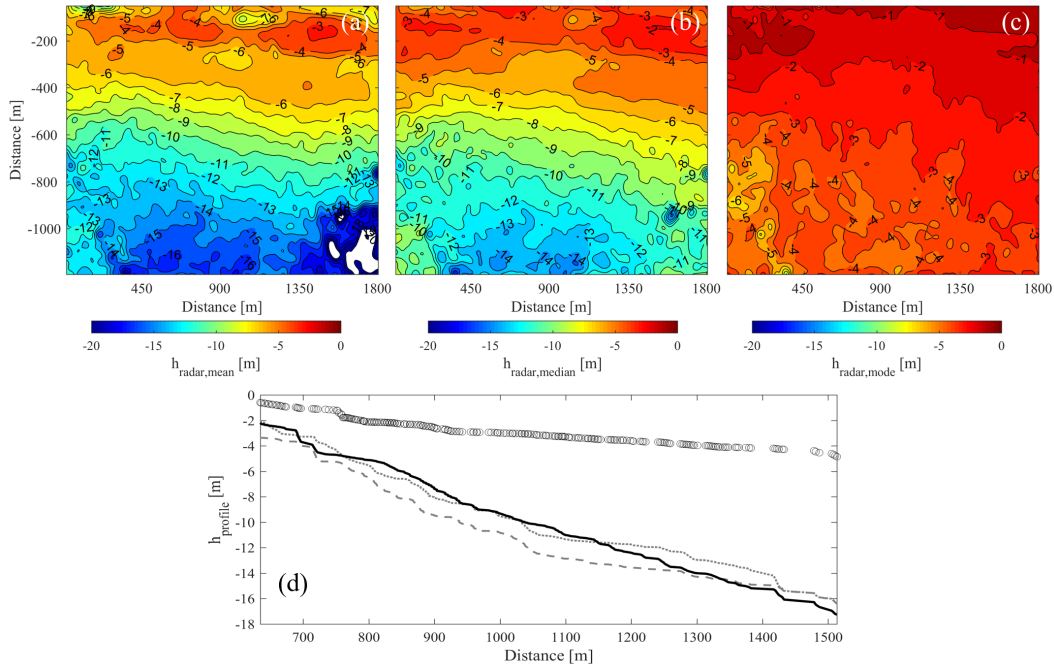
Figure 6.6: Inferred **(a)** mean, **(b)** median and **(c)** mode water depth composites. **(d)** Comparison of the radar-derived water depths and the in-situ measurements at a cross-shore transect. Transect location is indicated by the red dotted line in Figure 6.2a. Gray dashed and dotted lines are the mean and median radar-derived depth estimates, respectively. Circles are the mode statistic of the inferred water depths. Black line represents the in-situ measured depths at the cross-shore transect.
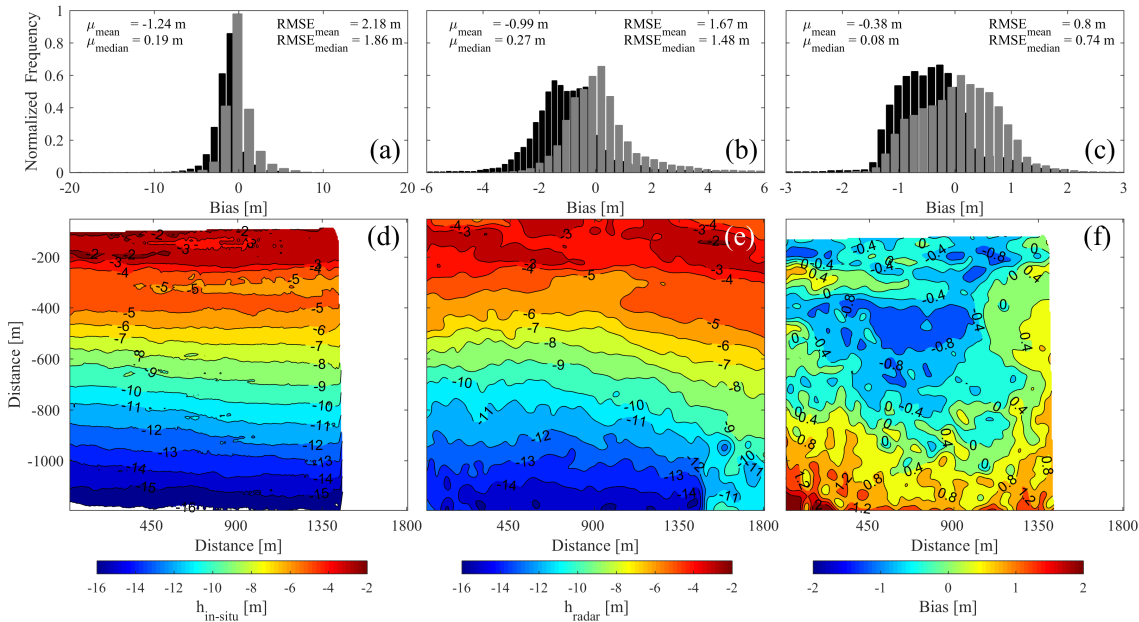
Figure 6.7: Normalized histograms of the bias errors from inferred mean (black bars) and median (gray bars) water depths compared with in-situ measured data. Bias error distribution for **(a)** raw and **(b)** enhanced h estimates using the median filtering and **(c)** considering non-linear effects. **(d)** In-situ measured and **(e)** the final radar-derived water depths, as well as **(f)** the difference between the gridded survey and the inferred water depths using the median composite image.

(black bars) and median (gray bars) water depths compared with in-situ measured data (Figure 6.7d). As it can be observed, the bathymetric inversion produces small errors using the median composite image. Raw *uBathy* results and enhanced *h* estimates by using the median filtering are depicted in Figures 6.7a and 6.7b.

To further compare the surveyed bathymetry with radar-derived depth estimates, Figures 6.8a and 6.8b depict a scatter plot for raw and enhanced h_{radar} estimates respectively, but only considering the median composite image (Figure 6.6b). Note that larger bias errors are obtained in the shallower (-5 m $\leq h \leq$ -1 m) and deeper (-16 m $\leq h \leq$ -10 m) water areas in the local bathymetry, where scatter distributions are coarser. Indeed, h_{radar} is overestimated at shallower areas and underestimated at deeper water, as shown in Figure 6.8b. Water depth estimates are *sufficiently* good at intermediate water depth zone (-10 m $< h <$ -5 m).

From Figure 6.8b, it can be observed that RMSE is reduced by applying the median filtering yielding a better agreement between h_{radar} and $h_{in-situ}$, i.e. $r = 0.97$ and RMSE $= 0.76$ m. However, limitations in the large and shallow water depth areas remain.
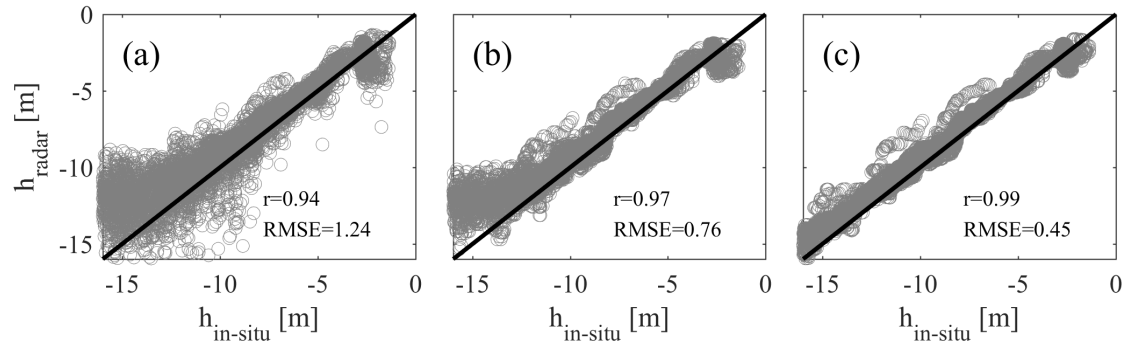
Figure 6.8: Comparison of surveyed depths and radar-derived **(a)** raw, **(b)** filtered and **(c)** final depth estimates at Castelldefels beach.

Mean differences between surveyed and radar-derived depth estimates are shown in Figure 6.9, in order to assess the average radar performance by applying the *uBathy* algorithm [16] to infer each given *h*. Black square markers indicate the errors obtained by the filtered *h* image. As stated above, three main zones are defined, i.e. shallow depths, intermediate depths and large depths, considering similarities in the average radar accuracy at the local bathymetry.

Note that radar performance is degraded at deeper (-16 m $\leq h \leq$ -10 m) and shallower (-5 m $\leq h \leq$ -1 m) waters. It is worth to note that large water depth areas are just located at the remote pixels where radar backscatter signal is weaker. However, shallower areas indeed correspond to the surf zone where non-linear wave transformations take place, which are associated with shoaling, wave breaking and transfer among different harmonics due to the finite water depth.

In order to reduce errors due to non-linear effects and weak echo signals, an empirical range dependent scaling factor $c(r_0)$ is included considering the radar antenna height $h_{ant} = 13$ m, the distance of each pixel to the antenna location, i.e. r_0, and the minimum local wavelength λ_{min,r_0} in meters at each r_0 location. This factor is used to correct the previous h_{radar} estimates at shallow and large water depth areas, i.e. $h_{radar,1} = h_{radar,0} + c(r_0)$, and is defined as,

$$c(r_0) = \pm\frac{2\lambda_{\min,r_0}h_{\text{ant}}}{r_0} \tag{6.11}$$

where $c(r_0)$ is positive at deeper water (-16 m $\leq h \leq$ -10 m) and negative at shallower water depths (-5 m $\leq h \leq$ -1 m), where h is under- and over-estimated, respectively. This factor is applied on both mean and median water depth composite images and the normalized histogram from bias errors is shown in Figure 6.7c. As it can be seen, mean bias error is 0.08 m from median water depth estimates. Besides, inferred h_{radar} and measured $h_{in-situ}$ are in good agreement with a high correlation coefficient $r = 0.99$ with a RMSE of 0.45 m, according to Figure 6.8c. Therefore, the final radar-derived water depth estimate is the filtered and empirically adjusted median composite, which is depicted in Figure 6.7e.

Figure 6.7f shows the difference between the gridded survey and the radar-inferred water depths, i.e. $h_{in-situ} - h_{radar}$. Note that over the vast majority of the overlapping domain, bias ranges from -0.5 m and 0.4 m. At the large and shallow water depths, mean bias is about 0.40 m and -0.37 m, respectively. Bias is up to 1.2 m only for lateral pixels at the remote areas.

Regarding Figure 6.9, gray circles represent the mean bias and RMSE considering the empirical scaling factor $c(r_0)$ for non-linear effects. As it can be observed, radar-derived depth estimates at intermediate depths (-10 m $< h <$ -5 m) are *sufficiently* good in both cases when the the empirical scaling factor $c(r_0)$ for non-linear effects are or not included. In this depth range, mean bias and RMSE are -0.37 m and 0.79 m when $c(r_0)$ is not included (i.e. only for filtered images). In contrast, considering the empirical correction the mean bias is -0.27 m with a RMSE of 0.65 m.
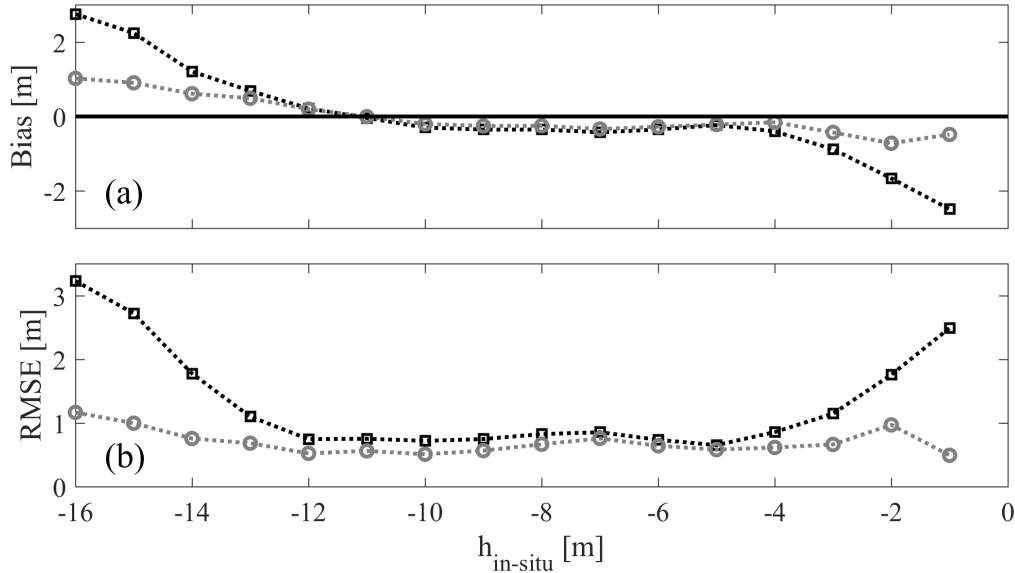
Figure 6.9: (a) Bias and **(b)** root-mean-square errors of radar-derived water depths using the *uBathy* algorithm [16]. Black square markers indicate the errors obtained by the filtered h image. Gray circles represent the results considering the empirical scaling factor $c(r_0)$ for non-linear effects.

Besides, at deeper water (-16 m $\leq h \leq$ -10 m), h is underestimated in both cases with a mean bias of 0.97 m and 0.40 m and a root-mean-square error of 1.58 m and 0.71 m using and not using the $c(r_0)$ factor, respectively. At shallower water (-5 m $\leq h \leq$ -1 m), the radar accuracy

strongly declines without considering the non-linear adjust. Hence, mean differences are larger, i.e. $\overline{\text{bias}}$ = -1.13 m and RMSE = 1.38 m respectively. Note that negative mean bias indicates that h is overestimated at this zone. After applying the empirical correction factor $c(r_0)$, errors are reduced with a mean bias of -0.37 m and a RMSE of 0.66 m at shallower depths.

6.4.2   Shoreline Detection

Regarding shoreline detection, Figure 6.10 illustrates the proposed approach applied on the normalized variance image. Variance image is calculated as the standard deviation in time domain from a series of hourly radar data measured at Cala Millor beach during October 22th-24th 2018. Pixel intensities larger than $\mu_{\text{var}} \pm 3\sigma_{\text{var}}$ in the variance image are considered outliers, where μ_{var} and σ_{var} are the mean and the standard deviation of the variance image intensities. Outliers are represented by white pixels in the radar coverage area, as shown in Figure 6.10a. Rocky outcrops are clearly identified.
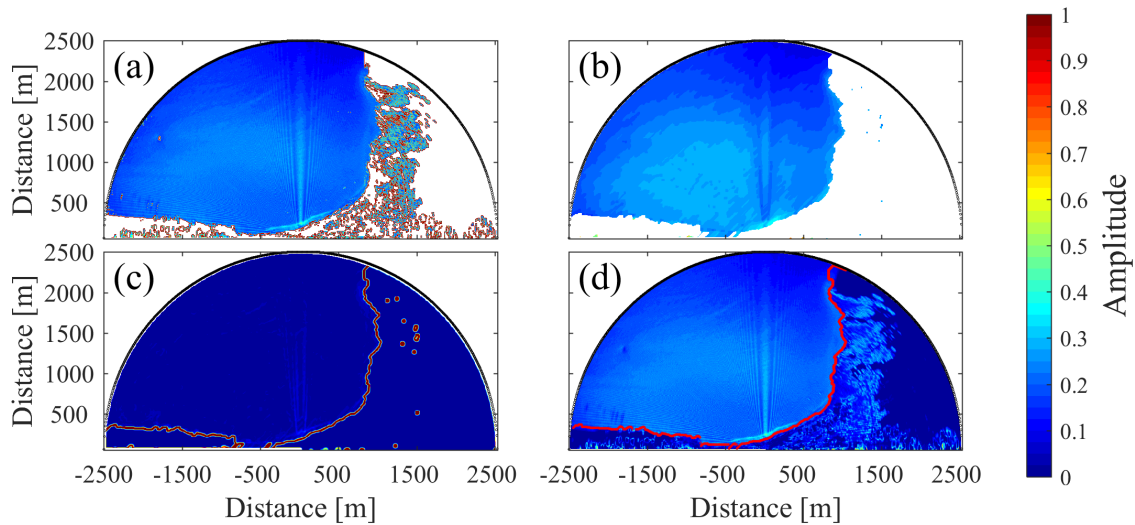
Figure 6.10: Shoreline detection using the variance image. **(a)** Normalized variance image. **(b)** Gaussian filtered and morphological operated image using closing and opening techniques. **(c)** Magnitude of the gradient and **(d)** the detected shoreline (red line) at Cala Millor beach.

Then, variance image is smoothed and enhanced by applying the Gaussian filtering and closing/opening morphological operators, as depicted in Figure 6.10b. The aim of this step is to remove discontinuities that do not correspond to the shoreline, e.g. buildings and shaded areas due to rocky outcrops backscattering obstruction, which can be possible error sources for the edge detection procedure. Thus, the magnitude of the gradient is calculated from the enhanced radar image.

After the gradient image has been computed, a thresholding procedure is applied, as shown in Figure 6.10c. Continuous pixels with larger values of the magnitude of the gradient, $|\bigtriangledown f| \geq 2.5$ when the variance image is the input signal, are considered as possible shoreline locations. These detected edge pixels are fitted to a high order polynomial function, $n = 9$, to smooth the results and to obtain the final shoreline estimation presented in Figure 6.10d over the original variance

image. Note that the radar-derived shoreline estimate not only includes the sand beach but also the rocky outcrops at the study site, where video systems cannot measure. The above procedure is also performed using mean and median images. Results are shown in Figure 6.11.
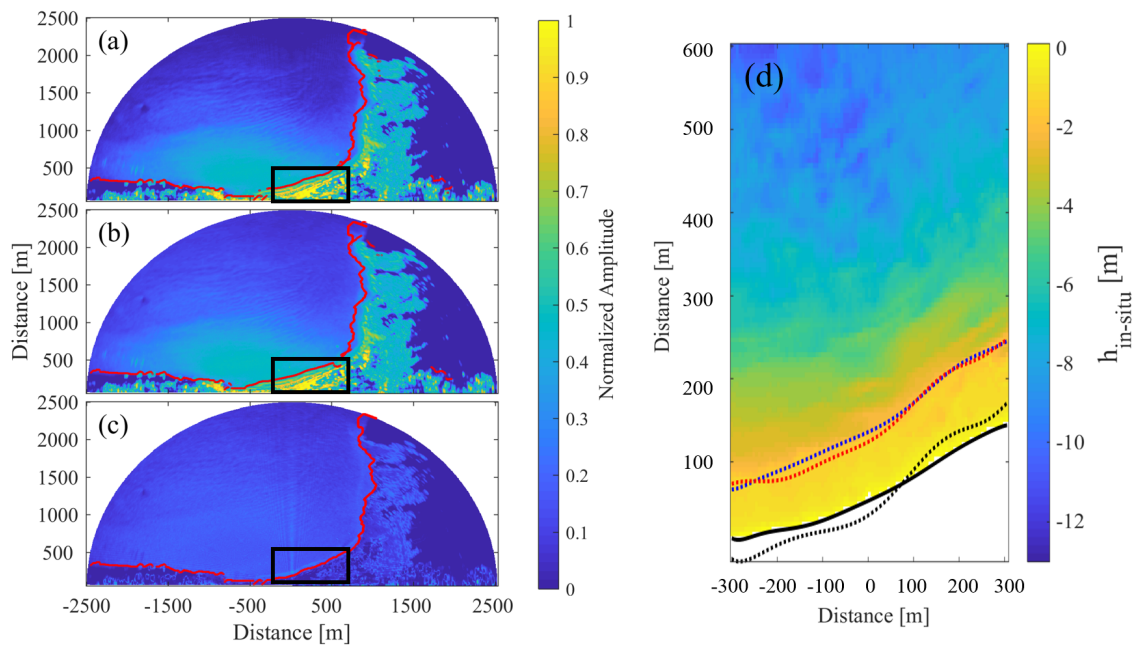
Figure 6.11: Radar-derived shoreline estimates using **(a)** mean, **(b)** median and **(c)** variance images. **(d)** Local shoreline estimates at the black square regions indicated in **(a-c)** that contain the submerged sandbars. Black line is the surveyed data. Blue, red and black dashed lines correspond to the shoreline estimates using mean, median and variance images, respectively.

According to Figures 6.11a and 6.11b, errors for shoreline detection are larger using mean and median images that wrongly identify submerged sandbars at about 200 m from the radar antenna as shoreline locations, mainly due to strong radar backscatter signal at that zone. Radar-derived shoreline using variance images are in good agreement with in-situ data, as shown in Figure 6.11c. Figure 6.11d shows the local shoreline estimates at the black square regions indicated in Figures 6.11a to 6.11c, which contain the submerged sandbars. Mean bias from mean and median images exceed the 50 m and shoreline locations are often overpredicted at seaward direction. In contrast, variance image achieves -3.74 m mean bias with a normalized error of 7.18% and RMSE of 2.49 m.

6.5 Discussion

Table 6.1 summaries the assessment of *uBathy* [16] and *cBathy* [159] bathymetric inversion algorithms using radar and video imagery. Radar and video performance by applying *cBathy* algorithm and the Kalman filter is reported in [146]. Optical video-based accuracy using both bathymetric inversion algorithms but without considering the Kalman filter is stated in [16].

It is worth to note that *uBathy* improves the results achieved by *cBathy*, providing smaller average error (bias) and RMSE at the different depth ranges considered. This proves that *uBathy*

algorithm, which has previously been evaluated only using video imagery [16], is suitable to be applied on field data from different remote sensor platforms, e.g. marine radars, with a similar overall accuracy to those obtained from video-derived depth estimates.

According to Table 6.1, the combination of *uBathy* estimates with the proposed post-processing techniques, i.e. median filtering to remove outliers and the empirical scaling factor in order to minimize errors due to non-linear effects, provides the best performance scenario. Besides, the total mean accuracy for radar-derived depth estimates is significantly higher than the achieved in [16] via optical video, with a mean bias of 0.08 m and RMSE of 0.45 m at the total study site. However, radar performance has lower fidelity depth estimates at intermediate depths than those reported in [146] using the Kalman filter.

TABLE 6.1: Assessment of the radar-derived water depth estimates using *uBathy* [16] algorithm compared with in-situ measurements and the reported accuracy on video-derived depth estimates using *cBathy* [159] and *uBathy* [16] algorithms.

Sensor	Results	*cBathy* [159] estimates			*uBathy* [16] estimates		
		Deeper	Intermediate	Shallower	Deeper	Intermediate	Shallower
Radar	Depth Range	-15 m$\leq h$ <-9 m	-9 m< h <-6 m	-6 m$\leq h \leq$0 m	-16 m$\leq h \leq$-10 m	-10 m< h <-5 m	-5 m$\leq h \leq$-1 m
	Bias	1.00 m	-0.02 m	-2.30 m	0.40 m	-0.27 m	-0.37 m
	RMSE	1.00 m	0.40 m	2.70 m	0.71 m	0.65 m	0.66 m
Video[a] [146]	Depth Range	-10 m$\leq h \leq$-5 m	-5 m< h <-1 m	-1 m$\leq h \leq$0 m	Not yet developed [16]		
	Bias	0.59 m	-0.01 m	-0.92 m			
	RMSE	0.79 m	0.34 m	1.0 m			
Video[b] [16]	Depth Range	-8 m$\leq h \leq$0 m			-8 m$\leq h \leq$0 m		
	Bias	-0.50 m			-0.27 m		
	RMSE	1.38 m			1.29 m		

a represents the performance using a series of hourly videos and applying the Kalman filter.
b denotes the results obtained from *cBathy* [159] and *uBathy* [16] algorithms considering only one video. The Kalman filter is not used.

Recently, Honegger *et al.* [166], [167] implemented the *cBathy* depth estimate algorithm on X-Band radar data at micro- [166] and macro-tidal [167] nearshore areas. As stated above, *cBathy* was originally designed from video cameras. They added a time lag correction between pixel time series in order to reduce possible error source, since *cBathy* algorithm has been exclusively applied to snapshot video images. Water depth estimates from X-Band radars show mean bias errors and RMSE of 0.26 m and 0.49 m, respectively, by applying the Kalman filter but without considering non-linear effects [166]. Hence, significantly higher errors are achieved at locations shallower than 2 m depth (surf zone). In contrast, bathymetric inversion from video imagery shows mean bias errors and RMSE of 0.23 m and 0.44 m, respectively [166]. In the extended case where tidal currents are considered on the linear dispersion relation [167], the mean bias error is 0.02 m with RMSE of 0.35 m. Therefore, inherent limitations of *cBathy* algorithm remain [166].

In this context, it can be observed that adding wave-current bathymetric interaction (as suggested [167] for *cBathy*) and Kalman filtering may decrease the bias and RMSE in about 40% obtained by using *uBathy* and the post-processing enhancement procedure that is proposed in this doctoral dissertation from radar data.

Regarding shoreline detection, Simarro *et al.* [125] also used video-derived variance images obtained from SIRENA open source code at Castelldefels beach (Spain) and Tairua beach (New Zealand). They obtained a mean bias of 8.5 m (0.6 m) and a relative error of 10.5% (6.1%), considering all videos at both studies sites (only at Castelldefels) [125]. In contrast, radar-derived variance images achieve -3.74 m bias error with a normalized error of 7.18% and RMSE of 2.49

m using the proposed shoreline detection approach based on digital processing techniques and first-derivative filtering.

Besides, surrounding rocky outcrops and submerged sandbars can also be identified in the radar image. However, onshore deposits of *Posidonia oceanica* meadows and crescentic sandbars often hinder the extraction of accurate shoreline in some regions.

6.6   Summary

The assessment of morphological mapping facilities of X-Band radars is performed by comparing radar-derived depths and shoreline estimates with in-situ data and the previously reported video performance at the study sites. Results reveal a promising use of X-Band radars and stereo-video systems as complementing nearshore monitoring tools, even although inherent trade-offs remain (i.e. the coarser spatial resolution and sea clutter image quality for X-Band radars and the degradation of video range resolution at cross-shore direction [166]). Therefore, radars and optical video systems should be considered as complementing morphological mapping tools, instead of excluding, in order to provide higher-resolution and more accurate bathymetric estimates and shoreline measurements in a broad area.

The *uBathy* algorithm [16] is adapted to radar systems considering more than 120 time windows with $w_t = 80$ s, $\triangle t = 10$ s, $\triangle x = 150$ m, $R_x = 250$ m and $R_t = 40$ s for each hourly sea clutter dataset at Castelldefels beach. Since more sub-videos are available, ω and k can be recovered with high accuracy. Median composites of radar-derived depth estimates are combined with a median filtering to remove outliers and the empirical scaling factor in order to minimize errors due to non-linear effects, providing the best performance scenario (i.e. mean bias and RMSE of 0.08 m and 0.45 m respectively, and $r = 0.99$).

Using this configuration, we obtained that *uBathy* improves the results achieved by *cBathy* from both radars and video imagery, providing smaller average error (bias) and RMSE at the different depth ranges considered. This proves that *uBathy* algorithm, which has previously been evaluated only using video imagery [16], is suitable to be applied on field data from different remote sensor platforms, e.g. marine radars, with a similar overall accuracy to those obtained via video systems. Further studies may consider the assessment of radar accuracy by adding wave-current bathymetric interaction and Kalman filtering in the *uBathy* algorithm [16].

Over the vast majority of the study site, bias errors range from -0.5 m and 0.4 m. At the large and shallow water depths, the mean bias is 0.40 m and -0.37 m, respectively. Only for lateral pixels at the remote areas the bias error is up to 1.2 m, where radar backscatter signal is weaker. Larger bias errors are obtained at the shallower water (-5 m $\leq h \leq$ -1 m) and deeper water (-16 m $\leq h \leq -10$ m) areas in the local bathymetry. Indeed, h_{radar} is overestimated at shallower areas and underestimated at deeper water. Water depth estimates are *sufficiently* good at intermediate water depth zone (-10 m $< h <$ -5 m). Shallower water correspond to the surf zone where non-linear wave transformations take place, which are associated with shoaling, wave breaking and transfer among different harmonics due to the finite water depth. Radar accuracy is enhanced at this zone including the empirical range dependent scaling factor $c(r_0)$.

Finally, a method for automatic extraction of the shoreline is proposed applying digital image processing and first-order derivative filters on variance images. Mean bias and normalized errors from radar-derived shoreline estimate are comparable to those achieved via optical video. Besides, surrounding rocky outcrops and submerged sandbars can also be identified using radar images. However, onshore deposits of *Posidonia oceanica* meadows and crescentic sandbars often hinder the extraction of accurate shoreline in some regions.

Chapter 7

Conclusions

"In the depth of winter, I finally learned that within me there lay an invincible summer."

Albert Camus (1913 – 1960)

Remote sensing is a challenging task in nearshore areas. Environmental conditions at the moment of image capture as well as the inherent random nature of highly dynamic coastal processes often degrade estimates at site-specific spatio-temporal scales. Therefore, pre-processing is crucial to improve the potential for deriving wave properties using remotely sensed data and the final results rely on the the effort invested in this previous step. Future trends in hydrodynamics and morphodynamics monitoring in shallow water highlight the increasing capability of remote sensors to be merged with different data sources in order to provide continuous and more detailed information.

In this context, this PhD thesis provides new insights aimed to advance in the use of X-Band radars in coastal areas to obtain reliable, autonomous and continuous measurements for hydrodynamical and morphodynamical processes in the nearshore and to combine this system with optical video to improve both diagnostic and prognostic of coastal processes. Hence, this research exhibits the scopes and limitations from radar remote sensing systems at different coastal environment (e.g. sand-beaches, coral reefs and semi-stretched beaches) in order to examine the opportunity to merge the advantages of radars and video cameras, which could improve the reliability of retrieved coastal data.

First, a shadowing mitigation methodology has been proposed by combining signal and image processing techniques as well as spectral analysis to reproduce with high accuracy the sea state parameters in nearshore areas from remotely sensed radar data. The method is based on filtering and interpolation approaches and is able to estimate sea state parameters including significant wave height (H_s), peak wave direction (θ_p), peak period (T_p) and peak wavelength (λ_p) in shallow waters with high accuracy. Traditional empirical and semi-empirical calibration methods, which use signal-to-noise ratio and in-situ measurements as external references, are avoided by using image enhancement techniques. Besides, distortions introduced by the radar acquisition process and the power decay of the radar signal along distance are compensated.

Errors for H_s, θ_p and T_p calculated as the difference between estimated and true data show a mean bias and a relative value of 0.05 m (2.72%), 1.52° (5.94%) and 0.15 s (1.67%), respectively. The directional and wave energy spectra derived from radar estimates, AWAC and ADVs record

as well as JONSWAP formulation are presented to illustrate the improvement resulting from the proposed method over frequency domain. The best performance is achieved when the significant wave height is at least 0.5 m and preferably higher and the peak period is $T_p \geq 4$ s.

Then, a completely novel use for X-Band radars is introduced by estimating wave energy dissipation rate, wave friction factors and the equivalent bottom roughness using the above pre-processing methodology. Datasets were obtained from radar-measured field data at San Andres Island barrier-reef system. Two physical formulations (i.e. Nielsen [12], [13] and Madsen *et al.* [14], [15] approaches) are assessed and each pixel of the radar image considered as a single virtual sensor. The results obtained show that Madsen's *et al.* spectral wave model adequately estimates the bottom roughness (k_w) as 0.20 m. In contrast, the formulation of Nielsen slightly overestimate k_w in most of the locations because they were originally determined by fitting laboratory data from monochromatic waves studied over a fixed rough bottom.

Considering raw-radar intensities, the fore reef, reef flat and lagoon regions are identified by visual inspection. However, an alternative unsupervised classification procedure to delineate the inner and the outer reef zones (i.e. lagoon and fore reef areas, respectively) is also proposed. Johnny Cay and a sandy beach section are detected through the discrimination of large shaded areas with low intensity. Shoreline and reef rim are also identified by using the magnitude of the image gradient.

Results reveal that the reef attenuates incident waves by approximately 75% due to both frictional and wave breaking dissipation. Furthermore, the mean values of $f_{wr,Madsen} = 0.18$ and $k_{w,Madsen} = 0.20$ m obtained in the study area are comparable with estimates derived from in-situ moorings at coral reefs and endemic *Posidonia oceanica* meadow canopies. Besides, the standard deviation of the measured bed elevation σ_b and the height of the bottom roughness elements H_{bed}, i.e. the mean height of the coral elements, are estimated, which are in good agreement with previous in-canopy flows models. Moreover, the highest $H_{bed} = 0.25$ m and $\sigma_b = 0.17$ m are comparable to values obtained at others barrier-reef systems from in-situ wave and currents data.

Since wave height derived from radar are in good agreement with model-predicted H_s as well as by in-situ measurements, results reveal that X-Band marine radars can describe prominent features of coral reefs, including the delineation of reef morphological structure, wave energy dissipation and wave transformation processes in the lagoon. For future studies, velocity measurements may improve the understanding of radar performance.

The assessment of morphological mapping facilities of X-Band radars is performed by comparing radar-derived depths and shoreline estimates with in-situ data and the previously reported video performance in the study sites. Results reveal a promising use of X-Band radars and stereo-video systems as complementary monitoring tools, even although inherent trade-offs remain (i.e. the coarser spatial resolution and sea clutter image quality for X-Band radars and the degradation of video range resolution at cross-shore direction [166]). Therefore, radars and optical video systems should be considered as complementing morphological mapping tools, instead of excluding, in order to provide higher-resolution and more accurate bathymetric estimates and shoreline measurements in a broad area.

The *uBathy* algorithm [16], which has previously been evaluated only using video imagery [16],

is adapted to radar systems through the redefinition of optimal parameters taking into account the radar pixel resolution and the sampling rate. Besides, more sub-videos are available and hence ω and k can be recovered with high accuracy. A post-processing technique is proposed to improve radar-derived depth estimates. Median composites of inferred depths are combined with a median filtering to remove outliers and the empirical scaling factor in order to minimize errors due to non-linear wave transformations, providing the best performance scenario (i.e. mean bias and RMSE of 0.08 m and 0.45 m respectively, and $r = 0.99$).

According to results, larger bias errors are obtained in the shallower (-5 m $\leq h \leq$ -1 m) and deeper (-16 m $\leq h \leq$ -10 m) regions in the local bathymetry. Indeed, h_{radar} is overestimated at shallower areas and underestimated at deeper water. Water depth estimates are *sufficiently* good at intermediate water depth zone (-10 m $< h <$ -5 m). Shallower water correspond to the surf zone, where non-linear wave transformations associated with shoaling, wave breaking and transfer among different harmonics due to the finite water depth, take place. Radar accuracy is enhanced at this zone including the empirical range dependent scaling factor $c(r_0)$.

Therefore, we obtained that *uBathy* improves the results achieved by *cBathy* from both radars and video imagery, providing smaller average error (bias) and RMSE at the different depth ranges considered. This proves that *uBathy* algorithm, is suitable to be applied on field data from different remote sensor platforms, e.g. marine radars, with a similar overall accuracy to those obtained via video systems. Further studies may consider the assessment of radar accuracy by adding wave-current bathymetric interaction and Kalman filtering in the *uBathy* algorithm [16].

Finally, a method for automatic extraction of the shoreline is proposed applying digital image processing and first-order derivative filters on variance images. Mean bias and normalized errors from radar-derived shoreline estimate are comparable to those achieved via optical video. Besides, surrounding geological paleo-channels and submerged sandbars can also be identified using radar images. However, onshore deposits of *Posidonia oceanica* meadows and crescentic sandbars often hinder the extraction of accurate shoreline in some regions.

It is worth to note that radar remote sensing is a complementary nearshore monitoring approach, which does not necessarily replace in-situ surveys due to their coarser spatio-temporal resolution for some specific applications. However, marine radars provide accurate wave data in broad areas that can support coastal management services and numerical modelling related to the assessment of coastline evolution, detection of crescentic sandbars, water depth changes, wave energy dissipation in coral reefs and estimation of sea state parameters, as obtained in this doctoral dissertation. Therefore, extreme changes in the beach shape can promptly be detected in order to generate early warnings of flooding risk, beach erosion and coral reefs threats.

Appendix A

List of Publications

This doctoral dissertation is presented as a monograph. The following chapters are an edited version of some published and in preparation research articles:

- **Chapter 4.** W. Navarro, J. C. Velez, A. Orfila, and S. Lonin, "A Shadowing Mitigation Approach for Sea State Parameters Estimation Using X-Band Remotely Sensing Radar Data in Coastal Areas", *IEEE Transactions on Geoscience and Remote Sensing*, vol. 57, no. 9, pp. 6292–6310, 2019, ISSN: 1558-0644. DOI: 10.1109/TGRS.2019.2905104.

  W. Navarro, J. C. Velez, and A. Orfila, "Estimation of sea state parameters using X-band marine radar technology in coastal areas", in *Sixth International Conference on Remote Sensing and Geoinformation of the Environment (RSCy2018)*, Paphos, Cyprus: Proc. of SPIE Vol. 10773, 2018, pp. 107730X–1–10. DOI: 10.1117/12.2322614.

- **Chapter 5**. W. Navarro, J. C. Velez, A. Orejarena-Rondón and A. Orfila, February 2020, "Wave Energy Dissipation in a Shallow Coral Reef Lagoon using X-Band Marine Radar Data", *Journal of Geophysical Research*, (submitted for publication).

- **Chapter 6**. W. Navarro, G. Simarro, A. Orfila and J. C. Velez, "Coastal Morphodynamics Study Using X-Band Marine Radar Data", (in preparation).

Other related works, projects and awards that support this doctoral dissertation:

- W. Navarro, J. C. Velez, and A. Orfila, *Best Paper Award*. "Estimation of sea state parameters using X-band marine radar technology in coastal areas". *Sixth International Conference on Remote Sensing and Geoinformation of Environment (RSCy2018)*. Paphos, Chipre. 25th March 2019.

- International Research Project. "Desarrollo de un sistema de medida de variables morfodinámicas mediante radares de microondas". Ref: COOPA20156. *I-COOP+2016 CSIC Program of Scientific Cooperation for Development*. 2017-2018. I.P.: Alejandro Orfila PhD. Doctoral student: Wendy Navarro. Majorca, Balearic Islands, Spain.

- International Research Project. "Propagación de oleaje y transporte de sedimentos sobre arrecifes de coral. Estrategias de gestión ante el cambio global". *Proyectos de Ciencia, Tecnología e Innovación en Geociencias*. 2014-2016. I.P.: Serguei Lonin PhD. Co-I: Alejandro Orfila PhD. Doctoral student: Wendy Navarro. Colombia.

- International Research Project. "Morfodinámica costera: Modelización de los procesos intra-ola". Ref. CTM2015-66225-C2-2-P. CSIC-IMEDEA. 2015-2018. I.P.: Alejandro Orfila PhD. Doctoral student: Wendy Navarro. Spain.

- International Research Project. "Desarrollo de métodos de procesamiento de señales de radar para obtener las características del oleaje en costas y arrecifes de coral". 2020. Universidad del Norte. I.P.: Juan Carlos Vélez PhD.

- National Research Project. "Desarrollo de un sistema de sensado remoto con radares de microondas para el estudio del oleaje y la morfodinámica costera". *Anexo 16: Doctorados Nacionales*. Instituto Colombiano para el Desarrollo de la Ciencia y la Tecnología, COL-CIENCIAS. 2017-2019. I.P.: Juan Carlos Vélez PhD. Doctoral student: Wendy Navarro. Colombia.

- W. Navarro, J. C. Velez, and A. Orfila, "Coastal hydrodynamics and morphodynamics description using X-Band Marine Radar Technology". *SENALMAR Congress*, 2019. Barranquilla, Colombia. Poster presentation. 25th October 2019.

- W. Navarro, J. C. Velez, and A. Orfila, "Developing a Remote Coastal Sensor based on X-Band Marine Radar Technology". *Uninorte Investiga Congress*, 2019. Barranquilla, Colombia. Poster presentation. 5th June 2019.

- W. Navarro, Third position *Pitch Todo Es Ciencia*. Instituto Colombiano para el Desarrollo de la Ciencia y la Tecnología, COLCIENCIAS, Colombia, April 2018.

- W. Navarro, "Remote Sensors in Oceanography". *Conference on Climate Change Management Strategies and Oceanographic Studies in the SEAFLOWER Biosphere Reserve*. San Andres Island, Colombia. Oral presentation. 20th June 2017.

Appendix B

Stochastic Description of Ocean Waves

Wind-generated ocean waves change randomly with time. Hence, wave height (peak-to-trough excursions) and wave period are non-repeatable from one cycle to another in time and space. Figure B.1 depicts a sea surface elevation profile in time domain travelling from deep water to shallow water areas. In shallow water, the relation $kh < \pi/10$ is satisfied, where k is the wavenumber and h represents the local water depth [19]. It can be seen that peaks and troughs of the wave profile, i.e. wave displacement from mean value, are similar in deep water obeying a normal probability distribution. However, wave profile has a large number of sharp peaks and weak troughs in shallow water because of non-linearities in nearshore areas. It leads to an asymmetric sea surface probability density function (PDF) with respect to the mean value.
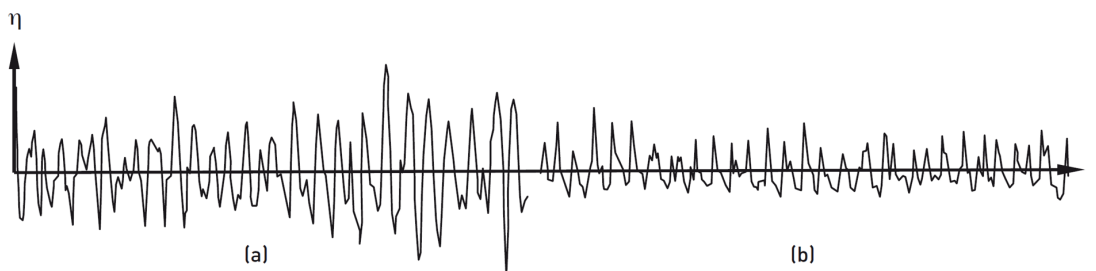
Figure B.1: Sea surface elevation η in severe seas at **(a)** deep water and **(b)** shallow water [243].

In this regard, ocean waves are assumed as Gaussian random stochastic processes in deep water. That means waves are steady in space, ergodic random processes and any displacement from the mean sea level are normally distributed [20]. In contrast, non-Gaussian random processes take place in shallow water areas where wave properties are affected by water depth. It suggests that wave characteristics transform from Gaussian to non-Gaussian random processes as they approach towards shoreline. Although there are some exceptions where shallow water waves can be considered as Gaussian random processes (e.g. when the sea severity is very mild), the concept of non-Gaussian random processes is generally used for statistical description of waves in shallow water. The degree of sea severity can be defined by the area under the density spectral function, which is described later in this section [20].

According to Figure B.1, the evaluation of random wave properties is almost impossible to be performed by a wave-by-wave analysis in time domain. Therefore, the random waves have to

be considered as stochastic processes in order to statistically evaluate wave properties through frequency and probability domains [20], [243].

For the mathematical representation of random wave profiles, let us consider a progressive wave in deep water using the coordinate system (X, Y, Z) fixed in space, θ represents the counter-clockwise angle with respect to X-axis [20]. As an initial approach, the profile of simple harmonic sea surface waves η may be described as,

$$\eta(x, y, t) = a \cos \left\{ \frac{\omega^2}{g} \left(x \cos \theta + y \sin \theta \right) - \omega t + \epsilon \right\} \tag{B.1}$$

where a, ω and ϵ are the wave amplitude (in meters), angular frequency (in radians/s) and phase (in radians), respectively.

The profile of random ocean waves can be written as shown in Equation B.2 based on the assumption that a sea surface elevation profile at time t is formed by an infinite number of j-th sinusoidal components with random amplitudes, directions and frequencies covering the range $0 < a_j < \infty$, $-\pi < \theta_j < \pi$ and $0 < \omega_j < \infty$, respectively. Besides, the phase ϵ is a random variable uniformly distributed in the range $-\pi < \epsilon_j < \pi$ whose magnitude depends on frequency ω_j and angle θ_j.

$$\eta(x, y, t) = \sum_j a_j \cos \left\{ \frac{\omega_j^2}{g} \left(x \cos \theta_j + y \sin \theta_j \right) - \omega_j t + \epsilon_j(\omega_j, \theta_j) \right\} \tag{B.2}$$

Figure B.2a shows a comprehensive sketch to explain the stochastic fluctuation of the sea surface displacements through the sum of a large series of statistically independent harmonic wave components which follow a random phase-amplitude model. Therefore, Fourier analysis and spectral techniques can be used for performing the stochastic analysis and description of random ocean waves [19], [20].

Besides, Figures B.2b and B.2d illustrate a set of n wave displacement records in time domain (i.e. $X_1(t), X_2(t), X_3(t), ..., X_n(t)$) dispersed in a certain area in the ocean to elaborate the definition of ocean waves as a stochastic process. Hence, $X(t_j)$ at any time is a random variable that relies on time and sample space. The set $\left\{ X_1(t_j), X_2(t_j), X_3(t_j), ..., X_n(t_j) \right\}$ is a random sample of size n or an *ensemble* at time t_j. The probability density function of the ensemble can be obtained by constructing a histogram from the wave records. It may be normally distributed with zero mean, as shown in Figure B.2c.

Sea surface random fluctuations generally relies on energy transfer from the local wind to sea. However, another ocean wave systems, also known as *swell*, is formed by a train of fairly large and more regular waves with minor or even no wind, which have moved away from their generating area. Wave spectrum allows clear identification of both swell and the local wind-generated waves in the frequency domain, as shown in Figure B.3 [20], [244]. It is evaluated from auto-correlation function defined in the time domain by applying the Weiner-Khintchine theorem which states that correlation function $R_{xx}(\tau)$ and the spectral density function $S_{xx}(\omega)$ are a Fourier transform pair defined as,

(a) Structure of random sea   **(b)** Set of wave records   **(c)** Histogram of ensemble   **(d)** Ensemble at time t_j and $t_j + \tau$
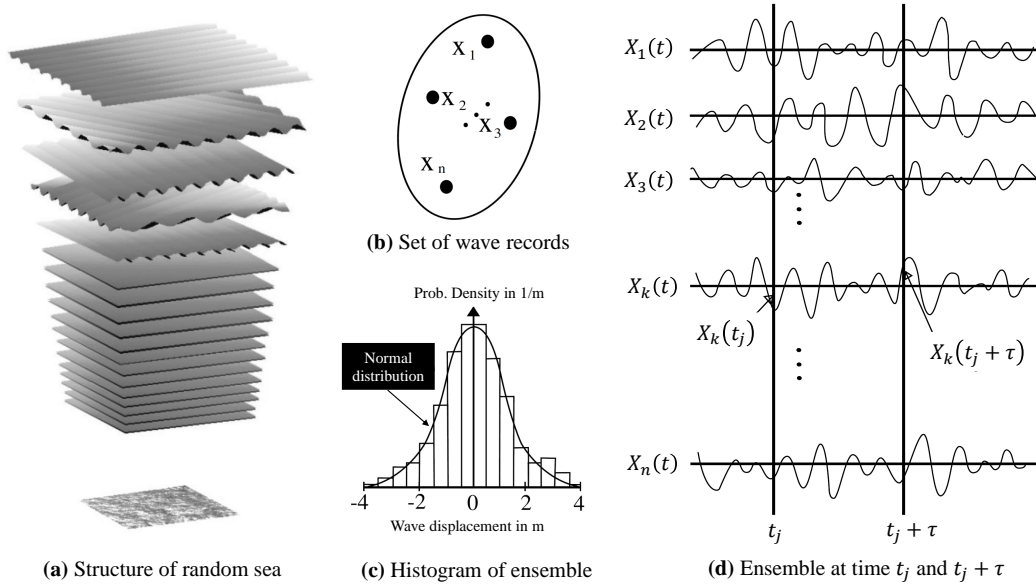
Figure B.2: Random ocean waves. **(a)** Structure of random sea surface: Sum of infinite sinusoidal components with different directions, amplitudes, frequencies and phases. **(b)** Definition of ensemble of random waves using a set of wave records. **(c)** Histogram of ensemble. **(d)** A complete ensemble at time t_j and $t_j + \tau$

$$S_{xx}(\omega) = \frac{1}{\pi} \int\limits_{-\infty}^{\infty} R_{xx}(\tau) e^{-j\omega\tau} \, d\tau; \qquad R_{xx}(\tau) = \frac{1}{2} \int\limits_{-\infty}^{\infty} S_{xx}(\omega) e^{j\omega\tau} \, d\omega \qquad (B.3)$$

where τ represents a shift in time in seconds.

Since $R_{xx}(\tau)$ and $S_{xx}(\omega)$ are both real and even functions and assuming that wind-generates waves are a steady-state ergodic random process, Equation B.3 can be presented in terms of frequency f (in hertz) as,

$$S_{xx}(f) = 2 \int\limits_{-\infty}^{\infty} R_{xx}(\tau) e^{-j2\pi f\tau} \, d\tau = 4 \int\limits_{0}^{\infty} R_{xx}(\tau) \cos(2\pi f\tau) \, d\tau$$

$$R_{xx}(\tau) = \frac{1}{2} \int\limits_{-\infty}^{\infty} S_{xx}(f) e^{j2\pi f\tau} \, df = \int\limits_{0}^{\infty} S_{xx}(f) \cos(2\pi f\tau) \, df$$

$$(B.4)$$

where $R_{xx}(0)$, also known as zero order spectral moment (m_0 or $\overline{P}$), represents the average wave energy in time domain that defines sea severity through the variance of waves. It can be calculated as the area under the spectral density function as,

$$m_0 = \int\limits_{0}^{\infty} S_{xx}(\omega) \, d\omega = \overline{P} = R_{xx}(0) = \text{Var}\left[\eta(t)\right] \qquad (B.5)$$

In this regard, wave height of the zero-order moment $H_{m_0} = 4\sqrt{m_0}$ is the most widely used wave parameter to define the sea severity. For a narrow-band wave spectrum (i.e. wave energy is concentrated around the peak frequency) H_{m_0} is practically equal to the significant wave height

H_s or $H_{1/3}$ which is the average height of the $N/3$ largest waves in $S_{xx}(\omega)$.
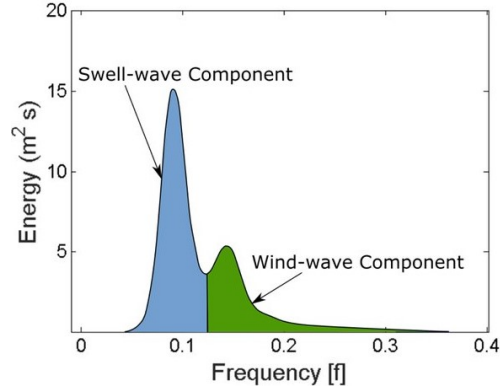
Figure B.3: Example of a combined swell and wind-generated wave spectrum [244]

Since ocean waves do not necessarily move in the same direction of wind, the wave energy spreads in various directions. Therefore, a directional spectral density function, denoted by $S(\omega, \theta)$, may be considered. This function defines the time average of wave energy at any frequency interval $\Delta\omega$ and for any directional angle interval $\Delta\theta$ [20], [243]. Ignoring ρg factor, directional spectral density function of random sea waves can be written as,

$$S(\omega, \theta) = \frac{1}{2}\rho g a_j^2 \quad \cong \quad \frac{1}{2}a_j^2 \tag{B.6}$$

where ρ is the density of water, g represents the acceleration of gravity and a_j is a positive random variable.

Moreover, wave spectrum can be obtained as a function of wavenumber $S(k)$ instead of angular frequency $S(\omega)$. That is, from $S(\omega)$ to $S(k)$,

$$S(k) = \left[S(\omega) \times \frac{\mathrm{d}\omega}{\mathrm{d}k}\right]_{\omega=\mathrm{f}(k)} \tag{B.7}$$

where ω is a function of k that corresponds to $\omega = \sqrt{kg\tanh(kh)}$ using the linear dispersion relationship (see Equation 2.2). Besides, $\mathrm{d}\omega/\mathrm{d}k$ is the wave group velocity. For deep water waves, we have $\omega = \sqrt{kg}$ and $\mathrm{d}\omega/\mathrm{d}k = 0.5\sqrt{g/k}$.

From $S(k)$ to $S(\omega)$,

$$S(\omega) = \left[S(k) \times \frac{\mathrm{d}k}{\mathrm{d}\omega}\right]_{k=\mathrm{f}(\omega)} \tag{B.8}$$

where k is defined as a function of ω that is $k = \omega^2/g$ for deep water waves. However, k cannot be expressed in closed form for waves of finite water depth. Hence, wavenumber has to be evaluated as a function of water depth h. The stochastic process for $S(k)$ in space domain can be defined as wave profiles at a time t along a longitudinal section X. Therefore, x-axis in Figure B.2d would be distance (in meters) instead of time (in seconds).

Appendix C

Description of a Pulse X-Band Marine Radar

A monostatic pulse marine radar consists of a transmitting/receiving microwave antenna that emit a train of modulated electromagnetic pulses of short duration and high power, as shown in the block diagram of Figure C.1. The duplexer (e.g. a solid-state circulator) permits a single antenna to be time-shared for both transmission and reception, protecting the receiver from damage when the high-power transmitter is on. The directive antenna concentrates the electromagnetic energy into a narrow beamwidth. Hence, reflecting objects can be described in size and shape through both range and angle resolutions, taking advantage of the fact that the radiated energy is slightly attenuated under fog, rain and weather conditions.

The transmitting-receiving X-Band radar antenna rotates to completely cover the surrounding area and its speed of rotation relies on mechanical and scanning factors. Radar transmitter generates high-power signals with stable waveforms, which operate in a wide bandwidth according to the radar type. Receiver separates the desired signal from the interfering or noisy signal through the low noise filter amplifier. Then, the echo signal is translated to an intermediate frequency (IF) using the mixer and the local oscillator. The IF amplifier maximizes the signal-to-noise ratio as a matched filter. Finally, the processing is applied to obtain the target data, rejecting undesired signals, such as *clutter* [209].

Radar equation describes the relationship between range of detection and the radar parameters that is given by,

$$P_r = \frac{P_t G_t}{4\pi R^2} \times \frac{\sigma}{4\pi R^2} \times A_e \tag{C.1}$$

where P_r and P_t denote the received and transmitted power (in watts) from an antenna of gain G_t. Besides, σ represents the target radar cross-section (RCS) in square meters. The first factor in Equation C.1 is the transmitted power density at a distance R in meters. The product of the first two terms corresponds to the power per square meter returned to the radar antenna. The effective aperture antenna A_e is defined as $A_e = \lambda^2 G_t / 4\pi$ since the same antenna is used for both transmitting and receiving [209].

According to Equation C.1, the range is proportional to the fourth root of the transmitted power. Hence, the power must be increased by 16 to double the range. This means that there is a necessary balance as well as an economical limit between transmission power and the range of a radar. Therefore, radar equation can also be expressed in terms of the minimum detectable signal
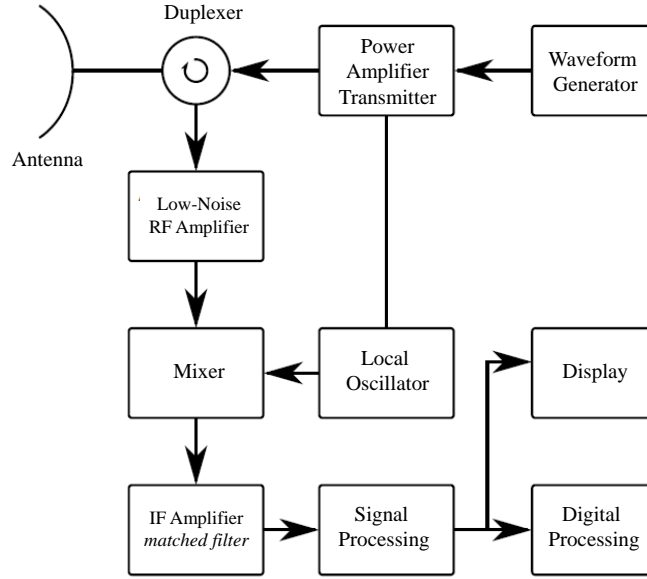
Figure C.1: Simple block diagram of a monostatic pulse radar [209].

or sensitivity $S_{\min}$ as,

$$R_{\max}^4 = \frac{P_t G_t^2 \lambda^2 \sigma}{(4\pi)^3 S_{\min}} \tag{C.2}$$

where $R_{\max}$ represents the maximum radar range and $S_{\min}$ is a statistical quantity defined as,

$$S_{\min} = kT_0 BF_n \frac{E}{N_0} \tag{C.3}$$

where k is Boltzmann's constant, T is the temperature, B is the receiver bandwidth and the factor F_n is the receiver noise figure at a $T_0 = 290$K being $kT = 4 \times 10^{-21}$ W/Hz. Sometimes $T_0 F_n$ is replaced with the system noise temperature T_s. Therefore, $S_{\min}$ is calculated by multiplying the signal-to-noise (SNR) ratio E/N_0 required for reliable detection by the receiver noise, which in turn relies on the thermal noise produced by an ideal receiver.

Since radar equation describes the incident electromagnetic wave energy dispersed by different objects in all direction, the intensity of echo signal can be directly defined by the physical characteristics of the targets such as shape, material and velocity. Radar Cross Section (RCS) is a target characteristic that explains the percentage of transmitted power that returns to radar antenna in the same direction and with the same polarization of the incident electromagnetic wave because of backscattering. The symbol σ designates the RCS of an object, which is defined by the projected area of a metal sphere that can be substituted by the target since it scatters the same power back to radar [209]. Hence, RCS relates the scattered power density at the receiver P_{D_r}, with the incident power density at the target P_{D_i}, through a limit in the far field of radar radiation given by,

$$\sigma = \lim_{R \to \infty} 4\pi R^2 \frac{P_{D_r}}{P_{D_i}} \tag{C.4}$$

Radar footprint receives echo signals not only from the target but also from the physical environment including ground and sea clutter. Since sea clutter can be defined as a surface-distributed process, the basic clutter parameter is the normalized radar cross-section (NRCS) σ_0 of the surface, which is expressed in decibels relative to $1 \, \text{m}^2/\text{m}^2$. It is obtained by dividing the measured RCS σ of an illuminated patch of the surface by a normalizing area A [209]. That is,

$$\sigma_0 = \frac{\sigma}{A} \tag{C.5}$$

For a radar with an antenna beamwidth B and a rectangular pulse of length T covering a range R with a grazing angle θ, the area A is defined either

$$A = \frac{\pi \, (BR)^2}{4 \sin \theta} \tag{C.6}$$

for beam-limited conditions including continuous-wave (CW) or long-pulse radar at high grazing angles or

$$A = \frac{(c\tau/2) \, BR}{\cos \theta} \tag{C.7}$$

for limited pulse-width conditions such as short-pulse radar at low grazing angles, as this doctoral dissertation considers, where c ans τ represent the velocity of propagation and the pulse width, respectively [209].

Appendix D

Hilbert Transform

D.1 Mathematical Description

Hilbert transform is particularly useful for signal decomposition based on *phase selectivity* using phase shifts between signals to obtain the desired separation. Just as the *ideal transformer* allows the polarity reversal of 180 degrees, which is the simplest phase shift procedure, the *Hilbert transformer* of a given signal shifts the phase angles of all components by $\pm$ 90 degrees, without affecting the amplitudes of all frequency components in the signal [245].

Therefore, the Hilbert transformation, which is denoted as $\hat{g}(t)$, is a linear operator that convolves the original real-valued signal $g(t)$ with the time function $1/(\pi t)$. The functions $g(t)$ and $\hat{g}(t)$ forms a *Hilbert-transform pair* defined by,

$$\hat{g}(t) = \frac{1}{\pi} \int_{-\infty}^{\infty} \frac{g(\tau)}{t - \tau} \, d\tau; \qquad g(t) = -\frac{1}{\pi} \int_{-\infty}^{\infty} \frac{\hat{g}(\tau)}{t - \tau} \, d\tau \tag{D.1}$$

where $\hat{g}(t)$ denotes the *direct Hilbert transform* and $g(t)$ expression corresponds to the *inverse Hilbert transform* [245]. Since the convolution of two functions in time domain can be transformed into the multiplication of their Fourier transforms in the frequency domain, the Fourier transform of $\hat{g}(t)$, i.e. $\hat{G}(f)$, is given by,

$$\hat{G}(f) = -j\text{sgn}(f)G(f) \tag{D.2}$$

where $G(f)$ is the Fourier transform of the original signal $g(t)$ and the expression $-j\text{sgn}(f)$ corresponds to the Fourier transform of the time function $1/(\pi t)$, being $\text{sgn}(f)$ the *signum function* which can be defined in the frequency domain as,

$$\text{sgn}(f) = \begin{cases} 1, & f > 0 \\ 0, & f = 0 \\ -1, & f < 0 \end{cases} \tag{D.3}$$

Equation D.2 states that for a given $g(t)$ signal, its Hilbert transform $\hat{g}(t)$ can be obtained by passing $g(t)$ through a linear two-port device with frequency response $-j\text{sgn}(f)$ producing a phase shift of -90 degrees for all positive frequency components of $g(t)$ and +90 degrees for all negative frequencies [245]. That is,

$$\arg\left[H(f)\right] = \begin{cases} -90°, & f > 0 \\ 0°, & f = 0 \\ 90°, & f < 0 \end{cases} \tag{D.4}$$

where $\arg\left[H(f)\right]$ is the phase characteristic of the frequency response $H(f)$ from the linear two-port device to obtain the Hilbert transform of a real-valued signal $g(t)$ [245]. For this reason, Hilbert transform is also called a *quadrature filter*.

Unlike Fourier transform, Hilbert transform operates exclusively in the time domain. For a given real-valued signal $g(t)$, some of the basic Hilbert transform properties are listed below [245].

1. A signal $g(t)$ and its Hilbert transform $\hat{g}(t)$ have identical energy because phase shift does not change the magnitude spectrum.

2. If $\hat{g}(t)$ is the Hilbert transform of $g(t)$, then the Hilbert transform of $\hat{g}(t)$ is $-g(t)$.

3. A signal $g(t)$ and its Hilbert transform $\hat{g}(t)$ are orthogonal over the entire time domain. Therefore, $\int_{-\infty}^{\infty} g(t)\hat{g}(t)\, \mathrm{d}t = 0$

D.2   Pre-envelope or Analytical Signal

The *pre-envelope* or *analytical signal* $g_+(t)$ of a given real-valued signal $g(t)$ is the complex-valued function

$$g_+(t) = g(t) + j\hat{g}(t) \tag{D.5}$$

where $g(t)$ is the real part of the pre-envelope $g_+(t)$, and the Hilbert transform of the original signal, $\hat{g}(t)$, is the imaginary part [245]. The pre-envelope definition is particularly useful in band-pass signal representation because the analytic signal is a complex representation made by taking the original signal and then adding in quadrature its Hilbert transform. Fourier transform of the pre-envelope $G_+(f)$ is given by,

$$G_+(f) = G(f) + \mathrm{sgn}(f)G(f) \tag{D.6}$$

from which we can obtain,

$$G_+(f) = \begin{cases} 2G(f), & f > 0 \\ G(0), & f = 0 \\ 0, & f < 0 \end{cases} \tag{D.7}$$

where $G(f)$ is the Fourier transform of the original signal $g(t)$ and $G(0)$ denotes the value of $G(f)$ at frequency $f = 0$. Therefore, the pre-envelope $g_+(t)$ does not have negative frequency components because it is defined for *positive frequencies*. Hence, the complex conjugate of $g_+(t)$ is

the pre-envelope for *positive frequencies* denoted as $g_-(t) = g(t) - j\hat{g}(t)$. In contrast, the spectrum of $g_-(t)$ is non-zero only for *negative frequencies*. Therefore, the pre-envelopes $g_+(t)$ and $g_-(t)$ constitute a pair of complex-valued signals [245].

According to the above analysis, the pre-envelope $g_+(t)$ of a given signal $g(t)$ can be determined by either of the following two methods.

1. We determine the Hilbert transform $\hat{g}(t)$ of the signal $g(t)$. Then, the pre-envelope $g_+(t)$ is computed by using Equation D.5

2. We determine the Fourier transform $G(f)$ and then $G_+(f)$ is obtained by using Equation D.7. Therefore, the pre-envelope $g_+(t)$ is computed by the inverse Fourier transform of $G_+(f)$. That is,

$$g_+(t) = 2 \int_0^\infty G(f) e^{j2\pi ft}\, \mathrm{d}f \tag{D.8}$$

The simplicity of a particular signal $g(t)$ and its Fourier transform $G(f)$ determines which one of these two methods would be better than the other [245].

Bibliography

[1] R. Holman and M. C. Haller, "Remote sensing of the nearshore", *Annual Review of Marine Science*, vol. 5, pp. 95–113, 2013.

[2] W. Navarro, J. C. Velez, A. Orfila, and S. Lonin, "A Shadowing Mitigation Approach for Sea State Parameters Estimation Using X-Band Remotely Sensing Radar Data in Coastal Areas", *IEEE Transactions on Geoscience and Remote Sensing*, vol. 57, no. 9, pp. 6292–6310, 2019, ISSN: 1558-0644. DOI: `10.1109/TGRS.2019.2905104`.

[3] Y. Zhuang, X. Liu, T. Nguyen, Q. He, and S. Hong, "Global remote sensing research trends during 1991–2010: a bibliometric analysis", *Scientometrics*, vol. 96, no. 1, pp. 203–219, 2013, ISSN: 0138-9130. DOI: `10.1007/s11192-012-0918-z`.

[4] J. Yoo and H. Fritz, "Nonlinear Bathymetry Inversion Based on Wave Property Estimation from Nearshore Video Imagery", PhD thesis, Georgia Institute of Technology, 2007, pp. 1–192.

[5] J. Wright, "A new model for sea clutter", *IEEE Trans. Antennas Propagation*, no. 2, pp. 217–223, 1968, ISSN: 0096-1973. DOI: `10.1109/TAP.1968.1139147`.

[6] G. Valenzuela, "Scattering of electromagnetic waves from a tilted slightly rough surface", *Radio Science*, vol. 28, no. 8, pp. 429–431, 1968, ISSN: 00218979. DOI: `10.1063/1.88809`.

[7] R. E. Walker, *Marine Light Field Statistics*. Wiley New York, 1994, ISBN: 9780471310464.

[8] K Reichert, K Hessner, J. Nieto Borge, J Dittmer, *et al.*, "WaMoS II: A radar based wave and current monitoring system", in *The Ninth International Offshore and Polar Engineering Conference*, International Society of Offshore and Polar Engineers, 1999, pp. 1–5.

[9] Josh Friedman, "Development of an X-band Radar Depth Inversion Model at the Sand Motor", Master of Science Thesis, Delft University of Technology, 2014.

[10] J. B. Vides de Andréis, "Diagnóstico de la erosión costera en el caribe colombiano", *INVEMAR, Serie Publicaciones Especiales, Ministerio de Ambiente y Desarrollo Sostenible*, pp. 1–48, 2012.

[11] DIMAR, "Sistema de Medición de Parámetros Oceanográficos y de Meteorología Marina–SMPOMM", 2015. [Online]. Available: `https://www.dimar.mil.co/red-de-medicion-de-parametros-oceanograficos-y-de-meteorologia-marina-redmpomm`.

[12] P. Nielsen, *Coastal bottom boundary layers and sediment transport*. World Scientific Publishing Company, 1992, vol. 4, ISBN: 9813103582.

[13] R. J. Lowe, J. L. Falter, M. D. Bandet, G. Pawlak, M. J. Atkinson, S. G. Monismith, and J. R. Koseff, "Spectral wave dissipation over a barrier reef", *Journal of Geophysical Research: Oceans*, vol. 110, no. C4, 2005.

[14]   O. S. Madsen, "Spectral wave-current bottom boundary layer flows", in *Coastal Engineering 1994*, 1995, pp. 384–398.

[15]   P. P. Mathisen and O. S. Madsen, "Waves and currents over a fixed rippled bed: 3. Bottom and apparent roughness for spectral waves and currents", *Journal of Geophysical Research: Oceans*, vol. 104, no. C8, pp. 18 447–18 461, 1999.

[16]   G. Simarro, D. Calvete, P. Luque, A. Orfila, and F. Ribas, "UBathy: A New Approach for Bathymetric Inversion from Video Imagery", *Remote Sensing*, vol. 11, no. 23, p. 2722, 2019.

[17]   G. Wilson, H. Özkan-Haller, R. Holman, M. Haller, D. Honegger, and C. Chickadel, "Surf zone bathymetry and circulation predictions via data assimilation of remote sensing observations", *Journal of Geophysical Research: Oceans*, vol. 119, no. 3, pp. 1993–2016, 2014.

[18]   J. L. Aarnink, "Bathymetry mapping using drone imagery", Master thesis in Coastal Engineering, Delft University of Technology, 2017, p. 89.

[19]   R. G. Dean and R. A. Dalrymple, *Water Wave Mechanics for Engineers and Scientists - Advanced Series on Ocean Engineering*. World Scientific, 2008, vol. 2, pp. 83–87.

[20]   M. K. Ochi, *Ocean waves: The stochastic approach*, Cambridge University Press, Ed. Cambridge University Press, 2005, vol. 6, ISBN: 978-0-521-01767-1.

[21]   H. F. Stockdon and R. A. Holman, "Estimation of wave phase speed and nearshore bathymetry from video imagery", *Journal of Geophysical Research: Oceans*, vol. 105, no. C9, pp. 22 015–22 033, 2000, ISSN: 01480227. DOI: 10.1029/1999JC000124.

[22]   P. D. Komar, *Beach Processes and Sedimentation*, N. J. Englewood Cliffs, Ed. Prentice-Hall Inc., 1998, p. 429, ISBN: 9780137549382.

[23]   P. Catalán and M. C. Haller, "Nonlinear Phase Speeds and Depth Inversions", in *Coastal Dynamics 2005: State of the Practice*, 2006, pp. 1–14, ISBN: 978-0-7844-0855-1. DOI: 10.1061/40855(214)42.

[24]   T. Holland, "Application of the linear dispersion relation with respect to depth inversion and remotely sensed imagery", *IEEE Transactions on Geoscience and Remote Sensing*, vol. 39, no. 9, pp. 2060–2072, 2001. DOI: 10.1109/36.951097.

[25]   E. B. Thornton and R. T. Guza, "Energy saturation and phase speeds measured on a natural beach", *Journal of Geophysical Research: Oceans*, vol. 87, no. C12, pp. 9499–9508, 1982.

[26]   S. T. Grilli, "Depth inversion in shallow water based on nonlinear properties of shoaling periodic waves", *Coastal Engineering*, vol. 35, no. 3, pp. 185–209, 1998.

[27]   T. Hedges, "An Empirical Modification To Linear Wave Theory", *Proceedings of the Institution of Civil Engineers*, vol. 61, no. 2, pp. 575–579, 1976, ISSN: 1753-7789. DOI: 10.1680/iicep.1976.3408.

[28]   N. Booij, "Gravity waves on water with non-uniform depth and current", Doctoral thesis, Delft University of Technology, 1981.

[29] A. Nortek, "The Comprehensive Manual: AWAC, Aquadopp, Aquadopp Profiler, 2D Horizontal Profiler, Vector and Vectrino", no. September, pp. 1–90, 2005. [Online]. Available: `https://www.nortekgroup.com/assets/documents/ComprehensiveManual_Oct2017_compressed.pdf`.

[30] NORTEK, *Nortek AWAC*. [Online]. Available: `http://www.nortek-as.com/en/products/wave-systems/awac`.

[31] O. Schofield, J. Kohut, U. Kremer, T. Miles, G. Saba, S. Glenn, C. Jones, and D. Webb, "Gliders as maturing technology: Using gliderpalooza as means to develop an integrated glider community", in *OCEANS 2015-MTS/IEEE Washington*, IEEE, 2015, pp. 1–5.

[32] G. Engen and H. Johnsen, "SAR-ocean wave inversion using image cross spectra", *IEEE transactions on geoscience and remote sensing*, vol. 33, no. 4, pp. 1047–1056, 1995.

[33] S. Lehner, J. Schulz-Stellenfleth, B Schattler, H. Breit, and J. Horstmann, "Wind and wave measurements using complex ERS-2 SAR wave mode data", *IEEE Transactions on Geoscience and Remote Sensing*, vol. 38, no. 5, pp. 2246–2257, 2000.

[34] N Ducet, P.-Y. Le Traon, and G. Reverdin, "Global high-resolution mapping of ocean circulation from TOPEX/Poseidon and ERS-1 and-2", *Journal of Geophysical Research: Oceans*, vol. 105, no. C8, pp. 19 477–19 498, 2000.

[35] J. M. Sayol, "A lagrangian multi-approach analysis of the upper ocean mesoscale dynamics", Doctoral thesis, Universitat de les Illes Balears, 2016, p. 173.

[36] J. Bruder, J Carlo, J Gurney, and J Gorman, "IEEE standard for letter designations for radar-frequency bands", *IEEE Aerospace & Electronic Systems Society*, pp. 1–3, 2003.

[37] W. Huang, X. Liu, and E. Gill, "Ocean wind and wave measurements using X-band marine radar: A comprehensive review", *Remote sensing*, vol. 9, no. 12, p. 1261, 2017.

[38] I. R. Young, W Rosenthal, and F Ziemer, "A three-dimensional analysis of marine radar images for the determination of ocean wave directionality and surface currents", *Journal of Geophysical Research: Oceans*, vol. 90, no. C1, pp. 1049–1059, 1985.

[39] J. C. Nieto-Borge, K. Reichert, and J. Dittmer, "Use of nautical radar as a wave monitoring instrument", *Coastal Engineering*, vol. 37, no. 3-4, pp. 331–342, 1999, ISSN: 03783839. DOI: `10.1016/S0378-3839(99)00032-0`.

[40] W. Navarro, J. C. Velez, and A. Orfila, "Estimation of sea state parameters using X-band marine radar technology in coastal areas", in *Sixth International Conference on Remote Sensing and Geoinformation of the Environment (RSCy2018)*, Paphos, Cyprus: Proc. of SPIE Vol. 10773, 2018, pp. 107730X–1–10. DOI: `10.1117/12.2322614`.

[41] I. Arias, J. C. Velez, and M. Calle, "System for Estimation of Significant Height and Direction of Waves by Using Radar Intensities", in *Communications (LATINCOM), 2014 IEEE Latin-America Conference on*, IEEE, 2014, pp. 1–6, ISBN: 9781479971626.

[42] J. C. Nieto-Borge, "Análisis de campos de oleaje mediante radar de navegación en banda X", Doctoral dissertation, Ph. D. thesis, Universidad de Alcalá de Henares, 1997.

[43] P Izquierdo and J. C. Nieto-Borge, "Análisis de oleaje y corrientes superficiales mediante radar de navegación en banda X", *Revista de teledetección: Revista de la Asociación Española de Teledetección*, no. 25, pp. 50–54, 2006.

[44] J. C. Nieto-Borge and C. Guedes Soares, "Analysis of directional wave fields using X-band navigation radar", *Coastal Engineering*, vol. 40, no. 4, pp. 375–391, 2000, ISSN: 03783839. DOI: 10.1016/S0378-3839(00)00019-3.

[45] W. R. Alpers, D. B. Ross, and C. L. Rufenach, "On the detectability of ocean surface waves by real and synthetic aperture radar", *Journal of Geophysical Research: Oceans*, vol. 86, no. C7, pp. 6481–6498, 1981, ISSN: 0148-0227. DOI: 10.1029/JC086iC07p06481.

[46] Keller W.C. and J. Wright, "Microwave scattering and the straining of wind-generated waves", *Radio Science*, vol. 10, no. 2, pp. 139–147, 1975.

[47] Plant W.J., "Bragg scattering of electromagnetic waves from the air/sea interface", *Surface Waves and Fluxes: Current Theory and Remote Sensing*, G. Geernaert and W. Plant, Eds., pp. 41–108, 1990. DOI: https://doi.org/10.1007/978-94-009-0627-3_2.

[48] L. B. Wetzel, "Electromagnetic scattering from the sea at low grazing angles", *Surface Waves and Fluxes*, vol. 2, no. Remote Sensing, pp. 109–171, 1990.

[49] P. H. Y. Lee, J. D. Barter, K. L. Beach, C. L. Hindman, B. M. Lake, H. Rungaldier, J. C. Shelton, A. B. Williams, R. Yee, and H. C. Yuen, "X band microwave backscattering from ocean waves", *Journal of Geophysical Research: Oceans*, vol. 100, no. C2, pp. 2591–2611, 1995, ISSN: 0148-0227. DOI: 10.1029/94JC02741.

[50] K. Hessner, K. Reichert, and B. L. Hutt, "Sea surface elevation maps obtained with a nautical X-Band radar – Examples from WaMoS II stations", *10th International Workshop on Wave Hindcasting and Forecasting and Coastal Hazard Symposium, North Shore, Oahu, Hawaii*, 2007.

[51] A. Serrano, J. Posada, J. C. Velez, and M. Alvarado, "Sensado Remoto De Oleaje Mediante Señales De Radar", *XX Seminario Nacional de Hidráulica e Hidrología*, p. 10, 2013.

[52] B. Lund, C. O. Collins, H. C. Graber, E. Terrill, and T. H. Herbers, "Marine radar ocean wave retrieval's dependency on range and azimuth", *Ocean Dynamics*, vol. 64, no. 7, pp. 999–1018, 2014, ISSN: 16167228. DOI: 10.1007/s10236-014-0725-6.

[53] B. Lund, H. C. Graber, K. Hessner, and N. J. Williams, "On shipboard marine X-band radar near-surface current "Calibration"", *Journal of Atmospheric and Oceanic Technology*, vol. 32, no. 10, pp. 1928–1944, 2015, ISSN: 15200426. DOI: 10.1175/JTECH-D-14-00175.1.

[54] G. Vivone and P. Braca, "Joint probabilistic data association tracker for extended target tracking applied to X-band marine radar data", *IEEE Journal of Oceanic Engineering*, vol. 41, no. 4, pp. 1007–1019, 2016.

[55] X. Zhu, Y. Li, H. Feng, B. Liu, and J. Xu, "Oil spill detection method using X-band marine radar imagery", *Journal of Applied Remote Sensing*, vol. 9, no. 1, p. 095 985, 2015.

[56] C. M. Senet, J. Seemann, and F. Ziemer, "The near-surface current velocity determined from image sequences of the sea surface", *IEEE Transactions on Geoscience and Remote Sensing*, vol. 39, no. 3, pp. 492–505, 2001.

[57] K. Hessner and P. S. Bell, "High resolution current & bathymetry determined by nautical X-band radar in shallow waters", in *Oceans 2009-Europe*, IEEE, 2009, pp. 1–5.

[58] F. Serafino, C. Lugni, and F. Soldovieri, "A novel strategy for the surface current determination from marine X-band radar data", *IEEE Geoscience and Remote Sensing Letters*, vol. 7, no. 2, pp. 231–235, 2009.

[59] W. Huang, R. Carrasco, C. Shen, E. W. Gill, and J. Horstmann, "Surface current measurements using X-band marine radar with vertical polarization", *IEEE Transactions on Geoscience and Remote Sensing*, vol. 54, no. 5, pp. 2988–2997, 2016.

[60] F Raffa, G Ludeno, B Patti, F Soldovieri, S Mazzola, and F Serafino, "X-band wave radar for coastal upwelling detection off the southern coast of Sicily", *Journal of Atmospheric and Oceanic Technology*, vol. 34, no. 1, pp. 21–31, 2017.

[61] Z. Chen, J. Pan, Y. He, and A. T. Devlin, "Estimate of tidal constituents in nearshore waters using X-band marine radar image sequences", *IEEE Transactions on Geoscience and Remote Sensing*, vol. 54, no. 11, pp. 6700–6711, 2016.

[62] P. S. Bell and J. C. Osler, "Mapping bathymetry using X-band marine radar data recorded from a moving vessel", *Ocean dynamics*, vol. 61, no. 12, pp. 2141–2156, 2011.

[63] L.-C. Wu, D.-J. Doong, and J.-H. Wang, "Bathymetry determination from marine radar image sequences using the Hilbert transform", *IEEE Geoscience and Remote Sensing Letters*, vol. 14, no. 5, pp. 644–648, 2017.

[64] M. Punzo, C. Lanciano, D. Tarallo, F. Bianco, G. Cavuoto, R. De Rosa, V. Di Fiore, G. Cianflone, R. Dominici, M. Iavarone, F. Lirer, N. Pelosi, L. Giordano, G. Ludeno, A. Natale, and E. Marsella, "Application of X-Band Wave Radar for Coastal Dynamic Analysis: Case Test of Bagnara Calabra (South Tyrrhenian Sea, Italy)", *Journal of Sensors*, vol. 2016, 2016, ISSN: 16877268. DOI: 10.1155/2016/6236925.

[65] C. E. Greenwood, J. M. A. Murray, A. Vogler, *et al.*, "A method for approximating surface elevation from a shore mounted X-band radar with a low grazing angle", in *The 27th International Ocean and Polar Engineering Conference*, International Society of Offshore and Polar Engineers, 2017.

[66] C. Greenwood, A. Vogler, J. Morrison, and A. Murray, "The approximation of a sea surface using a shore mounted X-band radar with low grazing angle", *Remote Sensing of Environment*, vol. 204, pp. 439–447, 2018.

[67] T. Hilmer and E. Thornhill, "Deterministic wave predictions from the WaMoS II", in *OCEANS 2014-TAIPEI*, IEEE, 2014, pp. 1–8.

[68] T. Hilmer and E. Thornhill, "Observations of predictive skill for real-time deterministic sea waves from the WaMoS II", in *OCEANS 2015-MTS/IEEE Washington*, IEEE, 2015, pp. 1–7.

[69] K. G. Hessner, J. C. Nieto-Borge, and P. S. Bell, "Nautical Radar Measurements in Europe: Applications of WaMos II as a Sensor for Sea State, Current and Bathymetry", in *Remote Sensing of the European Seas*, V. Barale and M. Gade, Eds., Dordrecht: Springer Netherlands, 2008, pp. 435–446, ISBN: 978-1-4020-6772-3. DOI: 10.1007/978-1-4020-6772-3_33.

[70] K. Hessner and J. L. Hanson, "Extraction of coastal wavefield properties from X-band radar", in *2010 IEEE International Geoscience and Remote Sensing Symposium*, IEEE, 2010, pp. 4326–4329.

[71] S. Flampouris, F. Ziemer, and J. Seemann, "Accuracy of bathymetric assessment by locally analyzing radar ocean wave imagery (February 2008)", *IEEE Transactions on Geoscience and Remote Sensing*, vol. 46, no. 10, pp. 2906–2913, 2008, ISSN: 01962892. DOI: `10.1109/TGRS.2008.919687`.

[72] K. Hessner, K. Reichert, J. Dittmer, J. C. N. Borge, and H. Günther, "Evaluation of WaMoS II wave data", in *Ocean Wave Measurement and Analysis (2001)*, 2002, pp. 221–230.

[73] K. Hessner, K. Reichert, J. C. N. Borge, C. L. Stevens, and M. J. Smith, "High-resolution X-Band radar measurements of currents, bathymetry and sea state in highly inhomogeneous coastal areas", *Ocean Dynamics*, vol. 64, no. 7, pp. 989–998, 2014, ISSN: 16167228. DOI: `10.1007/s10236-014-0724-7`.

[74] G Mosterdijk and H Miller, "SeaDarQ validation report", *Dutch Ministry Water Traffic Manage., Rotterdam, The Netherlands, Tech. Rep*, 2008.

[75] R. Gangeskar, "Automatic oil-spill detection by marine X-band radars", *Sea Technology*, 2004.

[76] Oceanwaves Gmbh and Rutter, "Sigma S6 WaMoS ® II", Tech. Rep. 01, 2016, pp. 4–6.

[77] Oceanwaves Gmbh, "Sigma S6 WaMoS ® II High Resolution Current Analysis (HRC) sigma S6 WaMoS ® II High Resolution Current Analysis (HRC)", Tech. Rep. 02, 2016, pp. 5–6.

[78] T. van der Vlugt and R. van der Vlugt, "Comparison of Directional WaveGuide Radar with Directional WaveRider Buoy", *Radac*, pp. 1–6, 2014.

[79] P. Izquierdo, C. Guedes Soares, J. C. Nieto Borge, and G. R. Rodríguez, "A comparison of sea-state parameters from nautical radar images and buoy data", *Ocean Engineering*, vol. 31, no. 17-18, pp. 2209–2225, 2004, ISSN: 00298018. DOI: `10.1016/j.oceaneng.2004.04.004`.

[80] J. C. Nieto-Borge, G. Rodríquez Rodríguez, K. Hessner, and P. I. González, "Inversion of marine radar images for surface wave analysis", *Journal of Atmospheric and Oceanic Technology*, vol. 21, no. 8, pp. 1291–1300, 2004, ISSN: 07390572. DOI: `10.1175/1520-0426(2004)021<1291:IOMRIF>2.0.CO;2`.

[81] L. Cui, Y. He, H. Shen, and H. Lü, "Measurements of ocean wave and current field using dual polarized X-band radar", *Chinese Journal of Oceanology and Limnology*, vol. 28, no. 5, pp. 1021–1028, 2010.

[82] J. C. Nieto-Borge, K. Hessner, P. Jarabo-Amores, and D. D. L. Mata-moya, "Signal-to-noise ratio analysis to estimate ocean wave heights from X-band marine radar image time series", *IET Radar, Sonar & Navigation*, vol. 2, no. 1, pp. 35–41, 2008, ISSN: 1751-8784. DOI: `10.1049/iet-rsn:20070027`.

[83] F Ziemer and H Günther, "A system to monitor ocean wave fields", in *Second International Conference on Air-Sea Interaction and Meteorology and Oceanography of the Coastal Zone*, Lisbon, 1994.

[84]   J. Nieto-Borge and K Hessner, "Estimation of the significant wave height with X-band nautical radars", C, 1999, 11—16.

[85]   P. Izquierdo, J. C. Nieto-Borge, C. Guedes Soares, R. Sanz González, and G. R. Rodríguez, "Comparison of Wave Spectra from Nautical Radar Images and Scalar Buoy Data", *Journal of Waterway, Port, Coastal, and Ocean Engineering*, vol. 131, no. 3, pp. 123–131, 2005, ISSN: 0733-950X. DOI: 10.1061/(ASCE)0733-950X(2005)131:3(123).

[86]   W. Alpers and K. Hasselmann, "Spectral signal to clutter and thermal noise properties of ocean wave imaging synthetic aperture radars", *International Journal of Remote Sensing*, vol. 3, no. 4, pp. 423–446, 1982.

[87]   R. Vicen-Bueno, C. Lido-Muela, and J. Nieto-Borge, "Estimate of significant wave height from non-coherent marine radar images by multilayer perceptrons", *EURASIP Journal on Advances in Signal Processing*, vol. 2012, no. 1, pp. 1–20, 2012, ISSN: 1687-6180. DOI: 10.1186/1687-6180-2012-84.

[88]   K. Ma, X. Wu, X. Yue, L. Wang, and J. Liu, "Array beamforming algorithm for estimating waves and currents from marine X-band radar image sequences", *IEEE Transactions on Geoscience and Remote Sensing*, vol. 55, no. 3, pp. 1262–1272, 2016.

[89]   A.-A. Al-Habashneh, C. Moloney, E. Gill, and W. Huang, "An adaptive method of wave spectrum estimation using X-band nautical radar", *Remote Sensing*, vol. 7, no. 12, pp. 16 537–16 554, 2015.

[90]   J. Qiu, B. Zhang, Z. Chen, and Y. He, "A new modulation transfer function with range and azimuth dependence for ocean wave spectra retrieval from X-band marine radar observations", *IEEE Geoscience and Remote Sensing Letters*, vol. 14, no. 8, pp. 1373–1377, 2017.

[91]   H. Dankert and J. Horstmann, "Ocean surface determination from X-band radar-image sequences", *Journal of Geophysical Research: Oceans*, vol. 109, no. C4, 2004, ISSN: 0148-0227. DOI: 10.1029/2003JC002130.

[92]   L. Cornejo-Bueno, J. Nieto Borge, E. Alexandre, K. Hessner, and S. Salcedo-Sanz, "Accurate estimation of significant wave height with Support Vector Regression algorithms and marine radar images", *Coastal Engineering*, vol. 114, pp. 233–243, 2016, ISSN: 03783839. DOI: 10.1016/j.coastaleng.2016.04.007.

[93]   J. Vogelzang, K. Boogaard, K. Reichert, and K. Hessner, "Wave height measurements with navigation radar", *International Archives of Photogrammetry and Remote Sensing*, vol. 33, no. B7/4; PART 7, pp. 1652–1659, 2000.

[94]   L. Z.-H. Chuang, L.-C. Wu, D.-J. Doong, and C. C. Kao, "Two-dimensional continuous wavelet transform of simulated spatial images of waves on a slowly varying topography", *Ocean Engineering*, vol. 35, no. 10, pp. 1039–1051, 2008.

[95]   L.-C. Wu, L. Z.-H. Chuang, D.-J. Doong, and C. C. Kao, "Ocean remotely sensed image analysis using two-dimensional continuous wavelet transforms", *International journal of remote sensing*, vol. 32, no. 23, pp. 8779–8798, 2011.

[96] J. An, W. Huang, and E. W. Gill, "A self-adaptive wavelet-based algorithm for wave measurement using nautical radar", *IEEE Transactions on Geoscience and Remote Sensing*, vol. 53, no. 1, pp. 567–577, 2014.

[97] G. Ludeno, M. Postacchini, A. Natale, M. Brocchini, C. Lugni, F. Soldovieri, and F. Serafino, "Normalized Scalar Product Approach for Nearshore Bathymetric Estimation from X-Band Radar Images: An Assessment Based on Simulated and Measured Data", *IEEE Journal of Oceanic Engineering*, vol. 43, no. 1, pp. 221–237, 2018, ISSN: 03649059. DOI: 10.1109/JOE.2017.2758118.

[98] F. Serafino, C. Lugni, and F. Soldovieri, "A novel strategy for the surface current determination from marine X-band radar data", *IEEE Geoscience and Remote Sensing Letters*, vol. 7, no. 2, pp. 231–235, 2010.

[99] F. Serafino, C. Lugni, J. C. Nieto Borge, V. Zamparelli, and F. Soldovieri, "Bathymetry Determination via X-Band Radar Data: A New Strategy and Numerical Results", *Sensors*, vol. 10, no. 7, pp. 6522–6534, 2010, ISSN: 1424-8220. DOI: 10.3390/s100706522.

[100] F. S. G. Ludeno, F. Reale, F. Dentale, E. Pugliese Carratelli, A. Natale, "Estimating Nearshore Bathymetry from X-Band Radar Data", in *Coastal Ocean Observing Systems*, Y. Liu, H. Kerkering, and R. Weisberg, Eds., Elsevier Inc., 2015, pp. 265–280.

[101] G. Ludeno, F. Reale, F. Dentale, E. P. Carratelli, A. Natale, F. Soldovieri, and F. Serafino, "An X-band radar system for bathymetry and wave field analysis in a harbour area", *Sensors*, vol. 15, no. 1, pp. 1691–1707, 2015, ISSN: 14248220. DOI: 10.3390/s150101691.

[102] G. Ludeno, C. Brandini, C. Lugni, D. Arturi, A. Natale, F. Soldovieri, B. Gozzini, and F. Serafino, "Remocean system for the detection of the reflected waves from the costa concordia ship wreck", *IEEE Journal of Selected Topics in Applied Earth Observations and Remote Sensing*, vol. 7, no. 7, pp. 3011–3018, 2014, ISSN: 21511535. DOI: 10.1109/JSTARS.2014.2321048.

[103] G. Ludeno, A. Orlandi, C. Lugni, C. Brandini, F. Soldovieri, and F. Serafino, "X-band marine radar system for high-speed navigation purposes: A test case on a cruise ship", *IEEE Geoscience and Remote Sensing Letters*, vol. 11, no. 1, pp. 244–248, 2014, ISSN: 1545598X. DOI: 10.1109/LGRS.2013.2254464.

[104] F. Serafino, C. Lugni, G. Ludeno, D. Arturi, M. Uttieri, B. Buonocore, E. Zambianchi, G. Budillon, and F. Soldovieri, "REMOCEAN: A flexible X-band radar system for sea-state monitoring and surface current estimation", *IEEE Geoscience and Remote Sensing Letters*, vol. 9, no. 5, pp. 822–826, 2012, ISSN: 1545598X. DOI: 10.1109/LGRS.2011.2182031.

[105] G. Ludeno and F. Serafino, "Estimation of the Significant Wave Height from Marine Radar Images without External Reference", *Journal of Marine Science in Engineering*, vol. 7, no. 432, pp. 1–13, 2019. DOI: 10.3390/jmse7120432.

[106] R. Gangeskar, "An algorithm for estimation of wave height from shadowing in X-band radar sea surface images", *IEEE Transactions on Geoscience and Remote Sensing*, vol. 52, no. 6, pp. 3373–3381, 2014, ISSN: 01962892. DOI: 10.1109/TGRS.2013.2272701.

[107] H. Dankert, J. Horstmann, W. Koch, and W. Rosenthal, "Ocean wind fields retrieved from radar-image sequences", *IEEE International Geoscience and Remote Sensing Symposium*, vol. 4, pp. 2150–2152, 2002, ISSN: 0148-0227. DOI: 10.1109/IGARSS.2002.1026475.

[108] H. Dankert and W. Rosenthal, "Retrieval of ocean surface wave fields using marine radar-image sequences", *Geoscience and Remote Sensing Symposium, 2004. IGARSS'04. Proceedings*, vol. 3, pp. 1884–1887, 2004. DOI: 10.1109/IGARSS.2004.1370708.

[109] H. Dankert, J. Horstmann, and W. Rosenthal, "Ocean surface winds retrieved from marine radar-image sequences", *Geoscience and Remote Sensing Symposium, 2004. IGARSS'04. Proceedings. 2004 IEEE International*, vol. 3, pp. 1903–1906, 2004.

[110] W. J. Plant and G. Farquharson, "Wave shadowing and modulation of microwave backscatter from the ocean", *Journal of Geophysical Research: Oceans*, vol. 117, no. 8, pp. 1–14, 2012, ISSN: 21699291. DOI: 10.1029/2012JC007912.

[111] Y. Liu, E. W. Gill, and W. Huang, "Analysis of the effects of rain on surface wind retrieval from X-band marine radar images", in *Oceans - St. John's, 2014*, 2014. DOI: 10.1109/OCEANS.2014.7003161.

[112] J. R. Buckley and J. Aler, "Estimation of ocean wave height from grazing incidence microwave backscatter", in *IGARSS'97. 1997 IEEE International Geoscience and Remote Sensing Symposium Proceedings. Remote Sensing-A Scientific Vision for Sustainable Development*, IEEE, vol. 2, 1997, pp. 1015–1017.

[113] R. Gangeskar, "Wave height derived by texture analysis of X-band radar sea surface images", in *IGARSS 2000. IEEE 2000 International Geoscience and Remote Sensing Symposium. Taking the Pulse of the Planet: The Role of Remote Sensing in Managing the Environment. Proceedings (Cat. No. 00CH37120)*, IEEE, vol. 7, 2000, pp. 2952–2959.

[114] R. Gangeskar, "An adaptive method for estimation of wave height based on statistics of sea surface images", in *IGARSS 2000. IEEE 2000 International Geoscience and Remote Sensing Symposium. Taking the Pulse of the Planet: The Role of Remote Sensing in Managing the Environment. Proceedings (Cat. No. 00CH37120)*, IEEE, vol. 1, 2000, pp. 255–259.

[115] X. Liu, W. Huang, and E. W. Gill, "Comparison of wave height measurement algorithms for ship-borne X-band nautical radar", *Canadian Journal of Remote Sensing*, vol. 42, no. 4, pp. 343–353, 2016.

[116] X. Liu, W. Huang, and E. W. Gill, "Wave height estimation from shipborne X-band nautical radar images", *Journal of Sensors*, vol. 2016, 2016.

[117] S. Salcedo-Sanz, J. C. Nieto Borge, L. Carro-Calvo, L. Cuadra, K. Hessner, and E. Alexandre, "Significant wave height estimation using SVR algorithms and shadowing information from simulated and real measured X-band radar images of the sea surface", *Ocean Engineering*, vol. 101, pp. 244–253, 2015, ISSN: 00298018. DOI: 10.1016/j.oceaneng.2015.04.041.

[118] Z. Chen, Y. He, B. Zhang, Z. Qiu, and B. Yin, "A new algorithm to retrieve wave parameters from marine X-band radar image sequences", *IEEE Transactions on Geoscience and Remote Sensing*, vol. 52, no. 7, pp. 4083–4091, 2013.

[119] T. Yu, W. Xie, and S. Zhang, "Improved algorithm for estimation of significant wave height from X-band radar image sequences", *Journal of Applied Remote Sensing*, vol. 10, no. 4, p. 046 016, 2016.

[120] S. Zhang, Z. Song, and Y. Li, "An advanced inversion algorithm for significant wave height estimation based on random field", *Ocean Engineering*, vol. 127, pp. 298–304, 2016.

[121] X. Liu, W. Huang, and E. W. Gill, "Estimation of significant wave height from X-band marine radar images based on ensemble empirical mode decomposition", *IEEE Geoscience and Remote Sensing Letters*, vol. 14, no. 10, pp. 1740–1744, 2017.

[122] Z. Chen, Y. He, and B. Zhang, "An automatic algorithm to retrieve wave height from X-band marine radar image sequence", *IEEE Transactions on Geoscience and Remote Sensing*, vol. 55, no. 9, pp. 5084–5092, 2017.

[123] P. A. Catálan and M. C. Haller, "Remote sensing of breaking wave phase speeds with application to non-linear depth inversions", *Coastal Engineering*, vol. 55, no. 1, pp. 93–111, 2008, ISSN: 03783839. DOI: `10.1016/j.coastaleng.2007.09.010`.

[124] P. A. Catalán, M. C. Haller, R. A. Holman, and W. J. Plant, "Optical and microwave detection of wave breaking in the surf zone", *IEEE Transactions on Geoscience and Remote Sensing*, vol. 49, no. 6, pp. 1879–1893, 2011, ISSN: 01962892. DOI: `10.1109/TGRS.2010.2095864`.

[125] G. Simarro, K. R. Bryan, R. M. Guedes, A. Sancho, J. Guillen, G. Coco, "On the use of variance images for runup and shoreline detection", *Coastal Engineering*, vol. 99, pp. 136–147, 2015.

[126] A. Arnberger, W. Haider, and C. Brandenburg, "Evaluating visitor-monitoring techniques: A comparison of counting and video observation data", *Environmental Management*, vol. 36, no. 2, pp. 317–327, 2005.

[127] J. Guillén, A. García-Olivares, E. Ojeda, A. Osorio, O. Chic, and R. González, "Long-term quantification of beach users using video monitoring", *Journal of Coastal Research*, pp. 1612–1619, 2008.

[128] R. Almar, G. Coco, K. R. Bryan, D. Huntley, A. Short, and N. Senechal, "Video observations of beach cusp morphodynamics", *Marine geology*, vol. 254, no. 3-4, pp. 216–223, 2008.

[129] A. Alvarez-Ellacuria, A. Orfila, L. Gómez-Pujol, G. Simarro, and N Obregon, "Decoupling spatial and temporal patterns in short-term beach shoreline response to wave climate", *Geomorphology*, vol. 128, no. 3-4, pp. 199–208, 2011.

[130] A. R. de Alegria-Arzaburu and G. Masselink, "Storm response and beach rotation on a gravel beach, Slapton Sands, UK", *Marine Geology*, vol. 278, no. 1-4, pp. 77–99, 2010.

[131] E. Ojeda and J. Guillén, "Shoreline dynamics and beach rotation of artificial embayed beaches", *Marine Geology*, vol. 253, no. 1-2, pp. 51–62, 2008.

[132] A. Sancho-García, J. Guillén, and E. Ojeda, "Storm-induced readjustment of an embayed beach after modification by protection works", *Geo-Marine Letters*, vol. 33, no. 2-3, pp. 159–172, 2013.

[133] W. Van de Lageweg, K. R. Bryan, G. Coco, and B. Ruessink, "Observations of shoreline–sandbar coupling on an embayed beach", *Marine Geology*, vol. 344, pp. 101–114, 2013.

[134] T. Lippmann and H. R.A., "Quantification of sand bar morphology: A video technique based on wave dissipation", *Journal of Geophysical Research*, vol. 94, no. C1, pp. 995–1011, 1989.

[135] R. de Swart, F. Ribas, G. Ruessink, G. Simarro, and J. Guillén, "Characteristics and Dynamics of Crescentic Bar Events in an Open , Tideless Beach", in *Coastal Dynamics 2017*, 2017, pp. 555–566.

[136] F. Ribas, E. Ojeda, T. D. Price, and J. Guillén, "Assessing the suitability of video imaging for studying the dynamics of nearshore sandbars in tideless beaches", *IEEE transactions on geoscience and remote sensing*, vol. 48, no. 6, pp. 2482–2497, 2010.

[137] S. L. Gallop, K. R. Bryan, G. Coco, and S. Stephens, "Storm-driven changes in rip channel patterns on an embayed beach", *Geomorphology*, vol. 127, no. 3-4, pp. 179–188, 2011.

[138] S. Aarninkhof, I. Turner, T. Dronkers, M. Caljouw, and L. Nipius, "A video-based technique for mapping intertidal beach bathymetry", *Coastal Engineering*, vol. 49, no. 4, pp. 275–289, 2003.

[139] B. Morris, G Coco, K. Bryan, and I. Turner, "Video-derived mapping of estuarine evolution", *Journal of Coastal Research*, pp. 410–414, 2007.

[140] R. Holman and J. Stanley, "The history and technical capabilities of Argus", *Coastal Engineering*, vol. 54, no. 6-7, pp. 477–491, 2007.

[141] R. M. C. Guedes, K. R. Bryan, G. Coco, and R. Holman, "The effects of tides on swash statistics on an intermediate beach", *Journal of Geophysical Research: Oceans*, vol. 116, no. C4, 2011.

[142] K. T. Holland, C. L. Vincent, and R. A. Holman, "Statistical characterization of nearshore morphodynamic behavior", in *Coastal Sediments*, ASCE, 1999, pp. 2176–2189.

[143] N. S. Pearre and J. A. Puleo, "Quantifying seasonal shoreline variability at Rehoboth Beach, Delaware, using automated imaging techniques", *Journal of Coastal Research*, pp. 900–914, 2009.

[144] V. Morales Márquez, A. Orfila, G. Simarro, and L. Gómez-Pujol, "Técnicas numéricas y remotas para la gestión de playas: aplicación a un grupo de tormentas", 2019.

[145] M. A. Nieto, B. Garau, S. Balle, G. Simarro, G. A. Zarruk, A. Ortiz, J. Tintoré, A. Álvarez-Ellacuría, L. Gómez-Pujol, and A. Orfila, "An open source, low cost video-based coastal monitoring system", *Earth Surface Processes and Landforms*, vol. 35, no. 14, pp. 1712–1719, 2010.

[146] J. Rutten, S. M. De Jong, and G. Ruessink, "Accuracy of nearshore bathymetry inverted from X-band radar and optical video data", *IEEE Transactions on Geoscience and Remote Sensing*, vol. 55, no. 2, pp. 1106–1116, 2016.

[147] S. G. J. Aarninkhof, "Nearshore bathymetry derived from video imagery", PhD thesis, Delft University of Technology, 2003, p. 191, ISBN: 9040724393.

[148] G. Simarro, F. Ribas, Á. Álvarez, J. Guillén, Ó. Chic, and A. Orfila, "ULISES: An open source code for massive extrinsic calibrations and planview generations in coastal video monitoring systems", *Journal of Coastal Research*, vol. 33, no. 5, pp. 1217–1227, 2017.

[149] A. Alvarez-Ellacuria, A. Orfila, M. Olabarrieta, R. Medina, G. Vizoso, and J. Tintoré, "A Nearshore Wave and Current Operational Forecasting System", *Journal of Coastal Research*, pp. 503–509, 2010, ISSN: 0749-0208. DOI: 10.2112/08-1133.1.

[150] A. F. Osorio, C. A. Ortiz, and J. C. Pérez, "Monitoreo Marino-Costero Y Fluvial Basado En Cámaras De Vídeo: Evolución Del Proyecto Horus", *Cuadernos del Caribe*, vol. 14, no. 1, pp. 36–55, 2010.

[151] A. C. Ocampo, "Estimación del espectro direccional del oleaje mediante procesamiento digital de imágenes", Master thesis, Universidad Nacional, Medellín, Colombia, 2014.

[152] G. C. Guenther, R. W. Thomas, and P. E. LaRocque, "Design considerations for achieving high accuracy with the SHOALS bathymetric lidar system", in *CIS Selected Papers: Laser Remote Sensing of Natural Waters: From Theory to Practice*, International Society for Optics and Photonics, vol. 2964, 1996, pp. 54–71.

[153] F. Levoy, E. J. Anthony, O. Monfort, N. Robin, and P. Bretel, "Formation and migration of transverse bars along a tidal sandy coast deduced from multi-temporal Lidar datasets", *Marine Geology*, vol. 342, pp. 39–52, 2013.

[154] X. Monteys, P. Harris, S. Caloca, and C. Cahalane, "Spatial prediction of coastal bathymetry based on multispectral satellite imagery and multibeam data", *Remote Sensing*, vol. 7, no. 10, pp. 13 782–13 806, 2015.

[155] R. P. Stumpf, K. Holderied, and M. Sinclair, "Determination of water depth with high-resolution satellite imagery over variable bottom types", *Limnology and Oceanography*, vol. 48, pp. 547–556, 2003.

[156] K. Karantzalos, D Argialas, and A Georgopoulos, "Towards automatic detection of coastlines from satellite imagery", in *2002 14th International Conference on Digital Signal Processing Proceedings. DSP 2002 (Cat. No. 02TH8628)*, IEEE, vol. 2, 2002, pp. 897–900.

[157] L. Ruiz, J. Pardo, J Almonacid, and B Rodríguez, "Coastline automated detection and multi-resolution evaluation using satellite images", in *Proceedings of the Coastal Zone*, vol. 7, 2007.

[158] A.-M. Saeed and A.-M. Fatima, "Coastline extraction using satellite imagery and image processing techniques", *International Journal of Current Engineering and Technology*, vol. 6, no. 4, pp. 1245–1251, 2016.

[159] R. Holman, N. Plant, and T. Holland, "cBathy: A robust algorithm for estimating nearshore bathymetry", *Journal of Geophysical Research: Oceans*, vol. 118, no. 5, pp. 2595–2609, 2013.

[160] A. Jessup, C. Zappa, M. Loewen, and V Hesany, "Infrared remote sensing of breaking waves", *Nature*, vol. 385, no. 6611, p. 52, 1997.

[161] G. Marmorino and G. Smith, "Bright and dark ocean whitecaps observed in the infrared", *Geophysical research letters*, vol. 32, no. 11, 2005.

[162] B. G. Ruessink, P. S. Bell, I. M. Van Enckevort, and S. G. Aarninkhof, "Nearshore bar crest location quantified from time-averaged X-band radar images", *Coastal Engineering*, vol. 45, no. 1, pp. 19–32, 2002, ISSN: 03783839. DOI: 10.1016/S0378-3839(01)00042-4.

[163] J. E. McNinch, "Bar and Swash Imaging Radar (BASIR): A Mobile X-band Radar Designed for Mapping Nearshore Sand Bars and Swash-Defined Shorelines Over Large Distances", *Journal of Coastal Research*, vol. 23, no. 1, pp. 59–74, 2007, ISSN: 0749-0208. DOI: 10.2112/05-0452.1.

[164] P. S. Bell, "Shallow water bathymetry derived from an analysis of X-band marine radar images of waves", *Coastal Engineering*, vol. 37, no. 3-4, pp. 513–527, 1999, ISSN: 03783839. DOI: 10.1016/S0378-3839(99)00041-1.

[165] P. S. Bell, "Determination of bathymetry using marine radar images of waves", in *Ocean Wave Measurement and Analysis (2001)*, 2002, pp. 251–257.

[166] D. A. Honegger, M. C. Haller, and R. A. Holman, "High-resolution bathymetry estimates via X-band marine radar: 1. beaches", *Coastal Engineering*, vol. 149, pp. 39–48, 2019.

[167] D. A. Honegger, M. C. Haller, and R. A. Holman, "High-resolution bathymetry estimates via X-band marine radar: 2. Effects of currents at tidal inlets", *Coastal Engineering*, p. 103 626, 2019.

[168] R. Holman, A. Sallenger, T. Lippmann, and J. Haines, "The application of video image processing to the study of nearshore processes", *Oceanography*, vol. 6, no. 3, pp. 78–85, 1993.

[169] E. Bergsma, D. Conley, M. Davidson, and T. O'Hare, "Video-based nearshore bathymetry estimation in macro-tidal environments", *Marine Geology*, vol. 374, pp. 31–41, 2016.

[170] K. L. Brodie, M. L. Palmsten, T. J. Hesser, P. J. Dickhudt, B. Raubenheimer, H. Ladner, and S. Elgar, "Evaluation of video-based linear depth inversion performance and applications using altimeters and hydrographic surveys in a wide range of environmental conditions", *Coastal Engineering*, vol. 136, pp. 147–160, 2018.

[171] I. A. Svendsen, P. Madsen, and J. B. Hansen, "Wave characteristics in the surf zone", in *Coastal Engineering 1978*, 1978, pp. 520–539.

[172] P Bonneton, "Wave celerity in the inner surf zone", in *Coastal Engineering 2004: (In 4 Volumes)*, World Scientific, 2005, pp. 392–401.

[173] J. T. Kirby and R. A. Dalrymple, "An approximate model for nonlinear dispersion in monochromatic wave propagation models", *Coastal Engineering*, vol. 9, no. 6, pp. 545–561, 1986.

[174] S. Flampouris, J. Seemann, C. Senet, and F. Ziemer, "The influence of the inverted sea wave theories on the derivation of coastal bathymetry", *IEEE Geoscience and Remote Sensing Letters*, vol. 8, no. 3, pp. 436–440, 2010.

[175] C. M. Senet, J. Seemann, S. Flampouris, and F. Ziemer, "Determination of bathymetric and current maps by the method DiSC based on the analysis of nautical X-band radar image sequences of the sea surface (November 2007)", *IEEE Transactions on Geoscience and Remote Sensing*, vol. 46, no. 8, pp. 2267–2279, 2008.

[176] P. Bell, "Mapping shallow water coastal areas using a standard marine X-Band radar", Proceedings of Hydro8 Conference, International Federation of Hydrographic Societies, 2008.

[177] P. S. Bell, J. J. R. Williams, S Clark, B. D. Morris, and A Vila-Concejo, "Nested Radar Systems for Remote Coastal Observations", *J. Coastal Research: ICS 2004 Proceedings*, vol. Special Is, no. 39, pp. 483–487, 2004, ISSN: 0749-0208.

[178] D. B. Trizna, "Errors in bathymetric retrievals using linear dispersion in 3-d fft analysis of marine radar ocean wave imagery", *IEEE Transactions on Geoscience and Remote Sensing*, vol. 39, no. 11, pp. 2465–2469, 2001.

[179] R. Abileah and D. B. Trizna, "Shallow water bathymetry with an incoherent x-band radar using small (smaller) space-time image cubes", in *2010 IEEE International Geoscience and Remote Sensing Symposium*, IEEE, 2010, pp. 4330–4333.

[180] P. S. Bell, C. O. Bird, and A. J. Plater, "A temporal waterline approach to mapping intertidal areas using X-band marine radar", *Coastal Engineering*, vol. 107, pp. 84–101, 2016, ISSN: 03783839. DOI: 10.1016/j.coastaleng.2015.09.009.

[181] C. O. Bird, P. S. Bell, and A. J. Plater, "Application of marine radar to monitoring seasonal and event-based changes in intertidal morphology", *Geomorphology*, vol. 285, pp. 1–15, 2017.

[182] P. S. Bell, J. Lawrence, and J. V. Norris, "Determining currents from marine radar data in an extreme current environment at a tidal energy test site", *International Geoscience and Remote Sensing Symposium (IGARSS)*, pp. 7647–7650, 2012, ISSN: 2153-6996. DOI: 10.1109/IGARSS.2012.6351856.

[183] J. Mcninch and K. Brodie, "Shallow-water bathymetry measurements during storm events using Bar And Swash Imaging Radar (BASIR), a mobile X-band radar", pp. 1–4, 2007.

[184] E. H. Boak and I. L. Turner, "Shoreline definition and detection: a review", *Journal of coastal research*, pp. 688–703, 2005.

[185] A. Kroon, S. Davidson, M.A. Aarninkhof, R Archetti, C. Armaroli, M Gonzalez, S. Medri, A. Osorio, T. Aagaard, R. Holman, and Spanhoff, "Application of remote sensing video systems to coastline management problems", *Coastal Engineering*, vol. 54, pp. 493–505, 2007.

[186] M. Davidson, M. Van Koningsveld, A. De Kruif, J. Rawson, R. Holman, A. Lamberti, R. Medina, A. Kroon, and S. Aarninkhof, "The CoastView project: Developing videoderived Coastal State Indicators in support of coastal zone management", *Coastal Engineering*, vol. 54, pp. 463–475, 2007.

[187] A. Luijendijk, G. Hagenaars, R. Ranasinghe, F. Baart, G. Donchyts, and S. Aarninkhof, "The state of the world's beaches", *Scientific reports*, vol. 8, no. 1, p. 6641, 2018.

[188] J. Williams, L. Esteves, J Atkinson, *et al.*, "X-band radar system to support coastal management decisions", *Australasian Coasts & Ports 2017: Working with Nature*, p. 1179, 2017.

[189] M. C. Haller and D. R. Lyzenga, "Comparison of Radar and Video Observations of Shallow Water Breaking Waves", *IEEE Transactions on Geoscience and Remote Sensing*, vol. 41, no. 4, pp. 832–844, 2003.

[190]   P. Catalán, M. Haller, R. Holman, and W. Plant, "Surf Zone Wave Breaking Identification Using Marine Radar", in *Coastal Engineering 2008: (In 5 Volumes)*, World Scientific, 2009, pp. 60–72.

[191]   D. Perkovic, T. C. Lippmann, and S. J. Frasier, "Longshore surface currents measured by doppler radar and video PIV techniques", *IEEE Transactions on Geoscience and Remote Sensing*, vol. 47, no. 8, pp. 2787–2800, 2009, ISSN: 01962892. DOI: 10.1109/TGRS.2009.2016556.

[192]   A. Benetazzo, F. Serafino, F. Bergamasco, G. Ludeno, F. Ardhuin, P. Sutherland, M. Sclavo, and F. Barbariol, "Stereo imaging and X-band radar wave data fusion: An assessment", *Ocean Engineering*, vol. 152, pp. 346–352, 2018, ISSN: 00298018. DOI: 10.1016/j.oceaneng.2018.01.077.

[193]   A. van Dongeren, N. Plant, A. Cohen, D. Roelvink, M. C. Haller, and P. Catalán, "Beach Wizard: Nearshore bathymetry estimation through assimilation of model computations and remote observations", *Coastal Engineering*, vol. 55, no. 12, pp. 1016–1027, 2008, ISSN: 03783839. DOI: 10.1016/j.coastaleng.2008.04.011.

[194]   A. Ramirez M, *Colombian Beaches: Hazards and risk assessment*, 2006.

[195]   CIOH Operational Oceanography, *Marine Observations*, 2017. [Online]. Available: https://www.cioh.org.co/meteorologia/ObMaritimas.php?obm=bar (visited on 10/16/2017).

[196]   W. Guzmán and B. O. G. Posada, *Programa Nacional de Investigación para la Prevención, Mitigación y Control de la Erosión Costera en Colombia PNIEC: Plan de acción 2009-2019*, Bogotá D.C., 2009.

[197]   E. Infantes, A. Orfila, G. Simarro, J. Terrados, M. Luhar, and H. Nepf, "Effect of a seagrass (Posidonia oceanica) meadow on wave propagation", *Marine Ecology Progress Series*, vol. 456, pp. 63–72, 2012.

[198]   J. Tintoré, R. Medina, L. Gómez-Pujol, A. Orfila, and G. Vizoso, "Integrated and interdisciplinary scientific approach to coastal management", *Ocean & Coastal Management*, vol. 52, no. 10, pp. 493–505, 2009.

[199]   J. Geister and J. Díaz, "Reef environments and geology of an Oceanic Archipelago: San Andrés, Old Providence and Santa Catalina (Caribbean Sea, Colombia) with Field Guide", *Boletín geológico*, 2007.

[200]   J. Vega-Sequeda, C. M. Díaz-Sánchez, K. Gómez-Campo, T. López-Londoño, M. Díaz-Ruiz, and D. I. Gómez-López, "Marine biodiversity in remote areas in the Colombian Caribbean: New shoal, Alice shoal and Serranilla bank", *Boletín de Investigaciones Marinas y Costeras - INVEMAR*, vol. 44, pp. 199 –224, Jun. 2015, ISSN: 0122-9761.

[201]   FURUNO Electric Co. Ltd., *Operator's Manual, FURUNO Marine Radar Model FR-8062, FR-8122, FR-8252*, 2006.

[202]   N. Booij, R. C. Ris, and L. H. Holthuijsen, "A third-generation wave model for coastal regions: 1. Model description and validation", *Journal of geophysical research: Oceans*, vol. 104, no. C4, pp. 7649–7666, 1999.

[203]   S. Kobayashi, Y. Ota, Y. Harada, A. Ebita, M. Moriya, H. Onoda, K. Onogi, H. Kamahori, C. Kobayashi, H. Endo, *et al.*, "The JRA-55 reanalysis: General specifications and basic characteristics", *Journal of the Meteorological Society of Japan. Ser. II*, vol. 93, no. 1, pp. 5–48, 2015.

[204]   G. Komen, K Hasselmann, and K. Hasselmann, "On the existence of a fully developed wind-sea spectrum", *Journal of physical oceanography*, vol. 14, no. 8, pp. 1271–1285, 1984.

[205]   A. F. Orejarena-Rondón, J. M. Sayol, M. Marcos, L. Otero, J. C. Restrepo, I. Hernández-Carrasco, and A. Orfila, "Coastal impacts driven by sea-level rise in cartagena de indias", *Frontiers in Marine Science*, vol. 6, p. 614, 2019.

[206]   M. I. Skolnik, *Introduction to Radar Systems*, 3rd ed. McGraw-Hill, 2001, ISBN: 0070579091.

[207]   A. P. Wijaya and E van Groesen, "Determination of the significant wave height from shadowing in synthetic radar images", *Ocean Engineering*, vol. 114, pp. 204–215, 2015, ISSN: 00298018. DOI: `10.1016/j.oceaneng.2016.01.011`.

[208]   Y. Wei, Z. Lu, G. Pian, and H. Liu, "Wave height estimation from shadowing based on the acquired X-band marine radar images in coastal area", *Remote Sensing*, vol. 9, no. 8, pp. 1–20, 2017, ISSN: 20724292. DOI: `10.3390/rs9080859`.

[209]   M. I. Skolnik, *Radar Handbook*, M. I. Skolnik, Ed., 1. McGraw-Hill, 1990, vol. 7, ISBN: 9780071485470. DOI: `10.1007/s10194-006-0268-4`.

[210]   D. C. Montgomery, *Design and analysis of experiments*, Second Edi. Limusa Wiley, 2017, p. 686, ISBN: 968-18-6156-6.

[211]   R. Torres and S. Lonin, "Asimilación de datos satelitales en un modelo operacional de oleaje en el Caribe", *Boletín Científico CIOH*, no. 27, pp. 66–81, 2009.

[212]   I. A. Hernández, "Extracción de Parámetros Característicos del Estado del Mar a partir de Intensidades de Radares Fijos Ubicados en Plataformas Costeras", Master Thesis, Universidad del Norte, 2014, p. 82.

[213]   K. Hasselmann, T. P. Barnett, E. Bouws, H. Carlson, D. E. Cartwright, K. Enke, J. A. Ewing, H. Gienapp, D. E. Hasselmann, P. Kruseman, A. Meerburg, P Muller, D. J. Olbers, K. Richter, W. Sell, and H. Walden, "Measurements of Wind-Wave Growth and Swell Decay during the Joint North Sea Wave Project (JONSWAP)", *Ergnzungsheft zur Deutschen Hydrographischen Zeitschrift Reihe*, vol. A(8), no. 12, p.95, 1973.

[214]   R. Torres and S. Lonin, "Study of the wave spectra in the Caribbean observed with buoys and its representation on the JONSWAP spectra", *Boletín Científico CIOH*, no. 25, pp. 8–18, 2007.

[215]   Z.-C. Huang, L. Lenain, W. K. Melville, J. H. Middleton, B. Reineman, N. Statom, and R. M. McCabe, "Dissipation of wave energy and turbulence in a shallow coral reef lagoon", *Journal of Geophysical Research: Oceans*, vol. 117, no. C3, 2012.

[216]   S. G. Monismith, J. S. Rogers, D. Koweek, and R. B. Dunbar, "Frictional wave dissipation on a remarkably rough reef", *Geophysical Research Letters*, vol. 42, no. 10, pp. 4063–4071, 2015.

[217] R. J. Lowe, U. Shavit, J. L. Falter, J. R. Koseff, and S. G. Monismith, "Modeling flow in coral communities with and without waves: A synthesis of porous media and canopy flow approaches", *Limnology and Oceanography*, vol. 53, no. 6, pp. 2668–2680, 2008.

[218] R. J. Lowe, J. R. Koseff, and S. G. Monismith, "Oscillatory flow through submerged canopies: 1. Velocity structure", *Journal of Geophysical Research: Oceans*, vol. 110, no. C10, 2005.

[219] R. J. Lowe, J. L. Falter, S. G. Monismith, and M. J. Atkinson, "A numerical study of circulation in a coastal reef-lagoon system", *Journal of Geophysical Research: Oceans*, vol. 114, no. C6, 2009.

[220] R. J. Lowe, J. L. Falter, S. G. Monismith, and M. J. Atkinson, "Wave-driven circulation of a coastal reef–lagoon system", *Journal of Physical Oceanography*, vol. 39, no. 4, pp. 873–893, 2009.

[221] S. Massel and M. Gourlay, "On the modelling of wave breaking and set-up on coral reefs", *Coastal engineering*, vol. 39, no. 1, pp. 1–27, 2000.

[222] D. Harris, A. Rovere, V. Parravicini, and E. Casella, "The role of coral reef rugosity in dissipating wave energy and coastal protection", in *Geophysical Research Conference Abstracts*, EGU General Assembly, vol. 18, 2016.

[223] D. L. Harris, A. Rovere, E. Casella, H. Power, R. Canavesio, A. Collin, A. Pomeroy, J. M. Webster, and V. Parravicini, "Coral reef structural complexity provides important coastal protection from waves under rising sea levels", *Science advances*, vol. 4, no. 2, eaao4350, 2018.

[224] J. D. Hedley, C. M. Roelfsema, I. Chollett, A. R. Harborne, S. F. Heron, S. Weeks, W. J. Skirving, A. E. Strong, C. M. Eakin, T. R. Christensen, *et al.*, "Remote Sensing of Coral Reefs for Monitoring and Management: A Review", *Remote Sensing*, vol. 8, no. 2, p. 118, 2016.

[225] G. Hodgson, "Reef Check: The first step in community-based management", *Bulletin of Marine Science*, vol. 69, no. 2, pp. 861–868, 2001.

[226] P. L. Colin, *Marine Environments of Palau*. Coral Reef Research Foundation, 2009, pp. 1–27, ISBN: 978-0-615-27484-3.

[227] S Bainbridge, C Steinberg, and M Furnas, "GBROOS— An Ocean Observing System for the Great Barrier Reef", in *Proceedings of the 11th International Coral reef Symposium*, Ft. Lauderdale, Florida, 2010, pp. 529–533.

[228] F. d. M. Rudorff and D. F. M. Gherardi, "Coral reef detection using SAR/RADARSAT-1 images at Costa dos Corais, PE/AL, Brazil", *Brazilian journal of oceanography*, vol. 56, no. 2, pp. 85–96, 2008.

[229] E Yuvaraj, S. D. Kumar, and K Dharanirajan, "An approach for extracting coral reef environs by interpreting multi-dimensional sar and multispectral data", *Journal of the Indian Society of Remote Sensing*, vol. 43, no. 3, pp. 617–624, 2015.

[230] M. Heron, B Willis, A Prytz, P Cetina-Heredia, Y Mao, O Hoegh-Guldberg, W. Skirving, S. Heron, C. Eakin, and C. Steinberg, "HF ocean surface radar monitoring for coral bleaching in the Great Barrier Reef", in *OCEANS 2006*, IEEE, 2006, pp. 1–5.

[231] M. Heron, A. Mantovanelli, D. D. Massa, and S. Heron, "Coastal ocean radars applied to coral reef science and management", in *Proceedings of the 12th International Coral Reef Symposium*, Remote sensing of reef environments, Cairns, Australia, 2012, pp. 1–5.

[232] D. D. DiMassa, M. L. Heron, A. Mantovanelli, S. F. Heron, and C. Steinberg, "Can vertical mixing from turbulent kinetic energy mitigate coral bleaching? An application of high frequency ocean radar", in *OCEANS'10 IEEE SYDNEY*, IEEE, 2010, pp. 1–5.

[233] S. R. Phinn, "Radar Applications", in *Coral Reef Remote Sensing: A Guide for Mapping, Monitoring and Management*, Springer Netherlands, 2013, ch. 13, pp. 248–262. DOI: 10. 1007/978-90-481-9292-2.

[234] J. Garzón-Ferreira and J. M. Díaz, "The Caribbean coral reefs of Colombia", in *Latin American coral reefs*, Elsevier, 2003, pp. 275–301.

[235] R. J. Lowe, J. L. Falter, J. R. Koseff, S. G. Monismith, and M. J. Atkinson, "Spectral wave flow attenuation within submerged canopies: Implications for wave energy dissipation", *Journal of Geophysical Research: Oceans*, vol. 112, no. C5, 2007.

[236] R. A. Dalrymple, J. T. Kirby, and P. A. Hwang, "Wave diffraction due to areas of energy dissipation", *Journal of Waterway, Port, Coastal, and Ocean Engineering*, vol. 110, no. 1, pp. 67–79, 1984.

[237] M. Luhar, E. Infantes, A. Orfila, J. Terrados, and H. M. Nepf, "Field observations of wave-induced streaming through a submerged seagrass (Posidonia oceanica) meadow", *Journal of Geophysical Research: Oceans*, vol. 118, no. 4, pp. 1955–1968, 2013.

[238] M. P. Lesser, V. M. Weis, M. R. Patterson, and P. L. Jokiel, "Effects of morphology and water motion on carbon delivery and productivity in the reef coral, Pocillopora damicornis (Linnaeus): diffusion barriers, inorganic carbon limitation, and biochemical plasticity", *Journal of Experimental Marine Biology and Ecology*, vol. 178, no. 2, pp. 153–179, 1994.

[239] M. A. Reidenbach, J. R. Koseff, S. G. Monismith, J. V. Steinbuckc, and A. Genin, "The effects of waves and morphology on mass transfer within branched reef corals", *Limnology and Oceanography*, vol. 51, no. 2, pp. 1134–1141, 2006.

[240] P. A. Marshall, "Skeletal damage in reef corals: relating resistance to colony morphology", *Marine Ecology Progress Series*, vol. 200, pp. 177–189, 2000.

[241] K. O. Karantzalos, D. Argialas, and A. Georgopoulos, "Towards automatic detection of coastlines from satelite imagery", in *International Conference on Digital Signal Processing, DSP*, vol. 2, 2002, pp. 897–900, ISBN: 0780375033. DOI: 10.1109/ICDSP.2002.1028235.

[242] P. Maragos, "Morphological filtering for image enhancement and feature detection", *The Image and Video Processing Handbook*, pp. 135–156, 2005.

[243] C. Pascual, F. Incera, R. Solana, S. Landeira, P. Braña, A. Sampedro, M. García, C. Lasa, A. Hermosa, B. Reguero, *et al.*, "Evaluación del potencial de la energía de las olas", *Estudio Técnico PER*, 2011.

[244] D. A. Thompson, H. Karunarathna, and D. E. Reeve, "Computational investigation of the effects of bi-modal seas on wave overtopping", *Coastal Dynamics*, 2017.

[245] S. Haykin, *Communication systems*. John Wiley & Sons, 2008, ISBN: 9789681863074.